PARAMETRIC STUDY OF LIQUID FUEL JET IN CROSSFLOW AT CONDITIONS TYPICAL OF AEROSPACE APPLICATIONS

A Thesis
Presented to
The Academic Faculty

by

Jonathan R. Reichel

In Partial Fulfillment
of the Requirements for the Degree
Masters in the
School of Aerospace Engineering

Georgia Institute of Technology
May 2008

PARAMETRIC STUDY OF LIQUID FUEL JET IN CROSSFLOW AT CONDITIONS TYPICAL OF AEROSPACE APPLICATION

Approved by:

Dr. Ben T. Zinn, Advisor
School of Aerospace Engineering
Georgia Institute of Technology

Dr. Jerry Seitzman
School of Aerospace Engineering
Georgia Institute of Technology

Dr. Eugene Lubarsky
School of Aerospace Engineering
Georgia Institute of Technology

DEDICATION

I would like to dedicate this to Laura. It's not easy being a grad student's wife. You are amazing. ~ With All My Love, J.R.

ACKNOWLEDGEMENTS

I would like to thank Dr. Zinn and Dr. Lubarsky for their guidance in the Combustion Lab. I also wish to thank Yogish Gopala for his efforts throughout experimentation and data processing, his help has been invaluable. Finally, thank you to the entire Ben T. Zinn Combustion Laboratory staff and to the sponsors of this research for their generous support.

TABLE OF CONTENTS

Page

ACKNOWLEDGEMENTS iv

LIST OF TABLES vii

LIST OF FIGURES viii

NOMENCLATURE xii

SUMMARY xiii

CHAPTER

1 Introduction 1

Literature Review 1

Current Study 3

Experimental Setup 4

Incoming Air Flow Characterization 15

2 Spray Characterization 26

Operating Conditions 26

Characterization Results 27

3 Weber Number Dependence 34

Operating Conditions 34

Weber Number Effects Results 34

4 Injector Design Dependence 42

Operating Conditions 42

Injector Design Effects Results 43

5 Concluding Remarks 53

Spray Characterization 53

Weber Number Dependence 55

Injector Design Dependence 56

APPENDIX A: Spray Characterization Figures 58

REFERENCES 88

VITA 90

LIST OF TABLES

Page

Table 1.1: Operating Conditions for Characterization of Incoming Air Flow Core 16

Table 1.2: Operating Conditions for Boundary Layer Investigation 16

Table 2.1: Operating Conditions for Study of Characteristics of Spray 26

Table 3.1: Air and Fuel Characteristics for Different Weber Numbers 34

Table 4.1: Experimental Conditions for Imaging and Spray Characterization of Different Injectors 42

LIST OF FIGURES

Page

Figure 1.1: Schematic of Test Facility 4

Figure 1.2: (a) Three-window test section 5

(b) View of test section submerged in pressure chamber 5

Figure 1.3: Instrumentation of Facility 8

Figure 1.4: Schematic of Fuel Supply 9

Figure 1.5: Coordinate System 10

Figure 1.6: (a) Schematic of Micro-LDV setup 12

(b) Lens used for Micro-LDV 12

Figure 1.7: Schematic of Spray Imaging Apparatus 13

Figure 1.8: Raw image and Flattened image for noise reduction 14

Figure 1.9: (a) Axial Velocity profiles along the wall normal direction at M=0.2 17

(b) RMS Velocity profiles along the wall normal direction at M=0.2 17

(c) Axial Velocity Profiles in the y direction at M=0.2 18

(d) RMS Velocity profiles in the y direction at M=0.2 18

Figure 1.10: (a) Axial Velocity profiles along the wall normal direction at M=0.35 20

(b) RMS Velocity profiles along the wall normal direction at M=0.35 20

Figure 1.11: (a) Comparison of Axial Velocity profiles at locations 5mm and 2mm upstream of the orifice, M=0.2 21

(b) Comparison of RMS Velocity profiles at locations 5mm and 2mm upstream of the orifice, M=0.2 21

Figure 1.12: (a) Comparison of Axial Velocity profiles at locations 5mm and 2mm upstream of the orifice, M=0.35 22

(b) Comparison of Axial Velocity profiles at locations 5mm and 2mm upstream of the orifice, M=0.35 22

Figure 1.13: Avg. Velocity profiles near orifice plate (effect of spray) 24

Figure 1.14: RMS Velocity Plots near orifice plate (effect of spray) 25

Figure 3.1: (a) AMD for different Weber numbers 35

(b) SMD for different Weber numbers 35

Figure 3.2: Diameter Histograms at various values of We number at 16mm from injection wall 36

Figure 3.3: Z velocity components and ratios at different Weber numbers 38

Figure 3.4: X velocity components at different Weber numbers 40

Figure 3.5: X RMS velocities at different Weber numbers 41

Figure 4.1: Injector profiles 43

Figure 4.2: Injector evaluations at We=0 44

Figure 4.3: Instantaneous micro images of jet at We=0 45

Figure 4.4: Volume Flux Comparison between injectors #1 and #2 46

Figure 4.5: D_{10} Comparison b/w injectors #1 and #2 47

Figure 4.6: D_{32} Comparison b/w injectors #1 and #2 48

Figure 4.7: Mean Z-velocity Comparison b/w injectors #1 and #2 49

Figure 4.8: RMS Z-velocity Comparison b/w injectors #1 and #2 50

Figure 4.9: Mean X-velocity Comparison b/w injectors #1 and #2 51

Figure 4.10: RMS X-velocity Comparison b/w injectors #1 and #2 52

Figure A.1: Mean Diameters in the plane of Z=30mm at M=0.2 58

Figure A.2: Arithmetic Mean Diameter at M=0.2 for different Z locations 59

Figure A.3: Arithmetic Mean Diameter, view along x-axis at M=0.2 for different Z locations 60

Figure A.4: Sauter Mean Diameter at M=0.2 for different Z locations 61

Figure A.5: Arithmetic Mean Diameter at M=0.35 for different Z locations 62

Figure A.6: Arithmetic Mean Diameter, view along x-axis at M=0.35 for different Z locations 63

Figure A.7: Sauter Mean Diameter at M=0.35 for different Z locations 64

Figure A.8: Z Velocities in the plane of Z=30mm at M=0.2 65

Figure A.9: Z Velocity at M=0.2 for different Z locations 66

Figure A.10: Z Velocity, view along y-axis at M=0.2 for different Z locations 67

Figure A.11: Z RMS Velocity at M=0.2 for different Z locations 68

Figure A.12: Z Velocity at M=0.35 for different Z locations 69

Figure A.13: Z Velocity, view along y-axis at M=0.35 for different Z locations 70

Figure A.14: Z RMS Velocity at M=0.35 for different Z locations 71

Figure A.15: X Velocities in the plane of Z=30mm at M=0.2 72

Figure A.16: X velocity at M=0.2 for different Z locations 73

Figure A.17: X velocity, view along x-axis at M=0.2 for different Z locations 74

Figure A.18: RMS Velocity at M=0.2 for different Z locations 75

Figure A.19: X velocity at M=0.35 for different Z locations 76

Figure A.20: X velocity, view along x-axis at M=0.35 for different Z locations 77

Figure A.21: X RMS Velocity at M=0.35 for different Z locations 78

Figure A.22: Y velocities in the plane of Z=30mm at M=0.2 79

Figure A.23: Y Velocity at M=0.2 for different Z locations 80

Figure A.24: Y Velocity, view along y-axis at M=0.2 for different Z locations 81

Figure A.25: Y RMS Velocity at M=0.2 for different Z locations 82

Figure A.26: Y RMS Velocity, view along y-axis at M=0.2 for different Z locations 83

Figure A.27: Y Velocity at M=0.35 for different Z locations 84

Figure A.28: Y Velocity, view along y-axis at M=0.35 for different Z locations 85

Figure A.29: Y RMS Velocity at M=0.35 for different Z locations 86

Figure A.30: Y RMS Velocity, view along y-axis at M=0.35 for different Z locations 87

NOMENCALTURE

D	=	droplet diameter
D_{10}, AMD	=	arithmetic mean diameter, $\sum D_i n_i / \sum n_i$
D_{32}, SMD	=	Sauter mean diameter, $\sum D_i^3 n_i / \sum D_i^2 n_i$
T_f	=	Fuel temperature at injection (K)
σ	=	surface tension
λ	=	laser wavelength
q	=	liquid to air momentum-flux ratio, $\rho_l U_l^2 / \rho_a U_a^2$
Re	=	Reynolds number, $LU\rho/\mu$
ρ	=	density
P	=	pressure
U	=	speed
We	=	aerodynamic Weber number, $\rho_a U_a^2 D / \sigma$
d	=	Diameter of the orifice, =457 microns (0.018 inches)
Injector #1	=	L/D~10, sharp-edged, D=457μm
Injector #2	=	L/D~1, smooth countersink design, D=457μm
$\dot{m}_f$	=	Fuel mass flow rate (g/s)
V_{air}	=	Velocity of incoming air flow (m/s)
M	=	Mach number, U_a/a
V_f	=	Velocity of injected fuel (m/s)

SUMMARY

This report describes a parametric study of the spray created by Jet-A fuel injection into a crossflow (M=0.2 and M=0.35) of preheated (T=555K) air. Test section configuration and operating conditions correspond to modern jet engine operating conditions. The focus of this research is threefold: characterize the spray created by a liquid fuel jet in a crossflow at conditions typical of aerospace applications, analyze the influence of Weber number upon spray characteristics, and evaluate the influence of injector design upon spray characteristics.

For the study of spray characteristics, fuel was injected from a plate containing a single sharp edged orifice, 430 microns in diameter with an L/D ratio of 10 and a fuel coefficient (μ_f) of 0.73. Pressure in the test section was 4 atm and fuel to air momentum ratio was 40. Laser Doppler Velocimetry (LDV) and micro-LDV techniques were used for the characterization of the incoming air flow in the core and in the boundary layer respectively. A Phase Doppler Particle Analyzer (PDPA) was used for the measurement of diameter and velocity of the droplets.

Droplet arithmetic mean and Sauter mean diameters along with spray velocities and their Root-Mean-Squared (RMS) values were measured. It was seen that the primary mechanism of spray formation was shear breakup at which small droplets (12-20 micron in diameter) were formed immediately after small eddies stripped off from the boundary layer of the fuel jet. A region consisting of a limited number of much larger droplets (~100 microns) was found to exist in the spray at the cross-flow condition of M=0.35. Smaller droplets were observed close to the plate and larger ones on the periphery of the spray. Smaller droplets were formed at higher Mach

number. Velocities of droplets in fully developed spray were found to be 20-40% lower (on the peripheries and in the core of the spray respectively) then the velocity of the incoming air flow.

RMS velocities were found to be greatest at the core of the spray. The RMS velocity in the direction of the airflow was found to be distributed in the shape of a "hat structure" which consists of two maximum values of RMS at ±2mm from the spray centerline. This structure was most likely formed by a vortex flow that surrounds the core of the spray.

After a characterization of the spray at the above conditions, the Weber number (We) of the spray in crossflow was varied between 33 and 2020 and the effect of We on spray properties was investigated. It was seen that shear breakup mechanism dominates at We greater than about 100. Droplets' diameters were found to be in the range of 15-30 microns for higher values of We, while larger droplets (100-200 microns) were observed at Weber number of 33. Larger droplets were observed at the periphery of the spray.

Finally, the spray created by Jet A fuel injection from the plate containing sharp edged orifice (L/D~10) was compared to that created by a smooth countersunk injector with a L/D ratio of approximately unity under the same flow conditions. For this test, pressure was raised to 5 atm. The Weber number (We) of the spray and momentum-flux ratio (q) of the spray were also investigated with measurements taken at We=500, 1000, and 1500 and q=10, 20, and 40.

The smooth countersink design in the second injector is meant to decrease, if not eliminate all together, the turbulence within the fuel injection column. The two component Phase Doppler Particle Analyzer was used for measuring the characteristics of the spray along its centerline. Macro images of the spray were also taken for spray trajectory (outer-edge) measurements.

It was found that the spray produced by the smooth countersunk injector penetrates further into the test section away from the injector orifice by approximately 2mm. This injector also produces droplets with a significantly smaller mean diameter (D10) with a maximum decrease in diameter of approximately 14μm. A diameter defect between the injector orifice wall and core of the spray seen for both sprays is found to be minimized by the countersunk design as well. It was also found that the average droplet velocities in the vertical direction deviate from the incoming air flow velocity to a lesser degree using the countersunk injector. Meanwhile, droplets from this injector have a higher average velocity in the direction of fuel injection between the core of the spray and the orifice wall.

CHAPTER 1

INTRODUCTION

Cross flow fuel injection is widely used in gas turbine engine combustors, thus it is important to understand the mechanisms that control the spray breakup, penetration and distribution within the cross flow. Such data is needed for validation of CFD codes that will subsequently be incorporated into engine design tools. Additionally, this information is needed for understanding observed engine performance characteristics at different regimes of the flight envelope and development of qualitative approaches for solving problems such as combustion instabilities[1]. A number of experimental studies of this problem under conditions that simulate those in real engines have been undertaken and are briefly reviewed below.

Literature Review

Spray formation studies have identified two modes of liquid jet breakup; i.e., the column breakup and the shear breakup. During column breakup, the liquid "column" develops surface waves which distort the liquid[2]. As the waves evolve down stream along the fuel jet, aerodynamic forces enhance the growth rate of the disturbances, leading to the formation of ligaments which subsequently break up into droplets[3,4,5,and 6]. In shear breakup, aerodynamic forces on the surface of the liquid jet strip off droplets by shear. The domination of one mechanism over the other is dependent upon the liquid to air momentum-flux ratio, q, and Weber number, We, which is a non-dimensional parameter and defined as the ratio of aerodynamic to surface tension forces. The column breakup mechanism dominates the formation of droplets[6,7,8] at low We and low q. Transition from column breakup to shear breakup can be caused by

increase in pressure or increase in shear velocity[9]. Shear breakup for turbulent liquid jets is enhanced by the internal liquid turbulence[6, 10]. Wu et al.[11] proposed a breakup regime on a map of aerodynamic Weber number (We) and the momentum-flux ratio (q). Rancher et al.[12] carried out studies at elevated pressures (1.5-15 bar) on Jet A fuel and found the breakup regime of column and shear breakup to match with the studies carried out by Wu et al.[11]. Mazallon et al.[7] have found that for values of momentum-flux ratio above 100, the dominant breakup mechanism is determined only by Weber number.

Jet penetration has received significant attention as well. Chen et al.[5] and Wu et al.[11,13] have carried out experiments at different momentum ratios of water jets and developed a correlation for the upper surface trajectory of jets in a crossflow against liquid to air momentum-flux ratio. Stenzler et al.[14] used Mie scattering images to find the effect of momentum-flux ratio, Weber number, and liquid viscosity on jet penetration. Like other previous studies, they found that increasing momentum–flux ratio increased penetration. Increasing the Weber number diminished the overall penetration by decreasing the average droplet size of the spray. Increasing the viscosity of the injection fluid decreased the penetration by increasing the drag force on the jet and causing it to bend more sharply. Tambe et al.[4] used pulsed shadowgraph images, picked points on the periphery of the jet manually and developed correlations using different functional forms of power-law, exponential, and logarithmic. They found that the logarithmic model was in best compliance with the results.

Leong et al.[15] have conducted studies of the spray of Jet A in a crossflow of air at 38 m/s for different ambient pressures (1, 3 and 5ata). They found that at a given jet to crossflow momentum-flux ratio, an increase in ambient pressure decreases jet penetration and increases breakup. Ahn et al.[16] have explored the effect of turbulent internal flow on the fuel flow. They

used cavitations and hydraulic flip to change the orifice internal flow. They found that the spray characteristics, like the liquid column trajectories, follow the correlations obtained by Wu et al.[11] in absence of cavitation and hydraulic flip, but in their presence, deviate from the correlations significantly. Thus they concluded that the internal orifice flow has a significant effect on flow characteristics.

Current Study

This study extends the study of injector induced turbulence into the regime of jet engine design. In spite of a lot of work done in this field, very few studies have been carried out under conditions typical of aerospace applications. Becker at al.[9] and Rancher et al.[12] carried out studies at elevated pressures, but at room temperature. This current study aims at investigating the spray in cross flow close to conditions in gas turbine combustors. In this study, the characteristics of the spray at different Weber number while leaving q the same was examined at conditions closer to real aerospace conditions than any other study. A parametric study of the spray in crossflow is conducted in order to examine spray formation at conditions close to jet engine applications.

The transition from multi-mode breakup to shear dominated breakup is also investigated and characteristics of the spray such as average droplet diameter and velocity are examined for their dependence upon We. Liquid fuel viscosity and evaporation are also major phenomenon that are of concern in the high heat environment within a jet engine and these phenomenon can be accounted for within the following results.

This study will also investigate the dependence of spray formation upon injector design. Two different injector designs will be used. One injector will be of a sharp edged design with an L/d ratio of approximately 10. The second injector will consist of smooth edges with an L/d of

approximately unity. Finally, a general goal of this study is to collect experimental data to validate CFD codes used to compute flow characteristics in turbine engine liquid fuel spray systems.

Experimental Setup

The experimental setup developed by Lubarsky et al. [18] for the investigation of liquid fuel injected in a crossflow was utilized for this research and is described in this section. Figure 1.1 shows a schematic of the experimental setup that has been developed at Georgia Tech to study the injection of jet fuel from a flat surface into the cross flow of preheated air at elevated pressures. This setup consists of a plenum chamber, rectangular air supply channel, test section containing injector under investigation, and pressurized chamber with three windows for optical access to the spray. The plenum chamber is cylindrical with a diameter of 6 inches and length of 18. Air is supplied to the plenum chamber from its top end through a system of 60 equidistant orifices 1/8 inch in diameter.

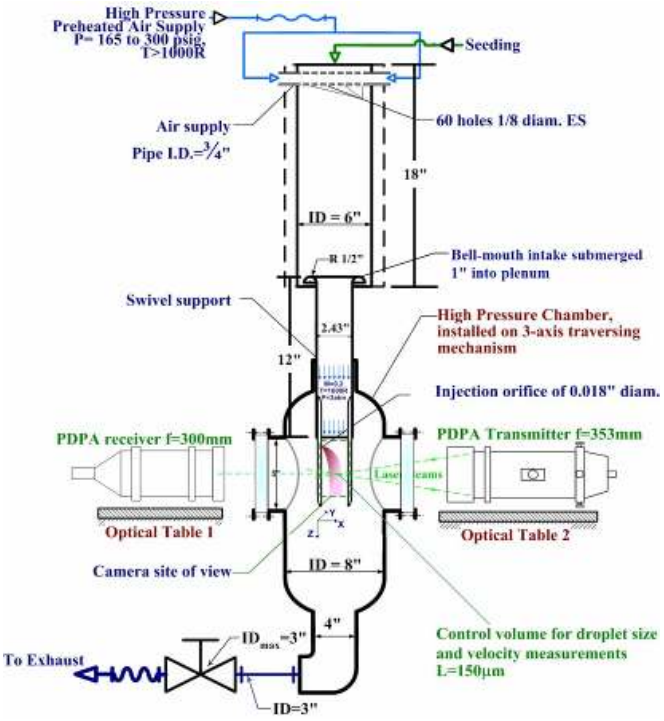

Figure 1.1: Schematic of Test Facility

The plenum chamber has an opening at its top to provide for the seeding of alumina particles (5 microns Al_2O_3) which are required for the characterization of incoming air using Micro-LDV. For this purpose, a small portion of the incoming air flow is bled through a seeder and replaced downstream of the grid of 60 injection orifices. The plenum chamber is thermally insulated to reduce heat losses. The cross section of the rectangular supply channel has dimensions of 2.43 by 2.43 inches. The length of the channel is 12 inches. The channel is equipped with a "bell-mouth" air intake, which is submerged by one inch into the plenum chamber at its bottom to smoothen the air flow.

(a) **(b)**

Figure 1.2: (a) Three-window test section (b) View of test section submerged in pressure chamber

The other end of the channel is submerged into the pressurized chamber. Two aerodynamically shaped plates are attached to the walls at this end of the channel creating a test section. A fuel injection orifice 0.018 inches in diameter is located on the centerline of the plate 11 mm downstream of the supply channel termination. Two quartz windows 1/8 inches thick are fixed in the slots of the aerodynamically shaped plates using Teflon gaskets. A third quartz window has been mounted in an orthogonal test section wall for the analysis of additional velocity components (See Figure 1.2a). Such design of the test section provides full confinement of the air flow in the spray region as well as optical access for the characterization of the spray and the incoming air flow upstream of the injection orifice in all desired planes. Figure 1.2b shows the test section submerged within the pressure chamber. The dimensions of the rectangular test section are 30mm by 46mm (from plate to window and from window to window

respectively). The length of the quartz windows is 3 inches. The tail edges of the plates are aerodynamically terminated 0.5 inches downstream of the windows.

The entire assembly, including the plenum, rectangular supply channel and test section, is installed on a sealed swivel support located on the top of the pressurized chamber (8 inches in diameter, 36 inches long) in such a way that the thin (1/8 inches) quartz windows of the test section are aligned with the thick (1 inch) windows (5 inches in diameter) of the pressurized chamber. The swivel support allows the test section to be rotated 360 degrees about it's axis to redirect the spray (in different experimental runs) with respect to the transmitter and receiver of the PDPA.

Two windows of the pressurized chamber are at an angle of 150 degrees with respect to each other to provide optical access for the transmitter and receiver of the PDPA system that was used to characterize the spray in forward scattering mode. This allowed for the measurement of droplet velocities along the X and Z axes (axes described in following section). The third window of the pressurized chamber is at an angle of 105 degrees with respect to the transmitter's window. This window was used for operating the PDPA system in 90 degree scattering mode. This mode enabled the measurement of the third component of droplet velocities along the Y axis.

The pressurized chamber is designed to withstand an internal pressure up to 200psi. In the reported experiments, pressure in the chamber was typically 58.5 psia (4ata). The exhaust line is a stainless steel flexible tube 4 inches in diameter. The exhaust is equipped with a throttle valve that opens to a maximum of 3 inches. The line is connected to the laboratory ejection exhaust pipe via a muffler. Air supply and fuel lines are flexible as well.

The whole system is installed on a traversing table, which provides precise movement (minimal step is 12.5 microns) in three mutually orthogonal directions using step motors and electronic drivers connected to the PDPA computer. The transmitter and receiver of the PDPA system are attached to optical tables which are locked to the frame of the rig. In the current study, 1mm increments of movement were typically used for the characterization of spray and

the core of the incoming air flow. Meanwhile, the micro-LDV system was traversed in steps of 12.5 microns for the characterization of the incoming air flow within the boundary layer.

Preheated air was supplied to the test rig from the laboratory high-pressure system (P_{max}=720psi, T_{max}=555K) which automatically maintains constant pressure and temperature (as set on an electronic control panel) at the entrance to the test cell. The high pressure air is initially stored in 14 high-pressure, 2500 psia (17.24 Mpa) cylinders. From there, the air passes through an air-heater then flows directly into the high-pressure test cell that houses the experimental apparatus. The laboratory high-pressure air storage system (14 Cylinders) was able to supply the experiment with constant pressure and temperature air during ~70 and ~25 minutes at M=0.2 and 0.35 respectively. The pipes leading to the test cell are insulated to minimize heat losses. The pipes are also heated with electrical tape heaters to compensate for any heat loss. Stabilizing the temperature in the test facility at the operating temperature (555K) was an iterative process meant to achieve and maintain the set temperature while minimizing the amount of high pressure air spent on preheating the system. In the reported experiments, a control system was used to maintain the air pressure and temperature at P_0=150-300psia and T=555K, respectively. At these air pressures and temperature, Mach number through the test section was varied from M=0.2 to M=0.35 while pressure was maintained at 4 atm for the characterization and Weber study and 5 atm for the injector comparison.

Control of the Mach number and pressure is provided by variation of the pressure supplied to the test cell and by the simultaneous variation of the throttle valve opening in the exhaust line. The Mach Number of the air flow is monitored using a combination of static and total pressure probes installed in the rectangular air supply channel about 6 inches upstream of the fuel injection orifice (see Figure 3). A static pressure sensor (OMEGA Px303-100G5v - 100psig) is connected to the static pressure port on the wall of the test section. A differential pressure sensor (PX656-200DI - ΔP=7.5 psi) is connected by a high pressure (HP) port to the total pressure port located in the middle of the rectangular channel cross-section. The low pressure (LP) port of the differential pressure sensor is connected to the static pressure sensor as

well (Figure 1.3). Electronic measurements of static and differential pressure were backed up by simple mechanical gauge devices to ensure the reliability of the experimental data.

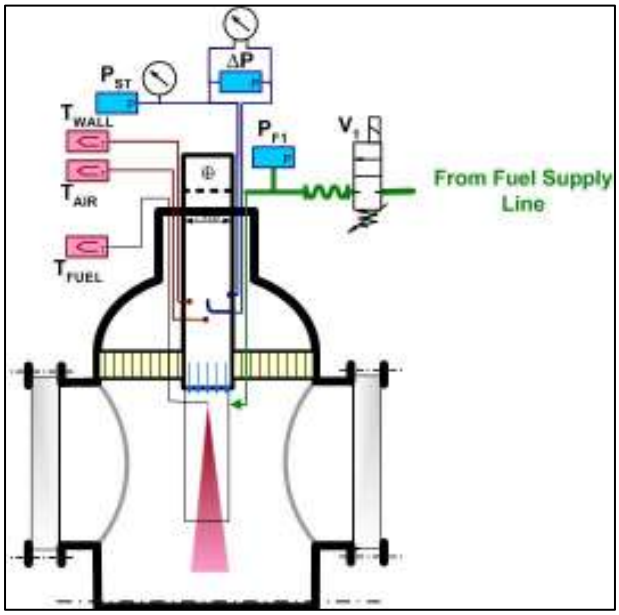

Figure 1.3: Instrumentation of Facility

Air temperature was measured using a K-type thermocouple, 1/16 inches in diameter, which protrudes from the side wall to the center of the rectangular cross-section, 1.4 inches upstream of the fuel injection orifice. The temperature of the rectangular channel's wall was measured by a 1/16 inch diameter K-type thermocouple with its tip welded into a dead end hole (about 1/16 inches deep) in the longer (2.43 inches) wall of the channel (~1/8 inches thick).

Jet-A liquid fuel was supplied to the injection orifice using a channel 1/8 inch in diameter drilled through one of the two aerodynamically shaped panels. A schematic of the fuel supply system is shown in Figure 1.4. Fuel was supplied from an outdoor, 60- gallon tank through an air-powered fuel pump (MAXIMATOR LSF15-2), which provided the required pressure head to reach the momentum ratios of 40 at M=0.35 (more than 1300 psig at 11 g/sec flow rate of Jet-A). The fuel tank was pressurized to about 60 psig (from a Nitrogen cylinder through a regulator) to prevent fuel cavitation at the pump inlet. A bladder-type accumulator (V=1 gallon) is attached to the pump discharge line to absorb the hydraulic shocks created by the pump stroke.

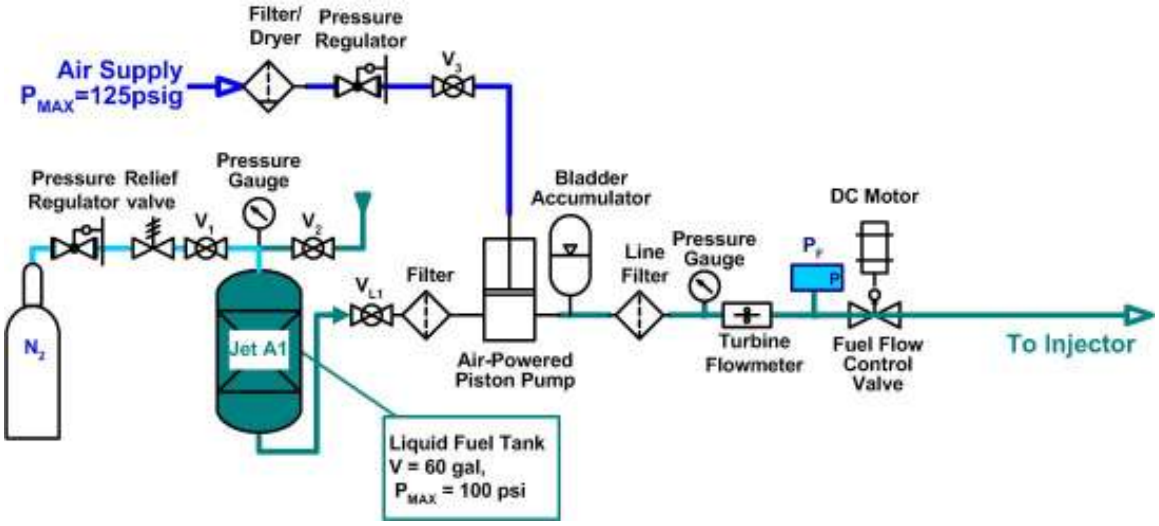

Figure 1.4: Schematic of Fuel Supply

Experiments with momentum-flux ratio of 40 at M=0.2 were supplied without active pumping (pump off). In these experiments, the fuel tank was pressurized to 160 psig. This combination of the tank, pump lines, and bladder accumulator design parameters assured the proper operation of the fuel control unit at both of the required flow rates for a momentum ration of 40 at M=0.2 and 0.35. The fuel flow control valve was actuated by a dial on the instrumentation panel.

The fuel flow rate was measured using an FTB-9504 turbine flow meter equipped with a FLSC-62 loop powered 4-20 mA OMEGA transmitter. The FTB-6071E flow rate meter (OMEGA) outputs an AC voltage signal which has a frequency equal to the rate of spin of the turbine. With a known density of fuel, the frequency signal is converted to a mass flow rate reading inside the flow rate meter. The latter generates a current signal which is passed through a low-pass filter and turned into a voltage signal proportional to the fuel mass flow rate. Pressure (P_{F1}) and temperature of the fuel supplied to the injection orifice were monitored and recorded during the test. Fuel pressure was measured by an OMEGA P303-1K5v (1000psig) transducer. The temperature of the fuel at the point of its injection was measured by the 1/16 inch diameter K-type thermocouple penetrated into the fuel channel drilled through the aerodynamically shaped plate directly under the injection orifice.

The thermocouple and pressure signals are displayed on an instrumentation and control panel by DPI-8A (OMEGA) display devices. The displays act as signal conditioners for the voltage connections to the computer data acquisition (DAQ) board. The flow rate measurements are displayed upon the FTB-9504 (OMEGA) before entering the DAQ board.

All signal cables are physically connected to a BNC-2090 (NATIONAL INSTRUMENTS) board. The signals run from the board into the computer and are measured, displayed, and saved. The computer DAQ card is a PCI-6071E (NATIONAL INSTRUMENTS). The computer calculates the following quantities from the pressure, temperature, and fuel flow rate voltage signals: free stream Mach number, velocity of air, mass flow rate of air, density of air, fuel velocity, Weber number, and momentum ratio.

Coordinate System

The axes used to orient the measurements are centered at the orifice. The three mutually orthogonal directions (*X*, *Y*, and Z) are aligned as shown in Figure 1.5. The positive X-axis points in the direction of fuel injection, the Z-axis points in the direction of incoming air and the positive Y-axis is on the plate having the orifice forming a left handed coordinate system. X-scans refer to the measurement of velocity components while moving in the X-direction.

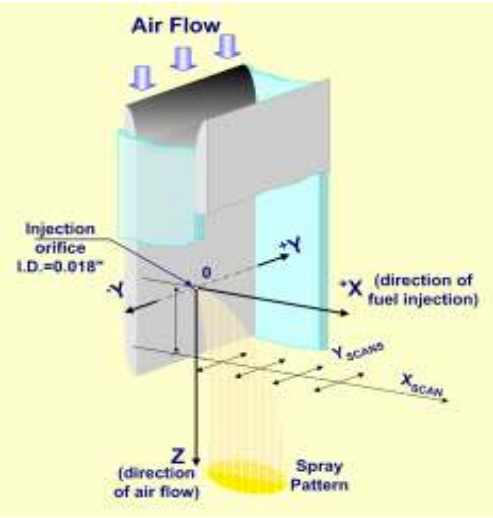

Figure 1.5: Coordinate System

Diagnostic Techniques

Phase Doppler Particle Analyzer

A two-component PDPA (TSI Inc.) was used to measure the diameter and velocities of fuel droplets within the spray. The PDPA system consists of transmitting optics (Model 450500) with a focal length of 500mm and receiving optics (Model 450300) with a focal length of 300mm, both installed on stationary tables. The receiving optics are connected to a photo-detector module (Model PDM 1000) using fiber-optic cables. Photomultiplier signals are processed using a multi-bit digital processor (Model FSA 3500). To generate the laser beams which create the optical measuring volume of the PDPA, an INNOVA 90 water-cooled, argon-ion laser, beam splitter and Brag cell were used. The laser provides 0.8 W green (λ = 514.5 nm) and 0.3 W blue (λ = 496.5 nm) beams.

To measure the incoming air velocity, the air was seeded with alumina particles (of diameter around 5 microns) and the PDPA was operated in LDV mode. When seeding the particles, a part of the inlet air was bled into a cylindrical chamber containing finely powdered Alumina before being released into the pressure chamber. The seeding level was controlled using a control valve which changed the air flow rate into the seeder. The data obtained was analyzed using the *Flowsizer* software. This software is also used to compute the D_{10} (arithmetic mean diameter) and D_{32} (Sauter mean diameter) sizing of the droplets within the spray along with the mean velocity and the root mean square (RMS) velocity of the droplets.

Micro-LDV

Figure 1.6a shows a schematic of the micro-LDV setup developed by Lubarsky et al. [19] for boundary layer study. There are two approaches for increasing the resolution of LDV systems. One involves reducing the thickness of the laser beams used. This reduces the dimensions of the control volume used for interrogation. The other approach is to magnify the existing control volume and collect data from a fraction of that volume. This method has been

followed in this study wherein a long distance microscope is used to zoom into the control volume of the LDV system and measure particle velocities in a cylindrical region of radius of 12.5 microns and depth of about 5 microns. The lens used for this purpose is a QUESTAR QM1 with a microscopic objective (Figure 1.6b). The resulting image is fed into the LDV analyzer and the particle velocities are recorded. This method reduces the rate at which data is acquired due to reduced control volume and hence data acquisition has to run for a longer time than usual. This setup combined with the traverse and its smallest traversing step of 12.5 microns gave a very good resolution for making boundary layer measurements.

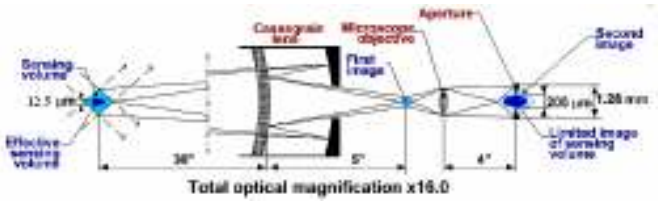

(a)

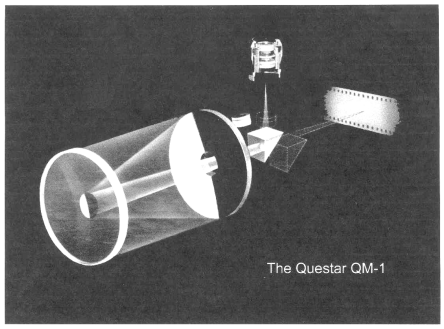

(b)

Figure 1.6: Micro-LDV System (a) Schematic of Micro-LDV setup (b) Lens used for Micro-LDV

Macro-Image Technique

Figure 1.7 shows a schematic of the facility used for imaging the entire spray (macro images). A Metalaser Technology MTS-20 pulsed Copper Vapor laser with pulse frequency of 6 kHz and pulse duration of 30ns was used to back illuminate the spray. A mirror was fixed in the background of the spray such that the laser that is incident on the mirror, is reflected in the direction of the camera making imaging of the "spray shadow" possible.

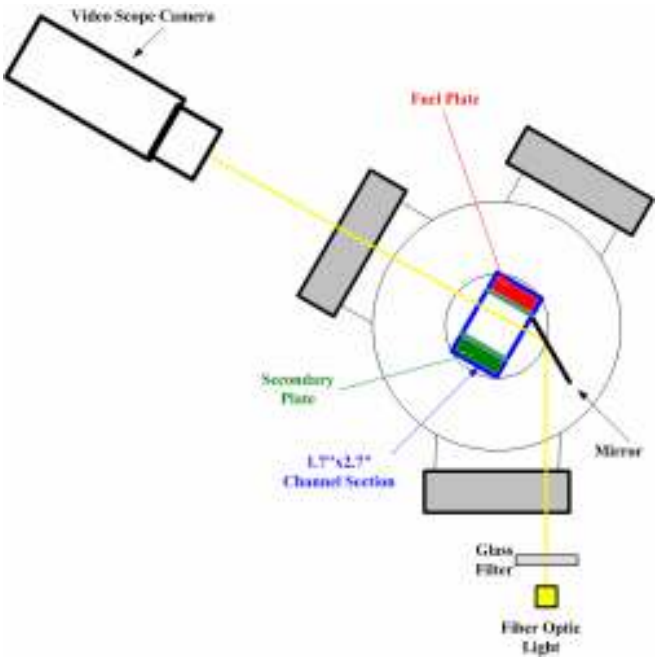

Figure 1.7: Schematic of Spray Imaging Apparatus

The angle between the two windows used for this purpose is 105^0. A Foculus FO531B CCD camera of resolution 1628 x 1236 is used at frame rate of 10Hz to capture spray images. The exposure time of the camera should be lower than the duration between two consecutive laser pulses so that the images are captured within one laser pulse. Also both the intervals should be close to each other so that most of the frames have an image (if the exposure time of the camera is much lower than the duration between pulses, the probability of the camera capturing an image during the laser pulse is less and many frames will not have any image at all). The duration between two consecutive laser pulses is 166.6 microseconds. The exposure time of the camera is chosen to be 160 microseconds which is marginally lower than the time interval between two laser pulses.

Imaging sessions routinely produced nearly 250 images of the spray at each condition. The macro images give the researcher a physical representation of the spray that can be qualitatively analyzed for a better understanding of spray phenomenon occurring along the entire

fuel-air mixing length. More importantly, these images can be used to physically validate the data being recorded by the PDPA system.

Image Processing Technique

Macro images of the spray were taken in their raw form and then flattened with *MaximDL* imaging software to eliminate random noise due to the experimental setup. Essentially, the background of the image was subtracted from the spray images. This process produced cleaner images for image processing then those used in previous research. Figure 1.8 shows an example of a flattened image and it is seen that significant random noise has been eliminated in the area of the spray. These flattened images are then processed to evaluate the spray's trajectory.

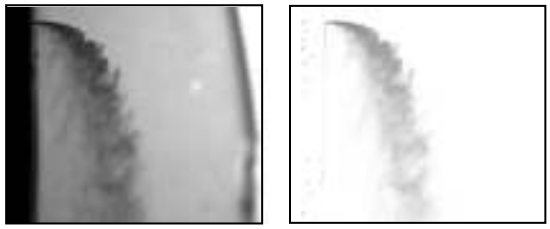

Figure 1.8: Raw image (left) and Flattened image (right) for noise reduction

In order to validate the PDPA data, a measurement of each spray's outer edge was required. For this, an edge detection routine was developed using *Matlab* computing software. This routine analyzed 90 images of each spray. For each image, the outer edge of the spray was designated and plotted then all 90 outer edges were superimposed upon one another to create a 90 image superposition which was then used to compare the trajectories from the PDPA data. 10% of the maximum volume flux measured was used as the measure of the location of the end of the trajectory of the spray. The volume flux constitutes the entire volume of liquid passing through the microscopic control volume utilized by the PDPA system for measurement. By this, the maximum value of volume flux should represent the core of the spray. The 10% volume flux was found by plotting volume flux data taken for each spray using the PDPA system and processing this data using *Matlab*. The *Matlab* curve-fitting software was used to fit 9^{th} and 10^{th}

order polynomials to the data. These polynomials were then evaluated using *Matlab* to find the X location of the maximum volume flux and 10% threshold.

Incoming Air Flow Characterization

Understanding the characteristics of the incoming air flow without fuel injection is required in order to assess both the uniformity of the air flow and analyze the effect fuel injection may have upon the air flow. The LDV system was used for measuring the axial velocity of the incoming air flow. The flow was seeded with alumina particles of diameter around 5 microns because the LDV system is only capable of measuring particle velocities, not the velocity of the flow itself. The particles were first heated in an oven to avoid clustering of particles and seeded as explained previously. The seeding level was adjusted by using the control valve to obtain an acceptable Doppler burst rate.

Characterization of the incoming air flow was performed by measuring the axial velocity in two X-Y planes with the LDV system operating in 150° forward scattering mode. One plane was chosen to be 5mm upstream of the orifice and the other one 20mm downstream. The fuel to air momentum ratio for these measurements was 180. X-scan measurements were completed at Mach numbers of 0.2 and 0.35 at Y=0 in both the planes chosen. For the same Mach numbers, Y-scan measurements were carried out at a distance of 10mm from the orifice plate (X=10mm). All of the scans were made using a step size of 1mm. To check the extent of the effect of spray on the incoming air flow, Y-scan measurements of the axial velocity were made 2mm and 5mm upstream of the fuel injection orifice. For this purpose, the distance from the plate was chosen to be 3mm (X=3mm). Operating conditions for characterization of the incoming air flow are listed in Table 1.1.

Table 1.1: Operating Conditions for Characterization of incoming air flow core

Mach Number	0.2	0.35
Pressure in the chamber	4 atm	4 atm
Temperature of air	555 K	555 K
Mass flow rate of air	0.665 kg/s	1.18 kg/s
Velocity of air	93.5 m/s	165 m/s
Reynolds Number of air	5500	9600

Micro-LDV was then used to measure the velocity profiles within the boundary layer of the air flow at locations of 2, 5, 7.5, and 10mm upstream of the injection orifice at the operating conditions listed in Table 1.2.

Table 1.2: Operating Conditions for Boundary Layer Investigation

Mach Number	0.2
Pressure in the chamber	4 atm
Temperature of air	276-280 K
F/A Momentum-flux Ratio	40

Incoming Air Flow Characterization Results

It is necessary to know the characteristics of the incoming air flow to understand the spray dynamics. It is also of interest to know how far upstream of the orifice the spray influences the incoming air flow. Velocity profiles in the presence and absence of spray were compared to investigate the influence of spray on the incoming air flow characteristics. For this purpose, two cross-sections located at the distance 5mm and 2mm upstream of the injection orifice were chosen. Another cross section 20mm downstream of the injection orifice was chosen to check the stability of the flow along the test section. The fuel to air momentum ratio used was 180.

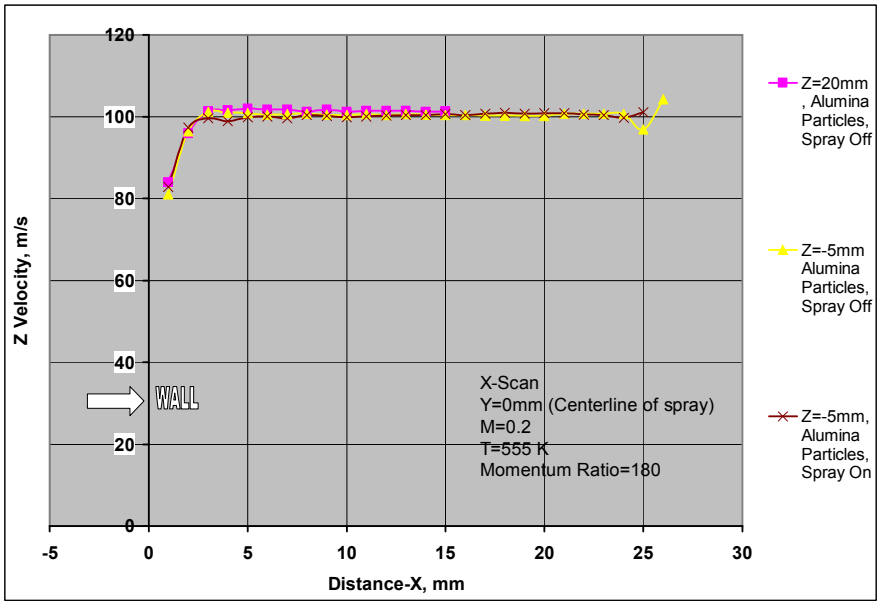

(a)

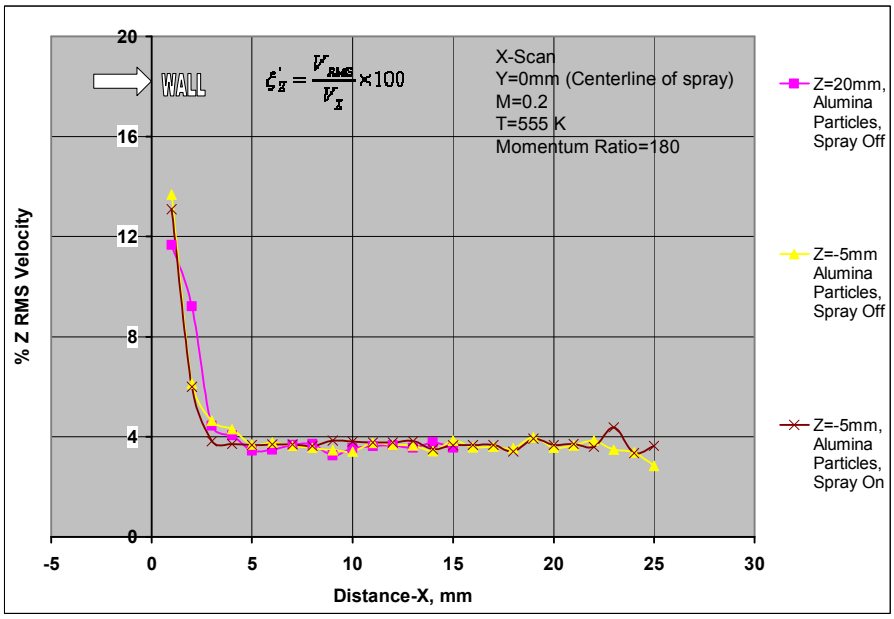

(b)

Figure 1.9: (a) Axial Velocity profiles along the wall normal direction at M=0.2 (b) RMS Velocity profiles along the wall normal direction at M=0.2 (c) Axial Velocity profiles in the y direction at M=0.2 (d) RMS Velocity profiles in the y direction at M=0.2

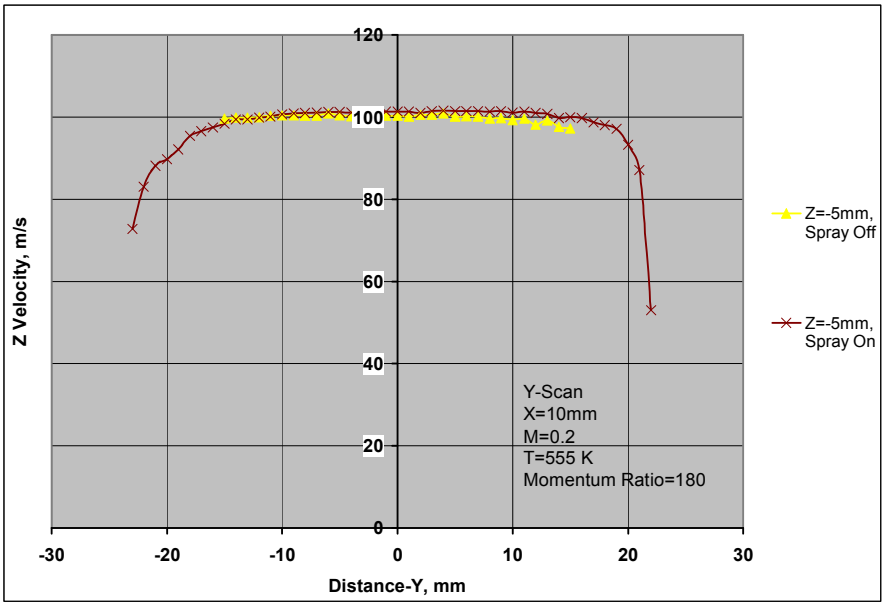

(c)

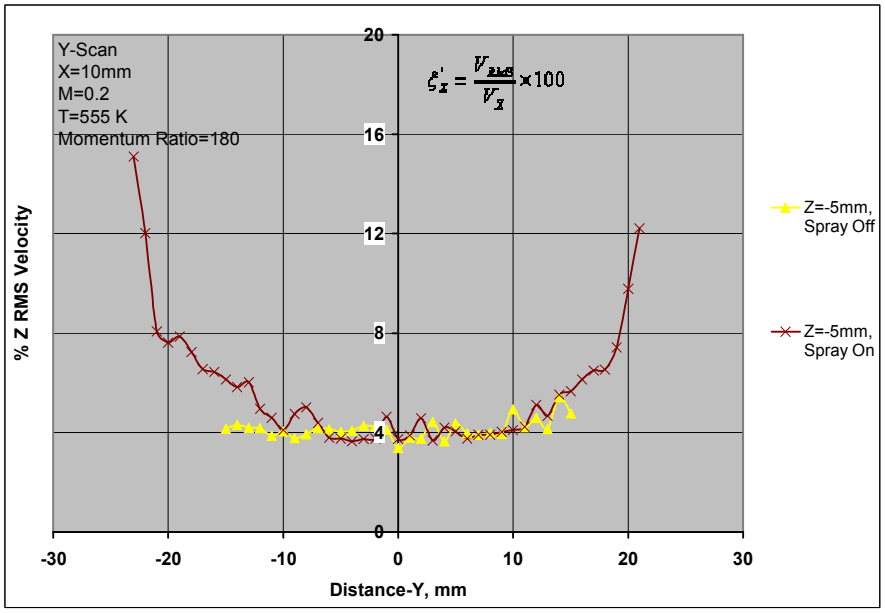

(d)

Figure 1.9: continued

Figure 1.9a shows the axial velocity profiles measured at 5mm upstream of the orifice in the presence and absence of fuel injection along the X-direction. For the case of 20mm downstream of the orifice, the axial velocity profile shown corresponds to the absence of spray. As seen in the graph, the velocity profiles for the three cases do not differ from one another

significantly. The measured average axial velocities do not differ by more than 1% in the core of the flow, which is within the limits of experimental error. Figure 1.9b shows the RMS velocity corresponding to the mean velocities shown in Figure 1.9a. The RMS velocity is around 4% of the mean velocity in the core region. Figure 1.9c shows the velocity profiles measured at 5mm upstream of the orifice in the Y-direction (i.e., along the plate) at a distance of 10mm from the plate containing the injection orifice. The uniform average value of the axial velocity remains within 1% on the distance of 10-12mm from the centerline in both Y directions. Figure 1.9d shows the RMS velocity corresponding to the mean velocities shown in Figure 1.9c. Again, the RMS velocity is found to be around 4% of the mean velocity in the core region. The thickness of the boundary layer near the plate containing the injection orifice does not exceed 3mm. Velocity profiles near the window reveal a thicker boundary layer of about 9-11mm.

Figure 1.10(a-b) shows the axial velocity and RMS velocity profiles in the X-direction at the same locations but at M=0.35. The velocity defect due to the spray lies within 1% of the mean velocity at 5mm upstream of the orifice. Again, the boundary layer near the orifice plate does not exceed 3mm. The RMS value is, again, typically around 4% in the core region.

Figure 1.11a exhibits the effect of spray on the incoming air flow. It shows the axial velocity profiles along the Y-direction (along the plate) as measured at M=0.2. Y-scan measurements are made at two locations, 2mm and 5mm upstream of the orifice at a distance of 3mm from the orifice plate. It is seen that the maximum difference between the axial velocities for the cases of presence and absence of spray is around 5m/s (around 5% of mean velocity) at 2mm upstream of the orifice. For the 5mm upstream case, the change in velocity did not exceed 1% of the mean velocity which is within the limits of experimental error. Figure 1.11b shows the RMS velocities at the same locations. In general, they are typically around 4% of the mean velocities except for the region of high influence of the spray which is at Y=0 and 2mm upstream from the orifice. Measurements made at M=0.35 (Figure 1.12 a-b) show similar results.

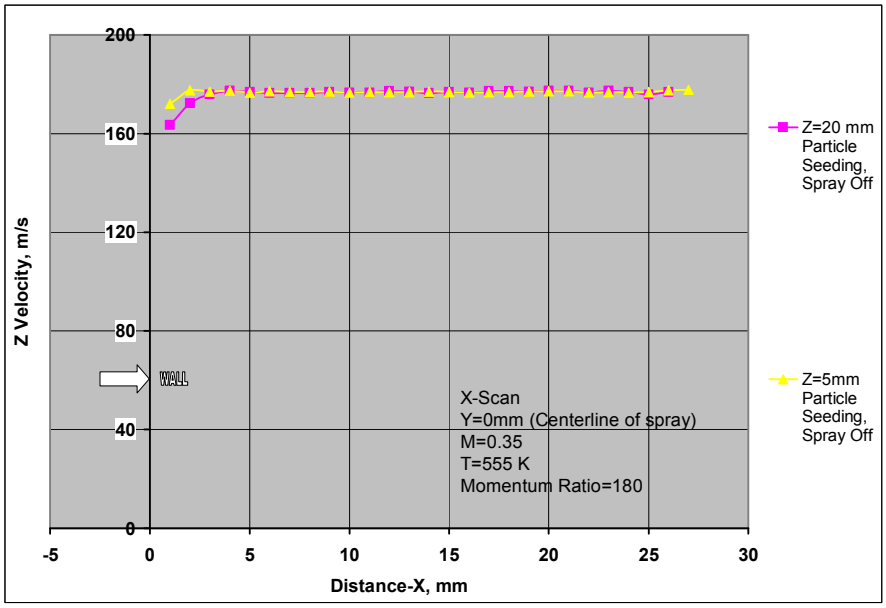

(a)

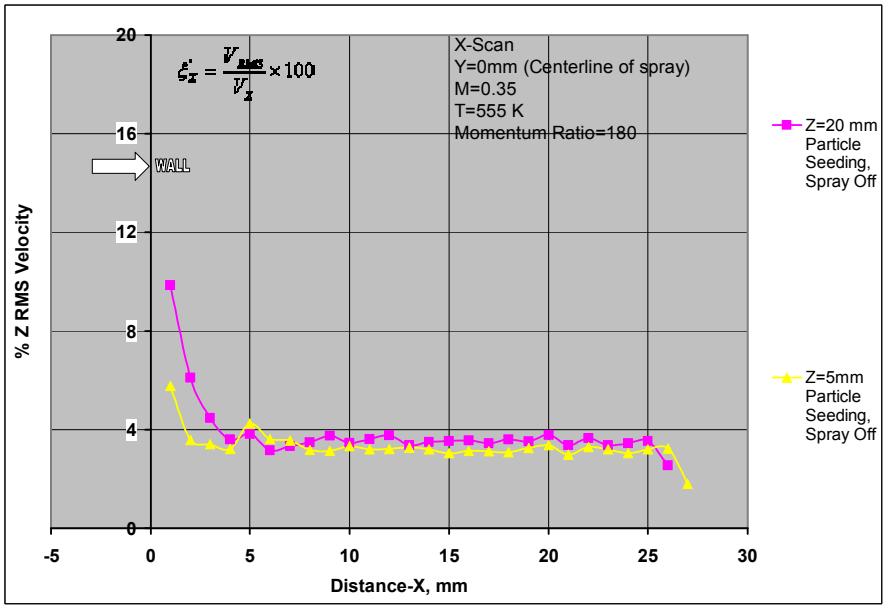

(b)

Figure 1.10: (a) Axial Velocity profiles along the wall normal direction at M=0.35 (b) RMS Velocity profiles along the wall normal direction at M=0.35

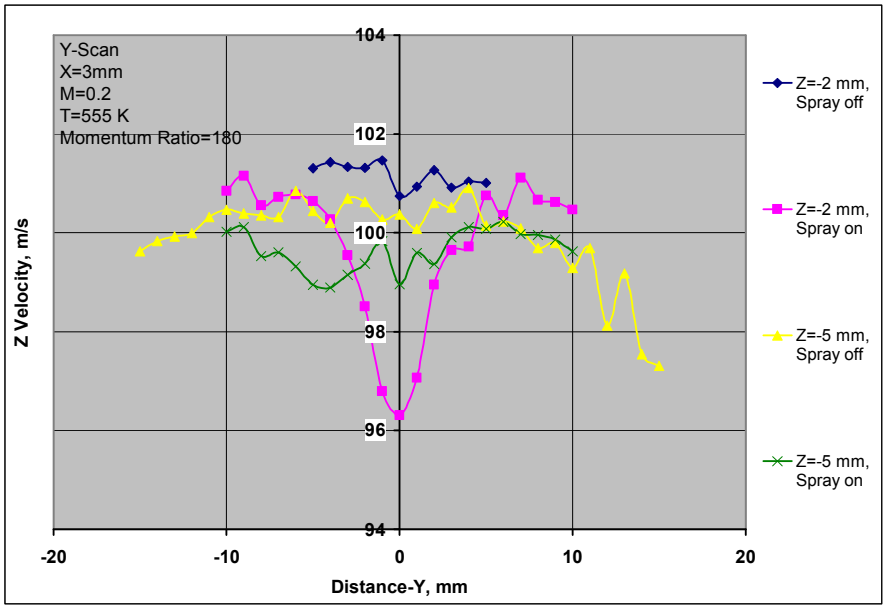

(a)

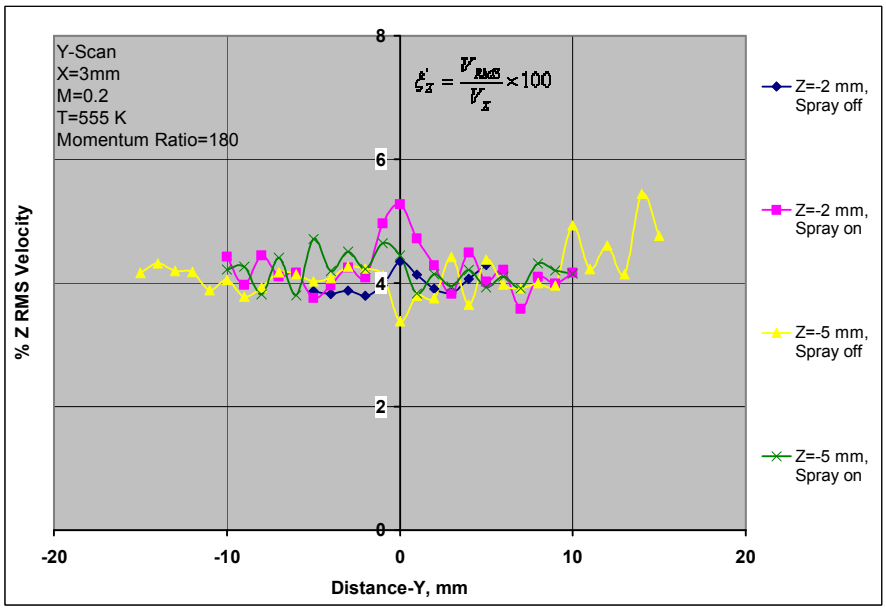

(b)

Figure 1.11: (a) Comparison of Axial Velocity profiles at locations 5mm and 2mm upstream of the orifice, M=0.2 (b) Comparison of RMS Velocity profiles at locations 5mm and 2mm upstream of the orifice, M=0.2

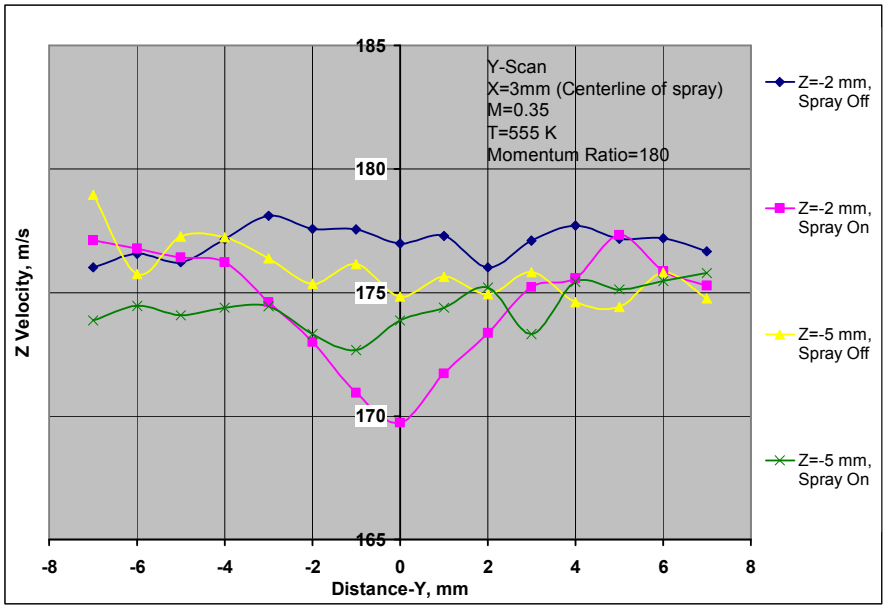

(a)

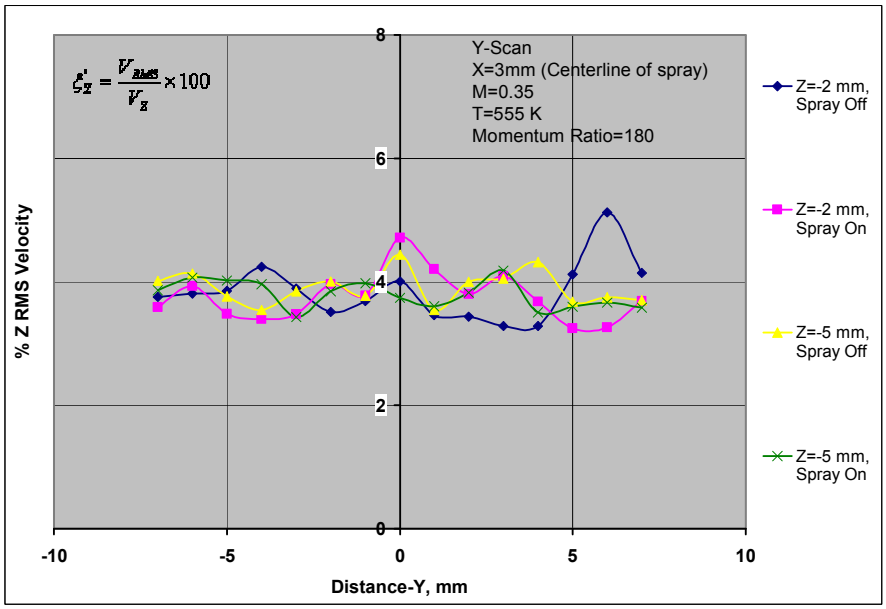

(b)

Figure 1.12: (a) Comparison of Axial Velocity profiles at locations 5mm and 2mm upstream of the orifice, M=0.35 (b) Comparison of Axial Velocity profiles at locations 5mm and 2mm upstream of the orifice, M=0.35

Combining the results of the X-scan and the Y-scan, it can be said that the effect of the spray on flow characteristics 5mm upstream of the orifice is not significant. On the contrary, significant effect of the spray on velocity profiles is observed at 2mm upstream of the orifice.

The measured velocity profiles are typical of turbulent flows. The flow Reynolds Numbers are 5500 (at M=0.2) and 9600 (at M=0.35). The observed RMS velocity is around 4% of the mean velocity and the boundary layer on the plate with the injection orifice measures about 3mm across. The boundary layer near the window is thicker, but the spray is completely encompassed in the core region of the flow. The characteristics of the incoming air flow at a plane located 5mm upstream of the orifice are fairly independent of the spray and hence the plane can be treated as a boundary for CFD codes. The flow is uniform and stable in the region of interest.

Boundary Layer and Spray Effect

This segment extends the work from the previous section into the boundary layer. Velocity measurements were made in the boundary layer of the flow. A Mach number of 0.2 was chosen for the boundary layer measurements for the current study.

Figure 1.13 shows the average Z velocity component profiles measured at Z locations of 2, 5, 7.5 and 10mm upstream of the orifice. It is seen that the effect of spray on the incoming air flow is significant at Z locations up to about 7.5mm upstream. The Z location of 10mm upstream shows a negligible effect of spray upon the boundary layer characteristics. This location corresponds to a z/d ratio of about 23. Hence, while choosing a computational domain, a z/d location of about 25 can be chosen to begin the computations for the flow conditions mentioned earlier. The boundary layer thickness is seen to be approximately 3mm from the orifice plate.

Figure 1.14 shows the RMS values of the velocity within the boundary layer in the Z direction. From these plots of the Z RMS profile within the boundary layer at several Z locations upstream of the orifice, it can be seen that the spray has very little effect upon the boundary layer

past about 7.5mm upstream of the orifice and is seen to be negligible at 10mm upstream. This validates a z/d location of about 25 as a suitable point to begin computations for the current flow conditions.

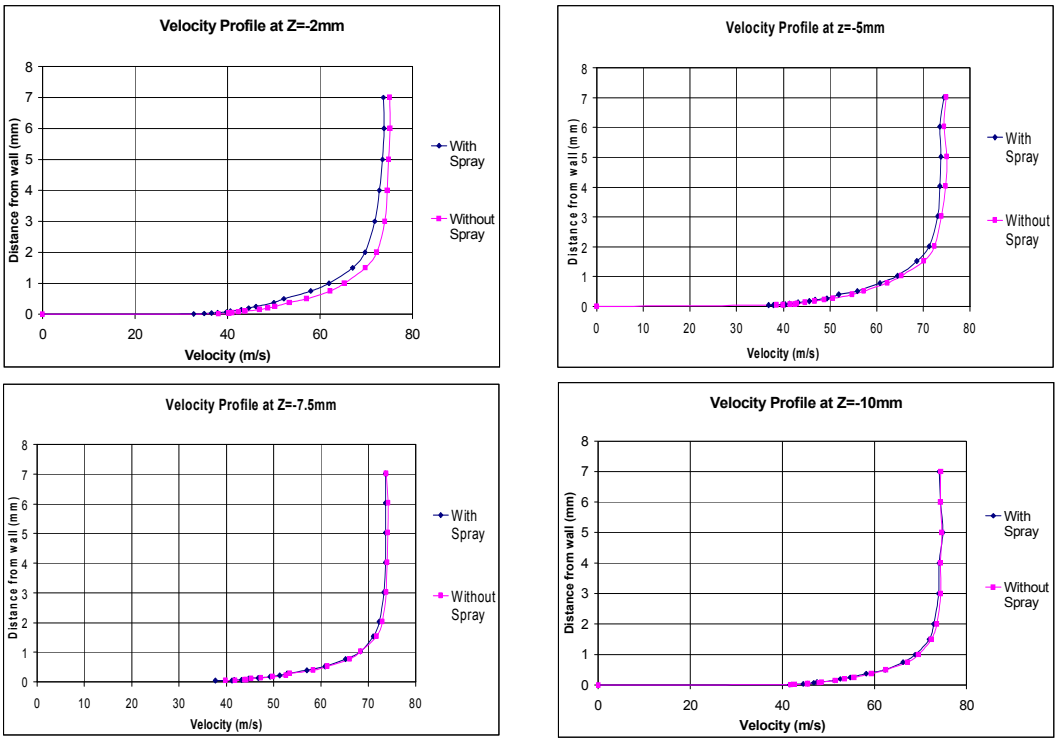

Figure 1.13: Avg. Velocity profiles near orifice plate (effect of spray)

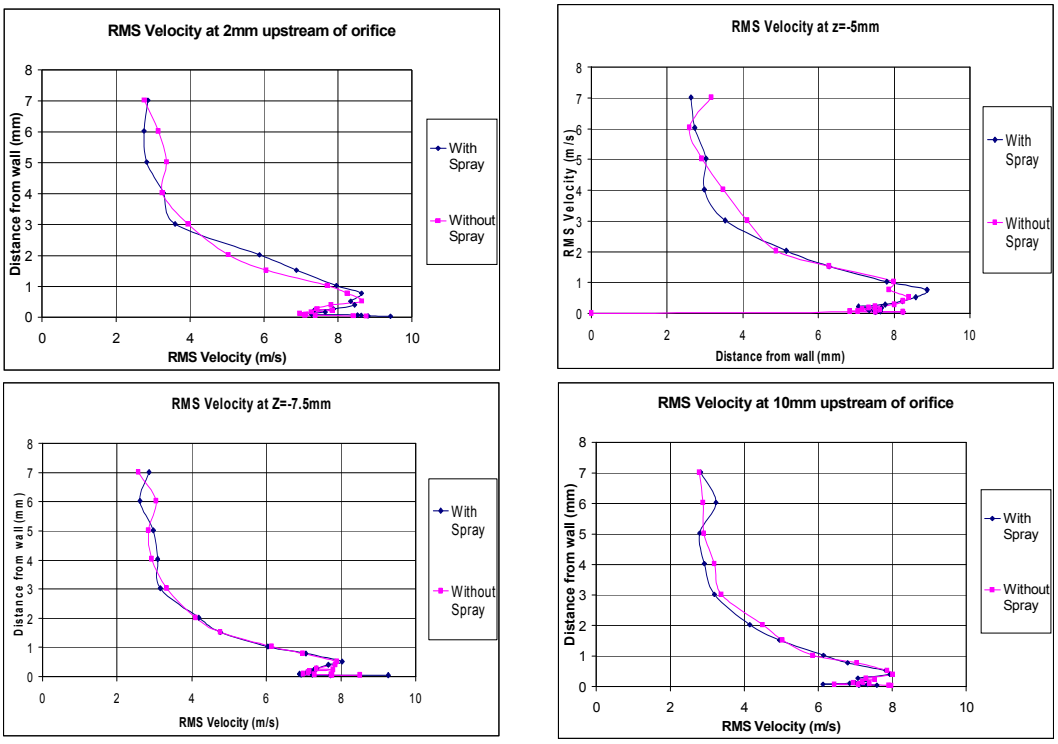

Figure 1.14: RMS Velocity Plots near orifice plate (effect of spray)

CHAPTER 2

SPRAY CHARACTERIZATION

Operating Conditions

The droplet velocities in three directions (along Z-direction, X-direction, and Y-directions) as well as droplet sizes were measured using the two-component PDPA system in 2 different modes. The valve for the alumina particle seeder is turned off for this study. Again, the 150^0 forward scattering mode of the PDPA system was used for the measurements of Z and X velocities as well as droplet diameters while the 90° scattering mode was used to obtain measurements of the Y and Z velocities. For M=0.2, the momentum ratio of 40 was maintained without active pumping by pressuring the fuel tank to 160 psig. For M=0.35, the fuel tank is pressurized to 60 psig using a nitrogen cylinder and a fuel pump is also operated to maintain the required pressure head for momentum ratio of 40. First, X and Z components of droplet velocities as well as diameters were measured in increments of 10mm downstream of the orifice (Z=10, 20, 30, 40, 50mm) for Mach numbers of 0.2 and 0.35 and a momentum ratio of 40. After completing these measurements, the rectangular test channel was the rotated 90 degrees for the measurement of the Y and Z components of droplet velocities. The traverse was moved and measurements were taken in steps of 1mm creating a 1mm by 1mm grid for all five investigated planes. Operating conditions for the characterization of the spray are listed in Table 2.1.

Table 2.1: Operating conditions for study of characteristics of spray

Mach Number	0.2	0.35
Pressure in the chamber	4 atm	4 atm
Temperature of air	555 K	555 K
Mass flow rate of air	0.665 kg/s	1.18 kg/s

Velocity of air	93.5 m/s	165 m/s
Momentum Ratio	40	40
Pressure of fuel	281 psi	917 psi
Mass flow rate of fuel	5.97 g/s	10.5 g/s
Temperature of fuel	323-328 K	323-328 K
Reynolds Number of air	5500	9600
Reynolds Number of liquid	22000	39000
Weber Number	570	1700

(Table 2.1 continued)

Characterization Results

This study of the spray patterns created by jet-A fuel injection into a cross-flow of preheated air (M=0.2, M=0.35, T=555K) primarily consists of three segments. This first is a data set of droplet velocities and diameters that could be used to validate CFD codes and to understand some of the physical phenomena occurring in the formation of droplets within a jet fuel spray of momentum ratio equal to 40. The second segment (Chapter 3) deals with the effect of the flow Weber number upon spray characteristics. The third segment (Chapter 4) investigates the influence injector design has upon spray characteristics.

Spray Characteristics

This segment discusses the characteristics of the droplets first at Mach numbers of M=0.2 and M=0.35 and fuel to air momentum ratio of q=40. Axial (Z) and wall normal (X) velocity components as well as droplet sizes in Arithmetic Mean Diameter (AMD) and Suater Mean Diameter (SMD) were measured at 5 different Z locations downstream of the injection orifice in increments of 10mm (Z=10, 20, 30, 40, 50mm) using the 2-component PDPA system in 150 degree forward scattering mode. After completing this series, the rectangular test channel was rotated 90 degrees and the PDPA system was operated in 90 degree scattering mode to obtain the

Y velocity component of the droplets. All images referenced in this section can be found in Appendix A.

Diameters

For the purposes of this discussion, Figure A.1 will be referenced as an example of droplet diameters in one Z-plane at M=0.2. These comments will serve as a basis for further analysis at both M=0.2 and M=0.35. Figure A.1a shows the Arithmetic Mean Diameters (AMDs) of droplets at Z=30 while Figure A.1b shows the Sauter Mean Diameters (SMDs) at the same location. The AMDs range from approximately 22 microns to 42 microns and the SMDs range from approximately 25 microns to 49 microns. It can be seen that both the AMDs and SMDs increase in a nearly linear fashion as the X-location moves away from the wall. It is also interesting to note that the largest AMDs and SMDs can be found at the periphery of the spray while the center-line region of the spray displays the smallest diameter droplets. Further analysis of 3-D plots reveal an interesting difference between these diameters at M=0.2 and M=0.35.

Figure A.2 shows the Arithmetic Mean Diameter (D10) of droplets at M=0.2 for the 5 different Z locations mentioned previously. As was seen in Figure A.1, larger drops are seen at the periphery of the spray. It is seen that the AMDs increase almost linearly with distance from the wall for Z locations of 20, 30, and 40mm. However, at Z=10mm and Z=50mm, the distribution is not linear. The AMDs increase as the X location moves away from the wall in all cases. Figure A.3(a-e) illustrates this increase in AMD away from the wall more clearly with a view along the x-axis (side profile) of the droplet AMDs in the spray. Figure A.3 also more clearly shows the non-linear distribution of diameters at Z=10 and 50mm.

The Sauter Mean Diameters (D32) are also of interest in this study. Figure A.4 shows that at each Z location, the SMDs at M=0.2 follow nearly the exact same trend as the AMDs. SMDs increase away from the wall and larger diameter drops can be found on the periphery of the spray. The only difference seen between the SMD and AMD values is the fact that the SMDs are higher than the AMDs at each point. This difference can be accounted for in the

method of SMD calculation. SMDs are volume-weighted diameters. This method of calculation gives the small amount of larger droplets found in the spray greater influence upon the calculated mean diameters, thus creating the increase from AMD to SMD.

Measurements of AMD at M=0.35 display the same trends as those seen at M=0.2. Figure A.5 and A.6 show that the AMDs at M=0.35 follow the same linear trend seen in Fig. 13, but at lower values. Again, at Z=10 and 50mm the distribution is not linear. At M=0.2 the droplet diameters varied from about 21 to 37 microns at Z=10mm and 16 to 41 microns at Z=50mm; the droplet diameters at M=0.35 vary from only 12 to 24 microns at Z=10mm and 9 to 22 microns at Z=50mm. Therefore, smaller droplets are created at M=0.35. This fact indicates that the shear breakup mechanism which creates smaller droplets becomes more dominant as Mach number increases. At M=0.35 smaller droplets can still be seen in the center-line region of the spray and larger droplets on the periphery of the spray.

Figure A.7(a-e) shows the SMD distribution of droplets at M=0.35. As was seen at M=0.2, the SMDs follow similar trends to that of the AMDs, but at higher values. However, measurements at Z=10, 20, and 30 mm show large fluctuations, or spikes, in SMD. At Z=40 and 50mm these spikes are still seen, but they are not as large. These spikes can most likely be attributed to the fact that at M=0.35, unlike at M=0.2, a small amount of very large droplets (~100 microns) are formed from the breakup of the jet column. This formation of very large droplets can be seen at M=0.35 because the jet column may move into the breakup regime much more rapidly than at M=0.2. It is in this breakup regime that larger droplets are allowed to form. The larger droplets account for the "spikes" seen in Fig. 19. Overall, the droplet SMDs increase away from the wall, but this increase is not as linear as that seen at M=0.2.

Z-velocities

Figure A.8 displays the Z average velocity components and Z RMS velocity components of the droplets at Z=30mm and M=0.2. These measurements will be used as a basis for further analysis at all Z locations. It can be seen in Figure A.8a that the average Z velocities of the

droplets are highest on the periphery of the spray and are lowest in the core of the spray. At Z=30mm, the spray velocities on the periphery have increased up to almost 90% of the incoming air flow velocity of 93.5 m/s. Meanwhile, within the core the velocities are only about 67% of the incoming air flow velocity.

Figure A.8b shows the Z RMS velocities of the droplets at Z=30mm and M=0.2. It is interesting to note that at ±2mm the Z RMS values are the highest. Z RMS velocities dip toward the core of the spray and decrease past ±2mm from the center of the spray. This region of higher RMS velocities at ±2mm is approximately 11% higher than the RMS at the core. The deviation can possibly be attributed to a vortex flow that exists on the edge of the jet column. In this case, it is likely that the column acts as a virtual cylinder within the flow and a vortex flow is created as the incoming air flow passes around this cylinder.

Plots of droplet Z velocities at M=0.2 can be seen in Figure A.9 and A.10. In Figure A.9(a-e), it can be seen that the Z velocities are non-uniform at Z=10mm do not become uniform throughout the spray even up to 50 mm downstream of the injection orifice. Figure A.10(a-e) presents a view along the y-axis of the Z velocities in the X-Y plane. The Z velocity of droplets within the core is only about 40% of the incoming airflow velocity at Z=10mm. By Z=50mm, the Z velocity of the spray within the core has increased to nearly 80% of the incoming airflow velocity. Figure A.11 (a-e) shows that the Z RMS velocities are also highest within the core of the spray at ±2mm. This variation Z RMS velocity creates a "hat" structure (labeled in Figure A.12a). The Z RMS values at the peaks of the "hat" are the maximum with values of around 10%. It can also be seen that as Z location moves downstream of the orifice the Z RMS velocities decrease within the core, but increase slightly on the periphery as the jet column dissipates.

At M=0.35, the Z velocities show a greater magnitude drop within the core (Figure A.12) of the spray than that displayed by the spray at M=0.2. At Z=10mm the velocity at the core is approximately 38% of the incoming air flow velocity of 165 m/s. At Z=50mm the velocity at the core has reached almost 79% of the incoming airflow velocity. These ratios are nearly the same

as those seen at M=0.2. As seen at M=0.2, at M=0.35 the Z velocities at the core are lowest and the velocities on the periphery are highest. Figure A.13 illustrates this behavior with a view of flow in the Y-Z plane. It can be seen in Figure A.14 that the Z RMS velocities behave similarly at M=0.35 and M=0.2, but the increase in Z RMS velocity at the outer edge of the core (±2mm) is much steeper at M=0.35. This steeper increase leads to a more defined "hat" structure at M=0.35 when compared to M=0.2.

X-velocities

Figure A.15 will be used as a reference for the analysis of the X velocity components of the droplets; it represents the X velocities at Z=30mm and M=0.2. In Figure A.15a, it can be seen that the average velocities increase in a linear fashion away from the wall. Labeled in the figure, a slight rise in the velocities is seen at the center of the spray. These higher X velocities at the center are attributed to the higher momentum carried into the cross-flow at the onset of fluid injection. This is the densest region of the spray. It is interesting to see that close to the wall, the average X velocities measured were actually negative. This denotes a region of swirling where the spray actually curves back in on itself close to the boundary layer. Once again, the highest X RMS values are found at the core of the spray as can be seen in Figure A.2b. However, in the case of X velocities no "hat" structure is apparent. The rise in X velocities at the center of the spray is more evident within the 3-D plots.

It can be seen in Figure A.16 (a-e) that the X velocity components of the droplets at M=0.2 are highest at the periphery of the spray as was seen in Figure A.2a. The rise in velocities seen at the center of the spray for Z=30mm is also evident at all locations in Figure A.16. The rise is most pronounced at Z=10 and becomes less evident up to Z=50mm. This could possibly be due to the dissipation of the jet column and decrease of momentum in the X direction as the droplets change direction with the downstream flow. The trend of a linear increase in X velocity can best be seen in Figure A.17 which displays the X velocity distribution along the x-axis. Again, the X velocity of the droplets increases in a nearly linear fashion as X distance from the

wall is increased. Figure A.18 (a-e) displays the 3-D plot of X RMS velocities. These graphs show that X RMS is much higher at the core of the spray, forming a "hill" structure.

The X velocity components of the droplets at M=0.35 display a distribution similar to that at M=0.2, but the velocities at each point are higher than those at M=0.2. Refer to Figure A.19 and A.20 to see that, at M=0.35, the X velocity component of the droplets also increases almost linearly as the X location moves away from the wall. The core of the spray once again displays higher X velocities and the largest X velocities can be found at the periphery of the spray. The same negative X velocities are seen near the wall. Figure A.21 (a-e) shows that the X RMS velocities are also much higher at the core of the spray and decrease toward the periphery of the spray. The values of the X RMS at M=0.35 in the core of the spray are predictably higher than those found at M=0.2. At Z=10mm for M=0.2 the X RMS is at about 4% while for M=0.35 it is at about 10%. This difference could possibly be connected to the appearance of larger droplets at M=0.35. The X RMS distribution at M=0.35 becomes more uniform than the spray in M=0.2 cross-flow by the time they reach Z=50mm where for M=0.2 the X RMS at the core of the spray is about 50% higher than that at the periphery and for M=0.35 the X RMS at the core is only about 20% higher at the core.

Y-velocities

The velocity of the droplets in the Y direction at M=0.2 at Z=30mm are presented in Figure A.22 (a-b). These plots will serve as a benchmark for further discussion of the Y velocities at all Z locations. At first glance it appears that the Y-velocities become negative past the centerline, this is not the case. Droplets traveling away from the centerline toward the right are moving in the pre-designated negative Y direction and, therefore, their velocities are measured as negative. An interesting phenomenon is seen in these measurements. Small negative values of Y velocity are seen close to the center of the spray in Figure A.22a. This lends further evidence to the presence of a vortex flow within the center of the spray (±2mm) due to the liquid jet column itself. Though, overall the Y velocities are symmetric and they reduce as

the Z location moves downstream of the injector. The Y velocities decrease toward the center of the spray and are highest on the periphery. Figure A.22b shows that the Y RMS velocity component of the droplets is highest at the core of the spray and lowest on the periphery.

Figure A.23 (a-e) shows the average Y velocity measurements for the droplets in a 3-D distribution. It can be easily seen that the Y velocities are highest at the periphery of the spray. The drops of the Y velocities into the negative region have been labeled as "dips" in Figure A.24 which shows the Y velocity distributions along the Y axis. With this in mind, the velocities are, again, seen to be uniform. Figure A.25 (a-e) shows the Y RMS velocities at M=0.2. It is seen that Y RMS velocities follow a similar trend to that of X RMS velocities with a "hill" structure at the core of the spray. However, the Y RMS variation at the core shows a greater range when compared to the X RMS velocities. Y RMS values reach up to almost 10% while X RMS values only reach approximately 5%. Also, there exists a "valley" structure in the Y RMS velocities measured at Z=10mm as seen in Figure A.25a. This "valley" structure is not seen for any other measured Z values and could possibly be due to the orientation of the vortex flow at this Z location. It is most likely not evident farther downstream due to the increased breakup of the column the Z location moves downstream of the injection orifice. Figure A.26 shows a view along the y-axis of the Y RMS velocities. These plots show that the Y RMS at the core of the spray reaches to almost 10% while it is only around 3% at the periphery at Z=10mm. By Z=50mm, the core's Y RMS has diminished to about 6%, but has remained constant at the periphery.

The average Y velocities at M=0.35 are seen in Figure A.27. These plots show the same uniform distribution of Y-velocities. In Figure A.28, the same negative values of Y velocity, or "dips," are seen at ±2mm from the center-line where a vortex flow exists. At M=0.35, these "dips" due to vortex flow are seen to dissipate more rapidly then at M=0.2. It can be seen in Figure A.28 that the average Y velocity distribution is smoother for M=0.35 at Z=50mm than that for M=0.2 at Z=50mm (Figure A.24e). In Figures A.29 and A.30 the same Y RMS patterns are seen at M=0.35 as M=0.2 only at predictably higher values.

CHAPTER 3

WEBER NUMBER DEPENDENCE

Operating Conditions

For this segment of this research, the operating conditions were varied to obtain different Weber numbers ranging from 33 to 2020. The experiment was run at an elevated pressure of 4 ata (0.405 Mpa) and temperature of 555K. The liquid to air momentum ratio was maintained constant at 40 by varying the fuel flow rate. Table 3.1 shows that the velocity of the incoming air flow was varied from 22.95 to 190.64 m/s (Ma 0.05 to 0.4) and the fuel flow rate was varied from 0.78 to 6.48 g/s to obtain the previously mentioned We.

Table 3.1 Air and fuel characteristics for different Weber numbers

We	V_{air} (m/s)	$V_{f\,(m/s)}$	$\dot{m}_f$ (g/s)	T_f (K)
33	22.95	8.4	0.78	378
133	49.25	17.5	1.62	364
285	71.01	27.2	2.51	350
520	94.84	35.4	3.27	343
800	118.5	44.1	4.08	337
1140	142.28	52.1	4.81	333
1535	164.98	60.6	5.6	330
2020	190.64	70.1	6.48	326

Weber Number Effects Results

Figures 3.1(a) and 3.1(b) show the arithmetic mean diameters and Sauter Mean Diameters (SMD) along the centerline of the spray at various values of Weber number. It is seen that at values of We greater than about 800, droplets formed have a mean diameter value of about 15-35 microns. Bigger droplets are observed at the periphery of the spray. For We = 33, the arithmetic mean diameter (AMD) at the periphery of the spray is over 90 microns (SMD>140μm). It is seen that the larger droplets found at lower We penetrate further away from

the orifice plate. However, it is also seen that in the region of the spray close to the orifice plate, the droplets formed are much smaller. This indicates that the mechanism of formation of droplets in that region is shear breakup as is commonly seen in the case of higher Weber numbers. This evidence indicates that the spray is possibly formed by multi-mode breakup at lower We numbers (We=33).

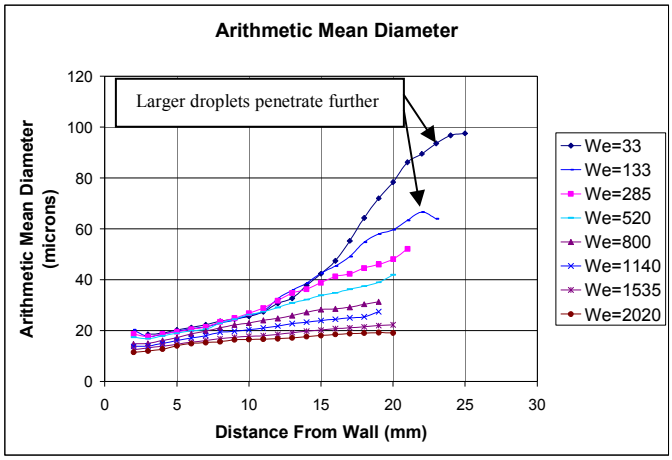

(a)

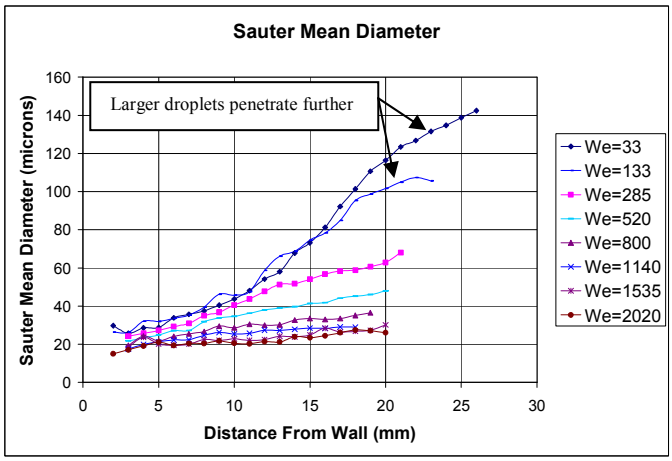

(b)

Figure 3.1: (a) AMD for different Weber numbers
(b) SMD for different Weber numbers

To further investigate the matter of multi-mode breakup at low We (We=33), diameter counts were taken 16mm from the orifice plate along the centerline in the periphery of the spray. Figure 3.2(a-d) displays histograms of the droplet diameter distribution at different Weber numbers. It is seen in the diameter histogram of Figure 3.2(a), for We=33, that two "peaks" are formed by the diameter distribution. The first peak occurs around 30 microns and the second peak occurs near 100 microns. This more clearly indicates that multi-mode column breakup occurs at We=33. For higher values of We, (Figures 3.2(b), (c) and (d)) the mean droplet diameter reduces gradually indicating that, at some point higher than We=33 and lower than We=133, multi-mode breakup no longer occurs. As the Weber number increases (Figure 3.2(a-c)), the droplet diameter distribution is seen to become more narrow, therefore, it is more uniform throughout the spray which once again indicates that shear break up dominates in this region.

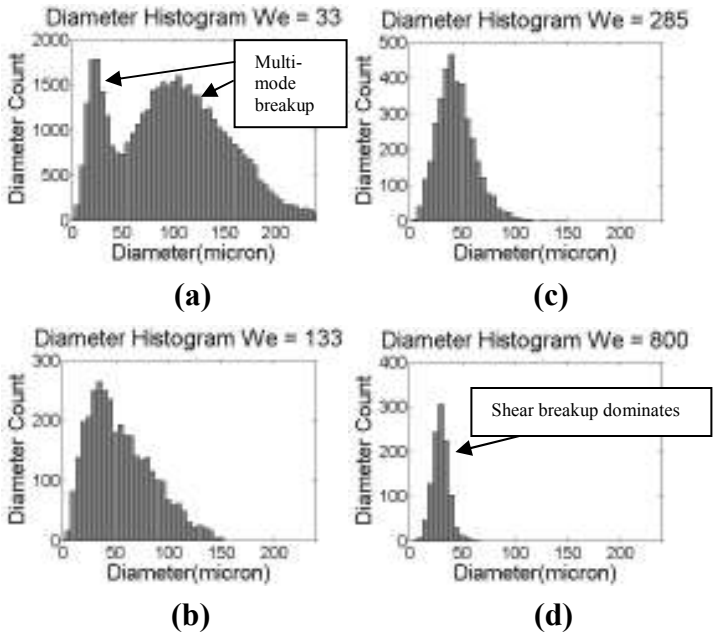

Figure 3.2: Diameter Histograms at various values of We number at 16mm from injection wall
(a) We=33 (b) We=133 (c) We=285 (d) We=800

After analyzing the effect of We upon diameter, its effect upon the droplet average Z-velocities was investigated. Figure 3.3(a) shows the mean Z-velocity components of droplet velocities for various We numbers measured on the centerline of the spray (Y=0) in the plane 30mm downstream of the injection orifice. The droplet velocities at high We numbers seem to have significant lag with respect to the velocity of incoming air flow, especially in the core of the spray located 7-8mm from the orifice plate. The absolute value of the velocity lag seems to be proportional to We number varying from 13 to 60 m/s at We=133 and We=2020 respectively. Figure 3.3(b) provides better insight on the data presented in Figure 3.3(a). It compares the Z-velocity components of droplets measured at different We numbers normalized by the corresponding incoming air flow velocity which changes with We. It is observed that in the core of the spray (2-7mm from the orifice plate) droplets have the same normalized velocity lag of 20-30% for the entire investigated range of We numbers with an exception at We=33, which displays only 0% to 10% velocity lag 2mm to 12mm from the orifice plate, respectively. It is worth noting that on the periphery of the spray (8-25mm from the orifice plate) the normalized velocity lag is negatively proportional to the We number within the range of We=133-2020. Thus, at a distance of 14mm from the orifice plate, droplet velocities attain 90% of the incoming air flow velocity at We=2020 while at We=133 only 76%. This trend most likely corresponds to the significant difference in droplet sizes, 20μm to 40μm for We=2020 and 133 respectively. It should also be noted that We=33 is the only exception from this trend, which may reflect the fact that a completely different mechanism of jet disintegration exists at We=33 (multi-mode instead of shear break-up).

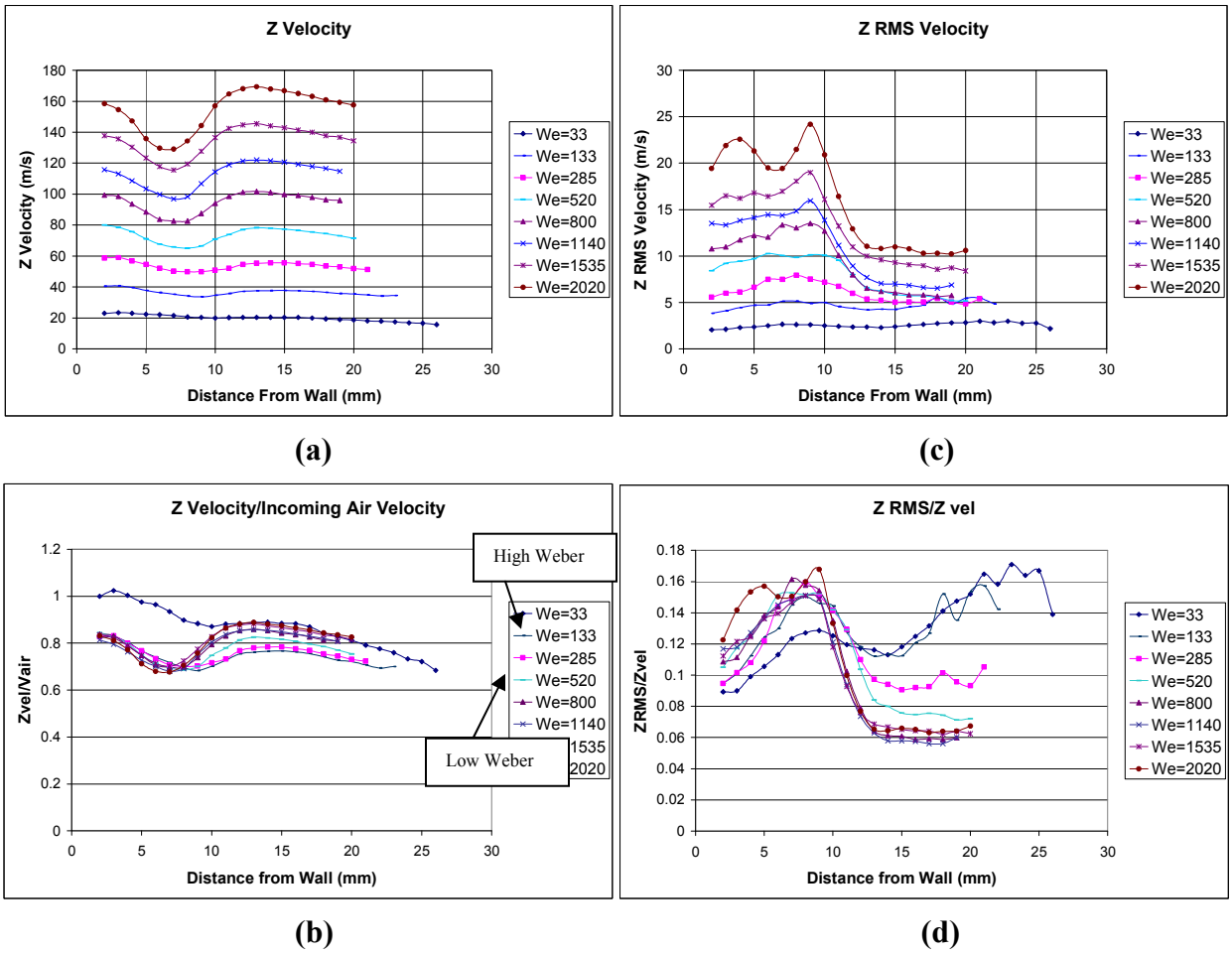

Figure 3.3: Z velocity components and ratios at different Weber numbers (a) Average Z velocity of droplets (b) Z velocity normalized by velocity of incoming air (c) Z RMS velocity of droplets (d) Z RMS normalized by average Z velocity of droplets

The RMS values of the Z-velocity components of droplets are plotted in Figure 3.3(c). As expected, higher RMS values were observed at higher We numbers. At We=2020, two maximum RMS values of 22.5m/s and 24.5 m/s were observed within the core of the spray at distances of 4.5mm and 8mm from the orifice plate respectively. In the range We=133-1535, only one RMS maximum in the core was typically observed. For better comparison, the Z-RMS data are presented in Figure 3.3(d) as values normalized by the average droplet Z velocities. Normalized Z-RMS profiles reveal similar behavior in the range We=285-2020, especially in the

core region. Normalized RMS values vary from 10-12% near the orifice plate to 15-17% at a distance of 7-8mm from the plate. RMS values of these sprays on the periphery (12-20mm from the plate) are significantly lower – 5.5%-10%. In general, higher values of normalized RMS on the periphery correspond to lower We numbers (10% for We=285 and 5.5% for We=1140) which probably reflects the wider distribution of droplet sizes at these We. Again, analysis of the Z-RMS profiles plotted in Figure 3.3(d) reveal a different trend for sprays measured at We=33 and We=133. At We=133, the ratio seems to depend upon location as it mirrors the behavior shown by higher We values within the core of the spray, but then follows the We=33 profile in the periphery of the spray.

Figure 3.4(a) shows the average X-velocity components of droplets at different We numbers. The X-velocity is higher at the periphery of the spray. X-velocity values were found to be proportional to the initial velocity of the jet injected from the orifice for the entire range of measured We numbers (We=33-2020). It is seen that droplet velocities in the X direction typically attain 45% of the calculated velocity of the jet (see Figure 3.4(b)) on the outer border of the spray (~18-23 mm from the orifice plate) except spray with We=33 obtains a maximum velocity of droplets that is 65% of the jet velocity at a distance of ~26mm from the plate. The average X-velocity of droplets near the orifice plate is negative (towards the plate). Higher absolute values were observed at higher We numbers (~ -4m/s at We=2020 and ~-0.5m/s at We=33 – see Figure 3.4(a)). Both trends in X-velocity variation with We number (higher velocities at lower We numbers on the outer border of the spray and more negative X-velocities near the orifice plate at higher We numbers) can possibly be attributed to the droplet size dependence upon We number seen previously. Bigger droplets which penetrate further from the orifice plate have a higher X-velocity. Smaller droplets more closely follow the vortex flow and

are found to even move in the negative direction towards the plate downstream of the injection orifice.

In spite of the strong variation of X-velocity profiles seen in Figure 3.4(a), the inclination of velocity vector calculated as $\theta=arctan(Vx/Vz)$ is not found to strongly depend upon We number (see Figure 3.4(c)). Typically, inclination of ~10-13^0 from the direction of air flow was observed on the outer border of the spray (lower values correspond to higher We numbers). Maximum inclination of ~19^0 on the distance 26 mm from the plate was measured for We=33.

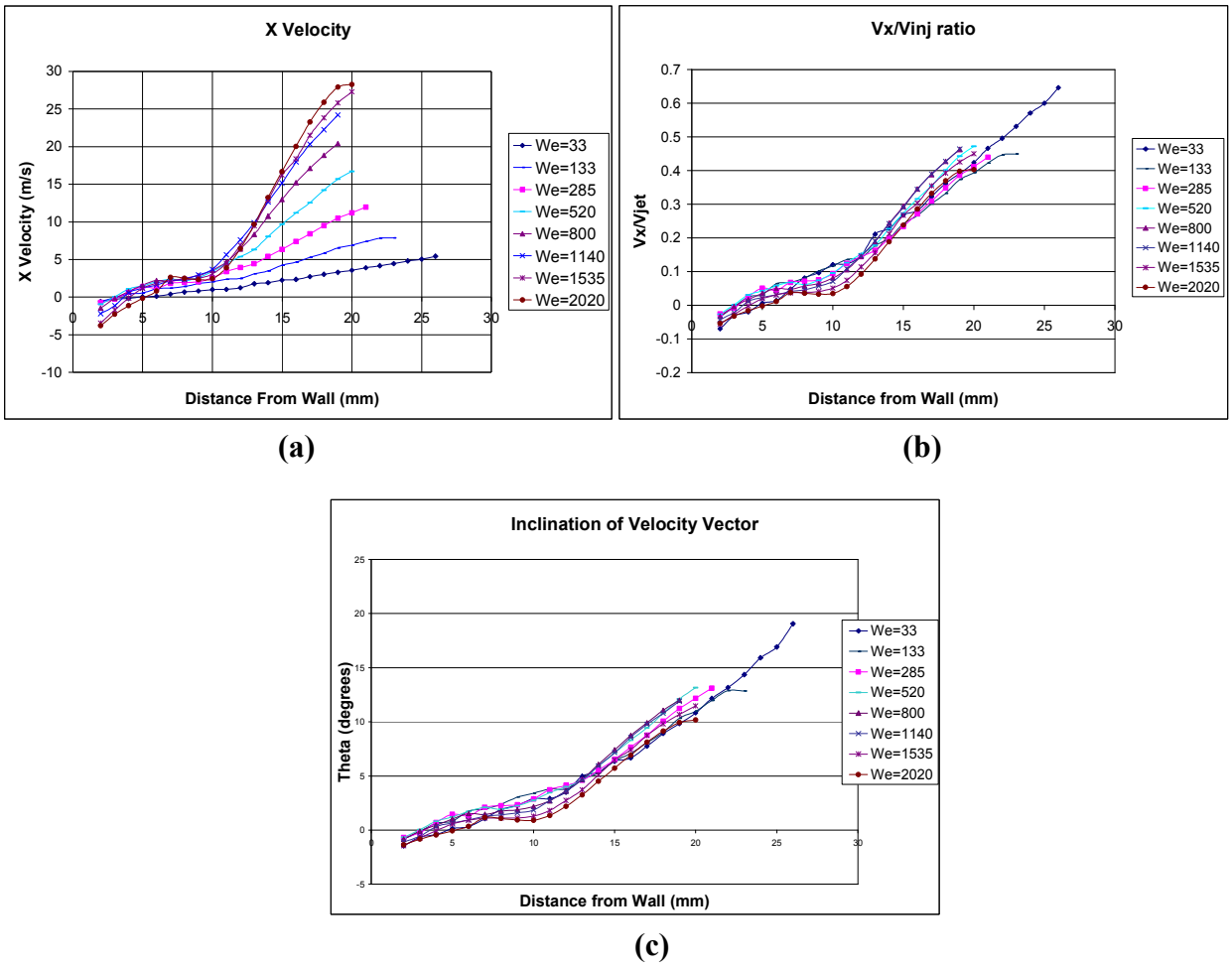

Figure 3.4: X velocity components at different Weber numbers (a) Average X velocity of droplets (b) Average X velocity normalized by velocity of injected fuel (c) Inclination of velocity vector

RMS values of droplet X-velocity are seen to change as We is changed (see Figure 3.5(a)). Their maximum values observed in the core of the spray vary from ~1.5 to 12m/s at We=33 and We=2020 respectively. Lower RMS values (1m/s to 6 m/s) were observed on the periphery of the spray for the same range of We numbers. Comparison of X-RMS to average X-velocities for the sprays characterized at different We numbers is presented in Figure 3.5(b)[1] which reveals high normalized values of X-RMS from 220% to 450% in the core of the spray (higher values correspond to higher We numbers). At the periphery of the spray relatively low values of 20-50% were observed.

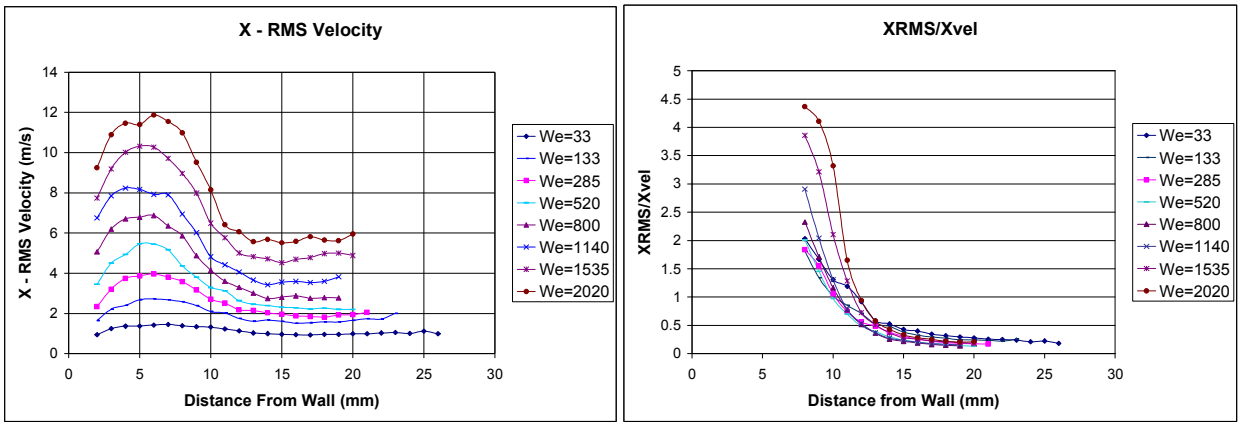

(a) **(b)**

Figure 3.5: X RMS velocities at different Weber numbers (a) X RMS velocity of droplets (b) XRMS normalized by average X velocity of droplets

[1] Figure 9(b) represents the values beyond about 7mm from the wall, where a noticeable trend arises. Zero X-velocity zone near the wall creates a very wide range ($X_{RMS}/X_{AV.}$ =40-100) with no apparent trend.

CHAPTER 4

INJECTOR DESIGN DEPENDENCE

Operating Conditions

This segment describes an investigation of the dependence fuel spray characteristics have upon injector design. All tests were run using both injector #1 (sharp) and injector #2 (smooth) at the previously mentioned temperature and pressure of 555K and 5 atm. The fuel flow rate and incoming air velocity were varied to achieve the 3 different Weber numbers and momentum flux ratios of 500, 1000, and 1500 and 10, 20, and 40, respectively. Table 4.1 summarizes the test conditions for each combination of We and q. Only one operating condition was chosen for analysis to limit the scope of this segment. After studying the results for each condition, it was found that the condition where We=1000 and q=20 is a good representation of the results found for the eight other operating conditions. So, all analysis of spray characteristics has been completed for this condition.

Table 4.1: Experimental Conditions for Imaging and Spray Characterization of Different Injectors

Momentum ratio (q)	10	20	40	10	20	40	10	20	40
Weber number (We)	500			1000			1500		
Mach #	.167			.237			.292		
Air Velocity (m/s)	78.1			112			138.3		
Fuel Mass Flow Rate (g/s)	2.05	2.93	4.10	2.93	4.07	5.85	3.55	5.10	7.16
Fuel temp (C)	55	55	48	58	56	49	61	57	54

The fuel injectors were fixed on the centerline of the plate 10mm downstream of the supply channel termination. Injector #1 (Figure 4.1(a)) employed a sharp-edged design with L/D~10 and a nozzle flow coefficient of 0.73. Injector #2 (Figure 4.1(b)) was constructed using

a countersink design and has a ratio of L/D~1. The injectors were tested at atmospheric conditions with We=0 prior to introducing jet engine conditions in order to verify the near elimination of injector-induced turbulence using Injector #2.

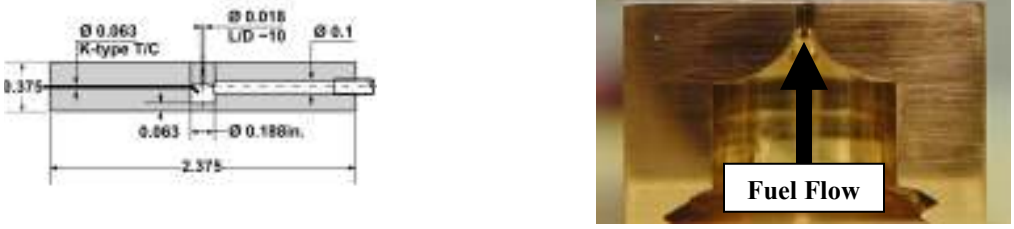

(a) **(b)**

Figure 4.1: Injector profiles (a) Injector #1 and (b) #2

Injector Design Effects Results

This discussion is organized into three sections. First, the images of the spray are analyzed for properties of the jet without the crossflow using each injector type. Then the trajectories of the jet at We = 500 and momentum ratio of 40 are plotted using the spray images and compared with the trajectories found using a volume flux threshold and data found using PDPA. Finally, the PDPA data taken along the centerline of the spray using injectors #1 and #2 are plotted and compared. The volume flux of the spray obtained from PDPA data is used to characterize the core of the spray. The arithmetic mean and Sauter Mean (SMD) diameters for the two injectors are compared. The average Z and X velocities of the droplets within the spray were also found along with the Root-mean-squared (RMS) velocities in the same directions. From this analysis, a better understanding of how injector design affects spray characteristics is obtained.

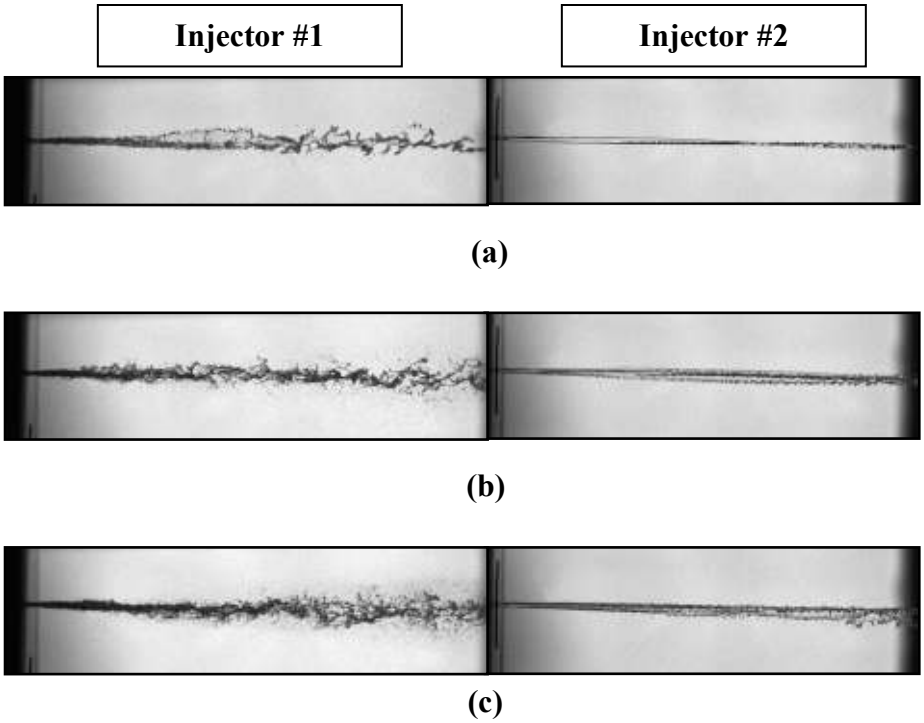

Figure 4.2: Injector evaluation at We=0
(a) mf=3g/s, Re=7033 (b) mf=5g/s, Re=11742 (c) mf=7g/s, Re=16421

Figure 4.2 shows the images of the spray in the absence of crossflow for the two injectors at different fuel injection Reynolds number. It is seen that the jet from injector #1 disintegrates due to the jet turbulence alone and large number of droplets are formed close to the orifice. This effect is more prominent at higher jet Reynolds number. In case of injector #2, the jet turbulence is not totally eliminated but its effect on the jet disintegration is very small. Figure 4.3 shows micro images of the spray for the case of jet Reynolds number of 11750 at different locations along the jet for both the injectors. Surface waves are formed on the edges of the jet due to the shear layer between the jet and the ambient air. These surface waves are more smooth and regular. These waves grow with increased distance from the orifice and few bigger droplets are seen to be sheared off from the surface.

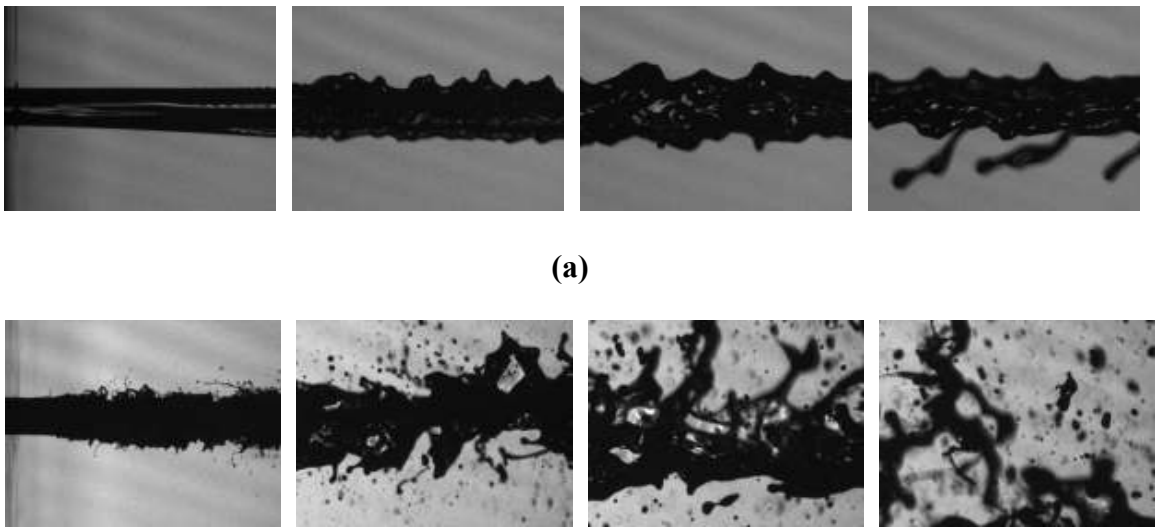

(a)

(b)

Figure 4.3: Instantaneous micro images of jet at We=0 (a) Smooth orifice (b) Sharp edged orifice

Volume Flux Measurements

The PDPA data analyzed with the Flowsizer software gives the volume flux of the liquid. PDPA measurements have been made on the centerline of the spray (Y=0) at six different location of 15 and 60 times the diameter of the injection orifice for both the injectors. Figure 4.4 shows the volume flux measurement along the centerline of the spray at Z/d locations of 15 and 60. It is seen that the volume flux follows similar trend for both the injectors with a shift to the right for injector #2 which exhibits a larger penetration. The location of the peak of the volume flux gives the location of the core of the spray.

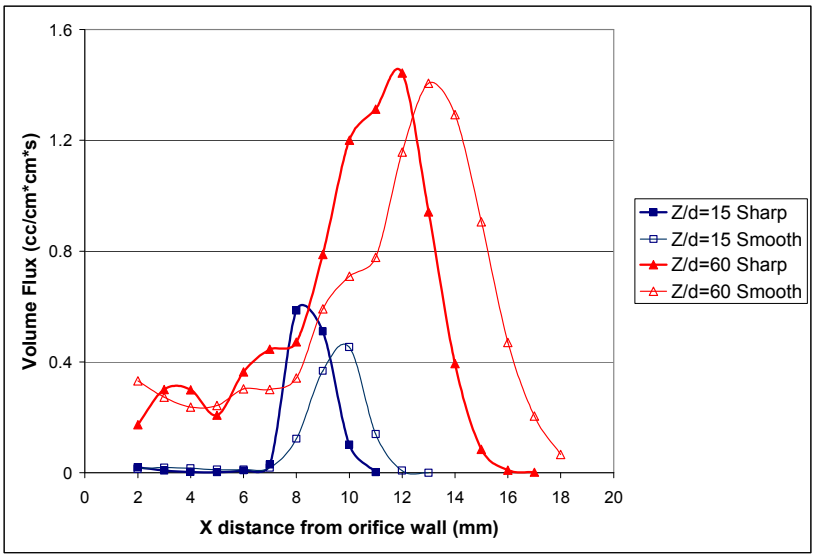

Figure 4.4: Volume Flux Comparison between injectors #1 and #2

Droplet Arithmetic Mean Diameters and Sauter Mean Diameters

Figure 4.5 shows a comparison of D10 for Injector #1 (Sharp) and Injector #2 (Smooth) at the Z/d locations of 15 and 60. It can be seen that the mean diameters follow the same trends for both injectors; however the smooth injector produces smaller droplets. The difference in droplet size is much more prominent closer to the injector orifice at Z/d=15. Using micro-imaging, it can be seen that both injectors produce liquid jet columns with surface waves which are a source of primary breakup. However, it is seen that the more turbulent column created by injector #1 also generates ligaments, or curls, of liquid which may be responsible for even larger droplets when they are sheared from the liquid column. At the location Z/d=60, since the penetration of the jet for the smooth injector is higher, if we shift the curve for the arithmetic mean diameter, it would almost overlap with the curve for injector #1. Hence we can say that eventually the same size droplets are formed but the smooth injector forms smaller droplets earlier. Thus, it is important to also consider the increased penetration of the spray using

injector #2; measurements taken at a fixed X and Y location could be documenting different stages of spray breakup. Where as, if X and Y were changed to account for this increased penetration, differences in spray characteristics may not be found.

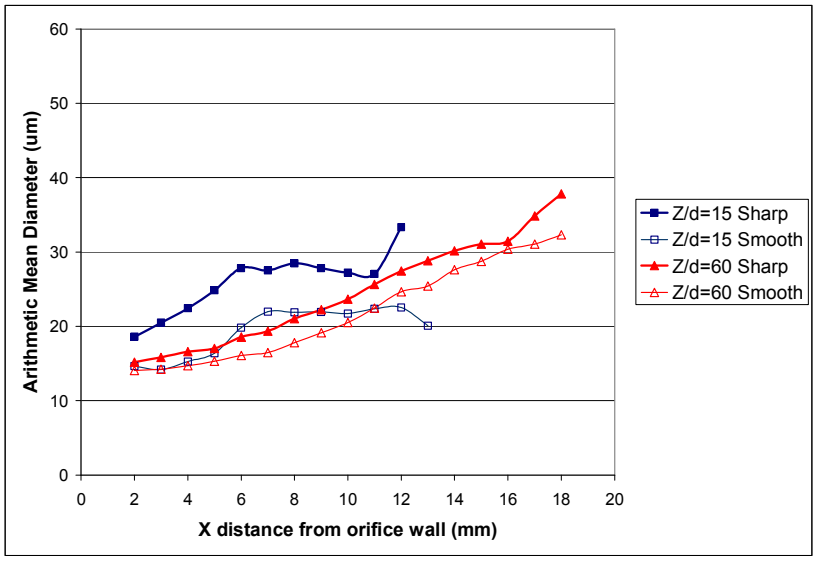

Figure 4.5: D_{10} Comparison b/w injectors #1 and #2

Figure 4.6 illustrates the comparison of SMD for the two injectors. For combustion problems where the active surface area of the spray is important, SMD is a vital parameter. It can be seen that the SMD for injector #1 and #2 follow seemingly random patterns with large fluctuations. Yet, a general trend is noticed within the central portion of the spray where the SMD for injector #2 is found to be less than that from injector #1 and less erratic. Meanwhile, at the periphery of the spray, SMD for both injectors are closer. This could possibly be due to the fact that the spray breakup for the jet emanating from injector #2 is much more uniform than that of injector #1 and smaller droplets are formed as pressure atomization is limited by the countersink design. This uniformity creates fewer fluctuations in SMD and lowers the overall value of SMD for injector #2. However, at the periphery of the spray, the difference in

uniformity is negligible and shear breakup dominates which is why the relationship between the two injectors' SMD measurements changes.

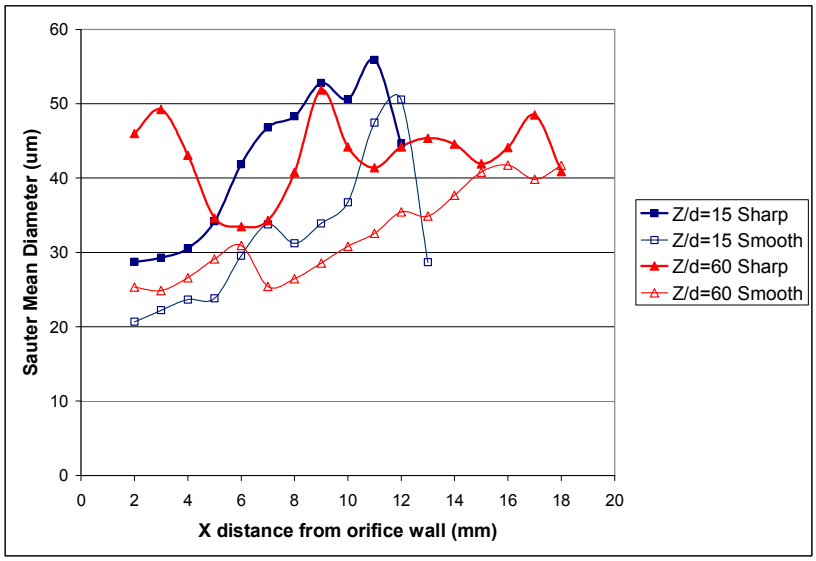

Figure 4.6: D_{32} Comparison b/w injectors #1 and #2

Droplet Mean Z-velocity and Z-RMS Velocity

The mean velocity of the droplets in the Z direction is illustrated in Figure 4.7. The difference between the velocity of the droplets created by injectors #1 and #2 can be seen at Z/d locations of 15 and 60. For each case, the general trend of higher velocities at the periphery of the spray can be seen. Moreover, it can be seen that at the periphery of the spray the mean Z-velocity of the droplets are nearly equal. At a location before the core of the spray, a velocity deviation is found. The same effect has been observed in literature[21] and is believed to be due to the shielding effect created by the core of the spray above the region of least Z velocity. As the core is broken up further downstream, at Z/d=60 it can be seen that the velocity deviation decreases greatly. Compared to injector #1, it can be seen that the deviation of the mean Z-

velocity within the core created by injector #2 is less slightly shifted. The shift is simply explained by the fact that the core of the spray is shifted the same distance as described above.

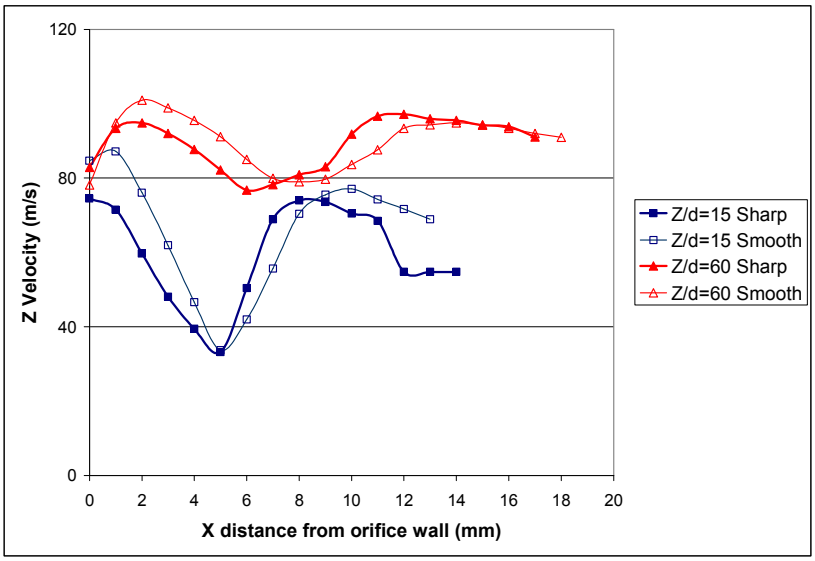

Figure 4.7: Mean Z-velocity Comparison b/w injectors #1 and #2

The RMS Z-velocity is a good indicator of the droplet velocity variation that can be found within the spray. It was seen above that injector #1 created a spray with much larger mean droplet diameters. This result was described as a result of the turbulence created by the sharp-edged design of the injector. This turbulence was seen to create a greater variation in droplet size which, in turn, can reasonably be expected to create greater variation in the RMS values of the droplet velocities. However, it can be seen in Figure 4.8 that injector #2 actually creates greater Z RMS values within the core of the spray. This could be a result of the increased solidity of the liquid jet emanating from injector #2. At the periphery, this effect is negligible and we see the RMS values of the droplet Z-velocities becoming more uniform between the two injectors. Also, as the spray moves downstream, the droplet characteristics for each injector become more similar and this variation is nearly equal, but once again shifted due to the shift in the core of the spray between the two injectors.

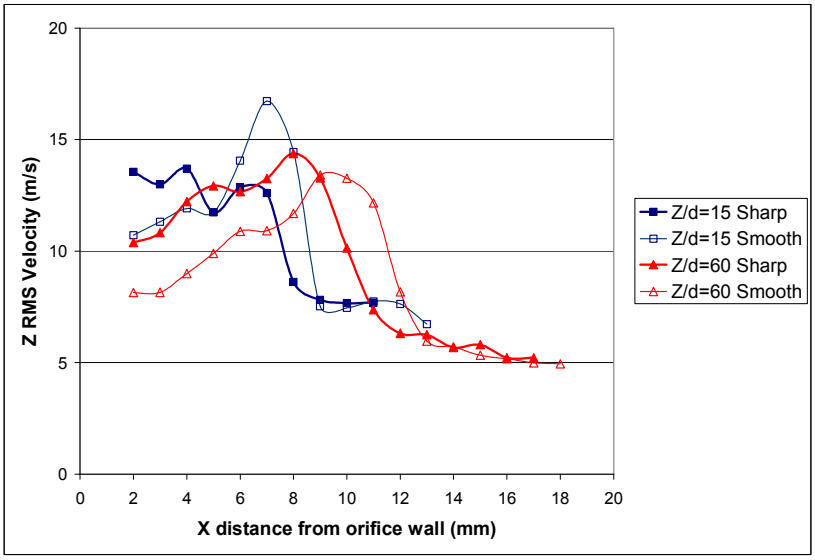

Figure 4.8: RMS Z-velocity Comparison b/w injectors #1 and #2

Droplet Mean X-Velocity and X-RMS Velocity

The mean X-velocity of the droplets has been seen to be largely dependent upon their size due to momentum transfer between the incoming air flow and droplets sheared from the injected liquid column. Larger droplets carry more liquid mass and, therefore, more momentum into the crossflow. Thus, it can reasonably be expected that we will find larger mean X-velocities for the droplets created by injector #1 due to the fact that injector #1 created larger droplets. In Figure 4.9, it can be seen that this is *not* the case for the spray close to the injector orifice wall while as measurements are plotted farther from the wall this trend does occur. Figure 4.9 illustrates the mean X-velocities of the droplets at Z/d=15 and 60 for injectors #1 and #2. This comparison reveals the phenomenon in which the mean X-velocities of the droplets along the centerline of the spray are greater for the droplets created by injector #2. This difference between the droplets of injectors #1 and #2 can be seen to occur from the point where measurements began to a location that approximately corresponds to the inner edge of the spray's core. It can

be seen that the core of injector #2 has a maximum near X=10 and 14mm for Z/d=15 and 60 respectively. The increase in volume flux as the core is approached is seen to begin at approximately X=6 and 10mm for the same Z/d locations. In Figure 4.9, it can be seen that the difference ends at approximately X=6 and 10mm. This shows that the increased solidity of the spray (decreased turbulence) liquid jet may limit the aerodynamic forces upon the droplets which lie below it. This allows the droplets to carry greater momentum into the test section near the wall. However, as the droplets move toward the core of the spray, they become just as vulnerable to aerodynamic forces, thus eliminating the difference and creating the relationship that was previously expected where the smaller droplets from injector #2 have slightly lower mean X-velocities. In effect, the solidity of the liquid column could possibly affect the characteristics of the vortex flow around the column (i.e. vortex "strength") which, in turn, affects the droplet velocities near the injection plate.

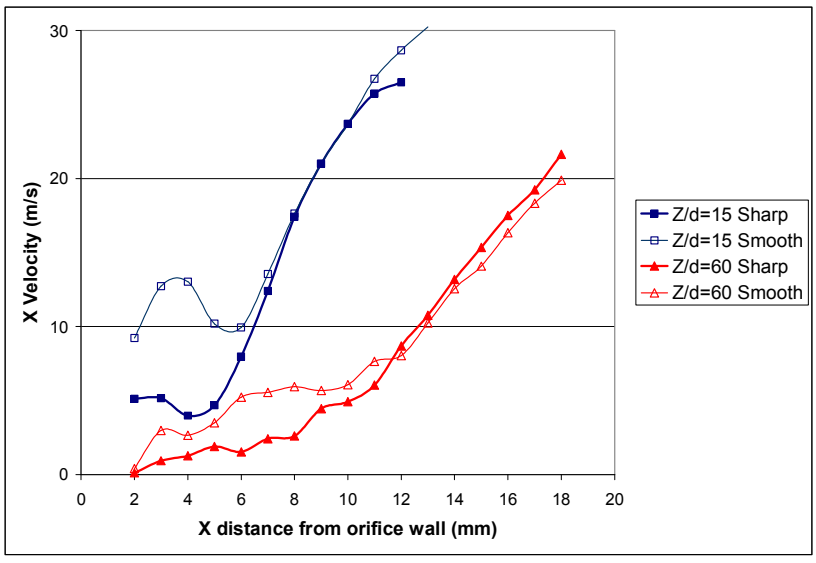

Figure 4.9: Mean X-velocity Comparison b/w injectors #1 and #2

Figure 4.10 shows the comparison of droplet RMS X-velocities between injectors #1 and #2. We see that the RMS X-velocities for the droplets created by injector #2 are also greater than those of injector #1. This relationship is the same as the one found to exist for the RMS Z-velocities and can be explained using the same reasoning. Thus, it can again be theorized that the increase in RMS values for the droplet velocities is possibly attributed to the increased solidity of the liquid jet produced by injector #2 when compared to injector #1. Moreover, it can be theorized that the liquid column emanating from injector #2 creates vortices which exhibit lower X-velocities in the X direction. Evidence of these vortices was seen to exist in the spray characteristics segment of this research as well.

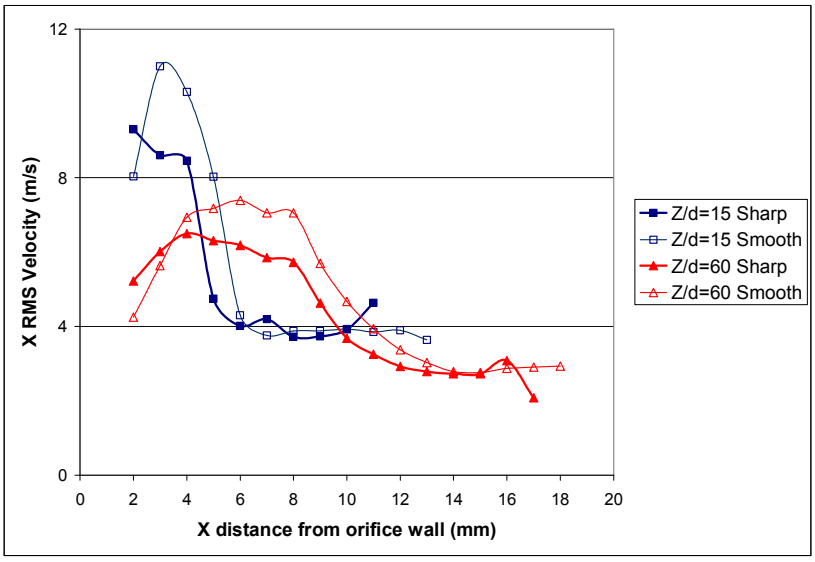

Figure 4.10: RMS X-velocity Comparison b/w injectors #1 and #2

CHAPTER 5

CONCLUDING REMARKS

The main accomplishment of this work is the data analysis covered in chapters 2 through 4. This research represents a portion of the work that can be done using the gathered data and delivers a preliminary investigation into several interesting spray design questions. Several interpretations of the collected results have been offered in order to examine the effects certain design parameters have upon spray characteristics. This section summarizes some of the key observations made in this report.

Spray Characterization

Spray created by Jet-A fuel injection into a cross flow (M=0.2 and M=0.35) of the preheated (T=555K) air was investigated. Fuel was injected from a plate containing single sharp edged orifice, 430 microns in diameter and L/D ratio of 10 and a fuel coefficient of 0.73. Pressure in the test section was maintained at 4 atm. The investigation was carried out with a fuel to air momentum ratio of 40. Laser Doppler Velocimetry (LDV) and micro-LDV were used for characterization of the incoming air flow core and the flow boundary layer conditions respectively. A Phase Doppler Particle Analyzer (PDPA) was used to obtain spray droplet diameters and velocities of the droplets in three mutually orthogonal directions (X, Y, and Z).

The design of the test rig gave uniform and stable flow of the incoming air (non-uniformity less than 1%, RMS velocity ~4% in the core of the flow). The thickness of the turbulence boundary layer near the flat plate containing injection orifice was about 3mm. A cross section of the incoming air channel 5 mm upstream of the injection orifice was chosen for characterization of the boundary conditions for the spray investigation. The influence of the

spray on the core flow of the incoming air in this cross section was found to be negligible. The effect of the spray upon the upstream boundary layer was found to be negligible beyond 7.5mm. A z/d location of about 25 was found to be suitable to begin computations for the flow conditions mentioned.

Measurements of droplet AMD and SMD show that droplet diameters become more uniform as the Z location is moved downstream of the orifice. However, it can be seen that close to the orifice the smallest diameter droplets can be found and on the periphery of the spray the largest diameter droplets are found. The droplet diameters increase in a linear fashion as the X location moves away from the wall. At M=0.35, a strong variation in droplet SMDs can be seen that is not present for M=0.2. This variation can possibly be attributed to the formation of a few very large droplets (~100 microns) within a breakup region that develops more rapidly at M=0.35. This breakup region is not seen to form for flow of M=0.2 at the 5 locations scanned downstream of the injection orifice.

At M=0.2 and M=0.35, the spray velocities display similar characteristics. The velocities were found to be lowest at the core of the spray and highest on the periphery, possibly due to larger droplets found on the periphery. At 10mm downstream of the orifice the axial velocity component of the droplets was found to be about 40% of the incoming airflow velocity. Meanwhile, at 50mm downstream, the core velocity increases to around 80% of the incoming airflow velocity. These ratios are found to hold at both M=0.2 and M=0.35. The Z RMS for each case displays a “hat” structure in its distribution. This structure could possibly be attributed to a vortex flow that might be formed around the jet column. For both M=0.2 and M=0.35, higher Z and Y velocities occur at the periphery of the spray while lower velocities are found within the center of the spray. The X velocities seem to follow the same trend except that at the

center-line region of the spray X velocities increase slightly. This may be attributed to the higher momentum in the X direction carried by the jet column along the center-line of the spray. This momentum is seen to decrease downstream of the orifice as the jet column breaks up and the X velocity components become more uniform throughout the spray. The highest RMS velocity values for all cases are found within the core of the spray.

Weber Number Dependence

Spray formed by injection of Jet A into cross flowing air was investigated at elevated pressure (4 ata) and temperature (555K, 1000R) using PDPA. The influence of the flow Weber number upon spray characteristics was investigated within a range of We between 33 and 2020 while keeping the fuel to air momentum-flux ratio constant at 40. The Shear Breakup mechanism dominates for We greater than about 300. Larger droplets (100-200 micron diameter) are observed at lower values of We (33, 133 and 285). Histograms of droplet diameter distribution were investigated to further clarify the dependence of breakup mode upon We. It was seen that for low We (We~33), a double "peak" distribution occurred. This clearly indicates the presence of multi-mode break up in this region. As We increases, the distribution of droplet diameters becomes more narrow, meaning the distribution is more uniform throughout the spray at higher We and shear breakup dominates.

The mean droplet Z-velocity components display considerable lag with respect to the incoming air flow velocity, especially within the core of the spray (7mm-8mm from the orifice plate). The absolute value of the velocity lag seems to be directly proportional to the We number as it varies from 13 to 60 m/s at We=133 and We=2020, respectively. It is seen that the velocity lag for each We number is approximately 20-30% with the exception of We=33 which display a

lag from 0-10% within the core. This is contributed to the presence of multi-mode break up of the spray within the core at low We number.

The mean X-velocity close to the orifice plate is negative in magnitude indicating the presence of vortices which are responsible for the bending of the liquid jet. The negative velocities are higher in magnitude for higher values of We. Typically, the droplets obtained about 45% of the fuel jet velocity. However, at We=33 the droplets reached a maximum of 65% of the jet velocity. These findings support the previous finding that larger droplets are attributed to low We and smaller droplets to high We. Specifically, larger droplets that penetrate further away from the orifice wall can possibly be associated with higher X-velocity while smaller droplets more closely follow the vortex flow within the core of the spray and move in the negative direction toward the orifice wall as the spray is bent by the vortex flow. In spite of variation of X-velocity profiles due to We number, it was seen that the inclination of the velocity vector, typically ~10-13°, does not strongly depend upon We number.

Injector Design Dependence

Spray created by two injector designs, one with a straight orifice with L/d ratio of 10 and the other with a smooth transition and approximately unity L/d ratio were investigated using PDPA and imaging techniques. Spray images in the absence of crossflow showed the formation of droplets due to the combined action of liquid jet turbulence and aerodynamic shear forces from the ambient air for the case of the sharp edged injector. In the case of the smooth injector, surface waves were observed but no significant droplet formation was seen.

It was seen that the smooth injector produced greater penetration of the jet into the crossflowing air. With the turbulent layer disintegrating into ligaments, the sharp orifice

exhibited larger droplets close to the orifice. It was seen that injector design may have an effect upon droplets' X-velocities. This could possibly be due to the variation of vortex flow characteristics caused by the varying uniformity of the liquid column using each injector. Meanwhile, other spray characteristics like the final droplet size distribution and velocity in the direction of air flow were found to be the same for both the injectors under consideration.

Future Work

More work is required concerning this subject. From this data, a new set of spray penetration correlations could be obtained and should be compared to the findings of others such as Wu et al. This research only details a small cross section of the data gathered during research and further work can be done merely processing this data in order to compare results at different combinations of Weber number and momentum-flux ratio. Moreover, in this study's analysis of the influence Weber number has upon spray characteristics, one could argue that the effects we see could be more accurately described as velocity effects. Further research could be done to discover whether these effects are truly due to Weber number changes or if they are merely a result of incoming air flow velocity changes.

An important characteristic in this study which is not discussed is breakup length or the point at which the liquid column ceases to exist and is completely atomized. Some studies have been done concerning this, but without crossflow. It would be of great interest to design an experiment which could investigate this characteristic so that a set of correlations for the breakup length could also be found. Further work could also be conducted in relation to injector design dependence of the liquid jet in crossflow and how spray characteristics change with more, different injector designs.

APPENDIX A

SPRAY CHARACTERIZATION FIGURES

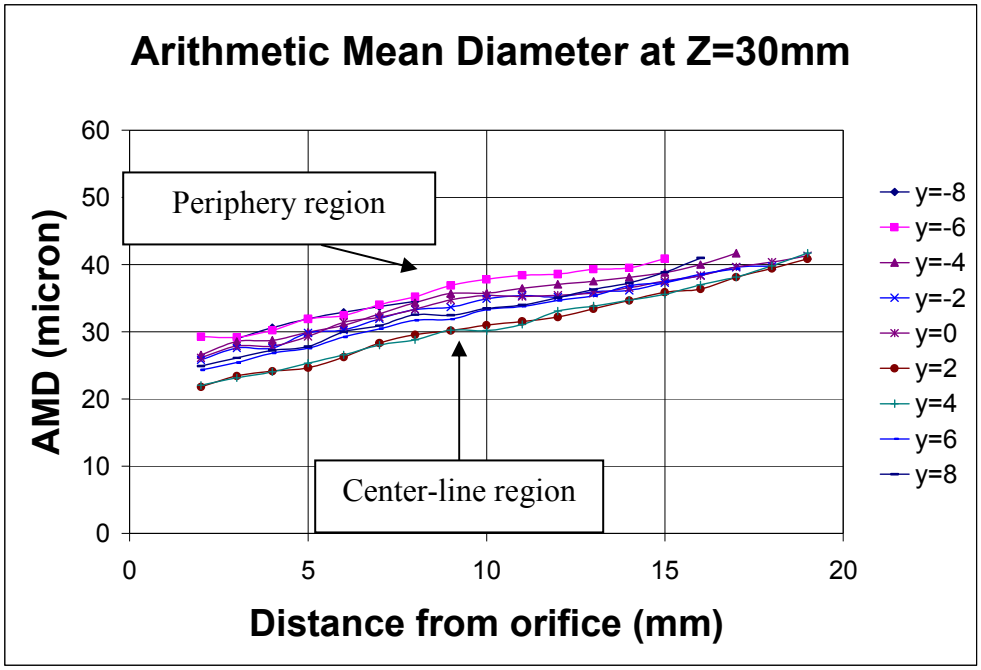

(a)

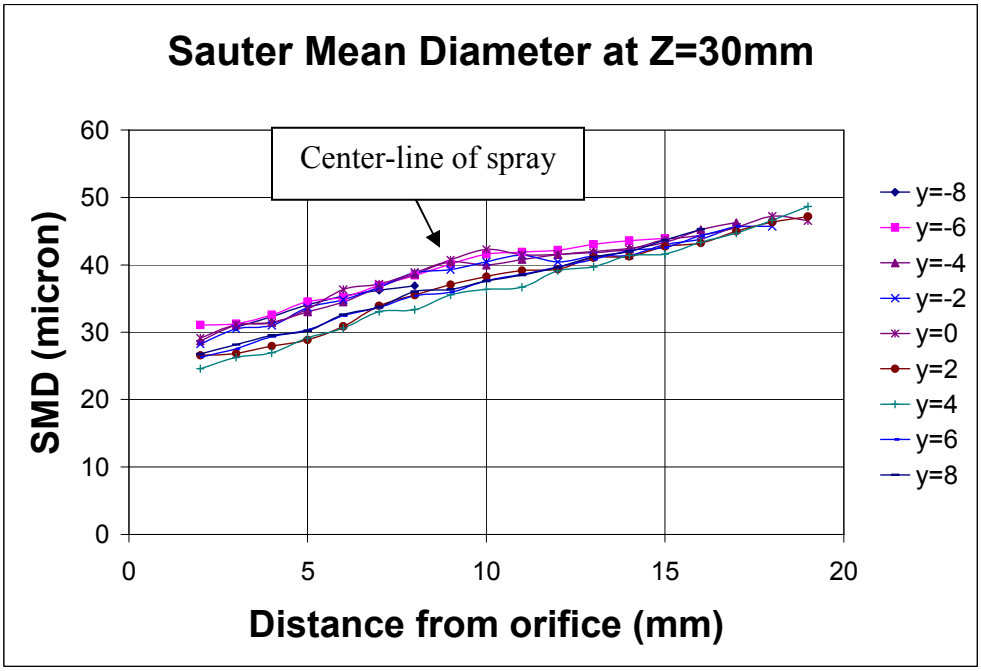

(b)

Figure A.1: Mean Diameters in the plane of Z=30mm at M=0.2
(a) Arithmetic Mean, D_{10} (b) Sauter Mean, D_{32}

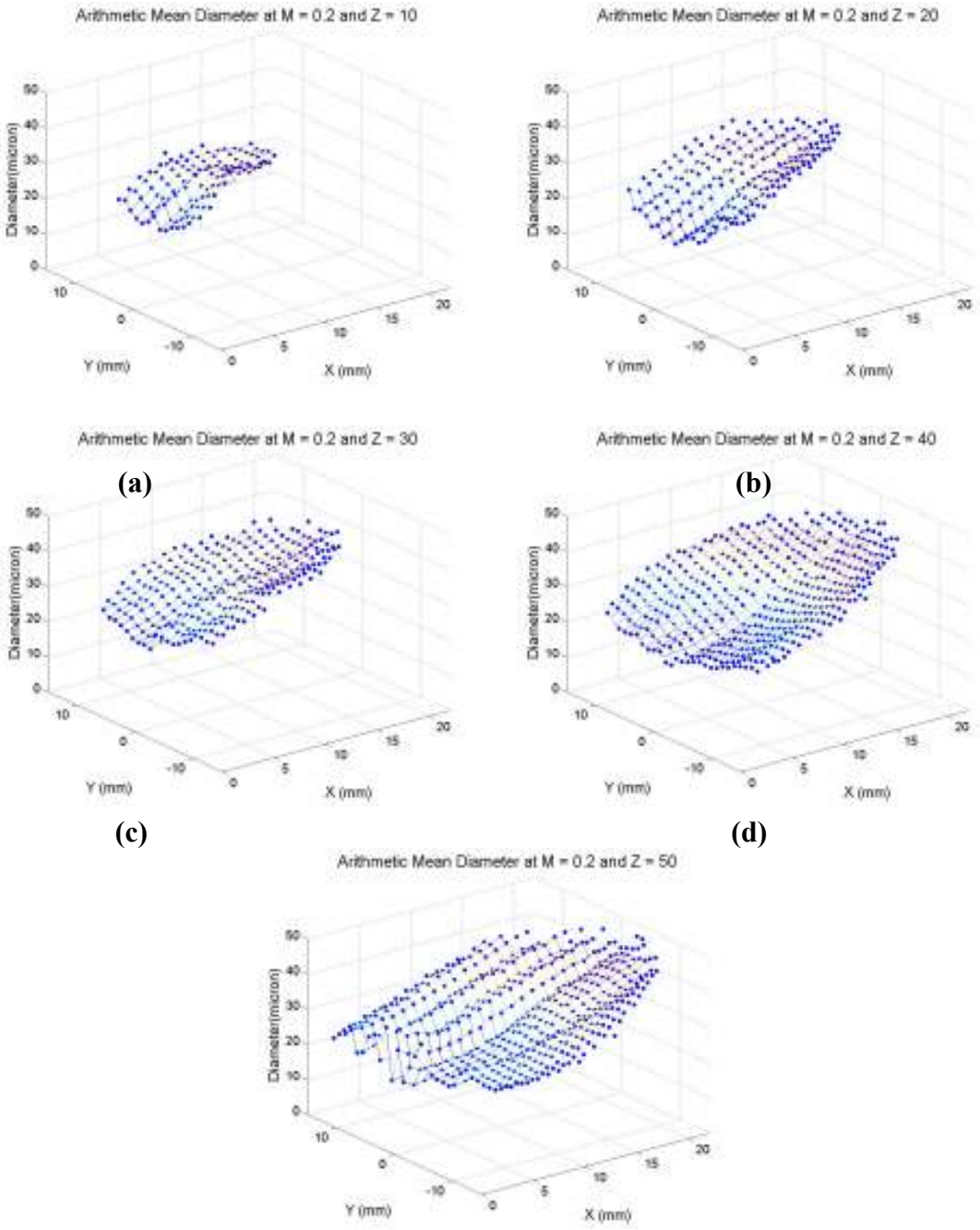

Figure A.2: Arithmetic Mean Diameter at M=0.2 for different Z locations (a) Z=10mm (b) Z=20mm (c) Z=30mm (d) Z=40mm (e) Z=50mm

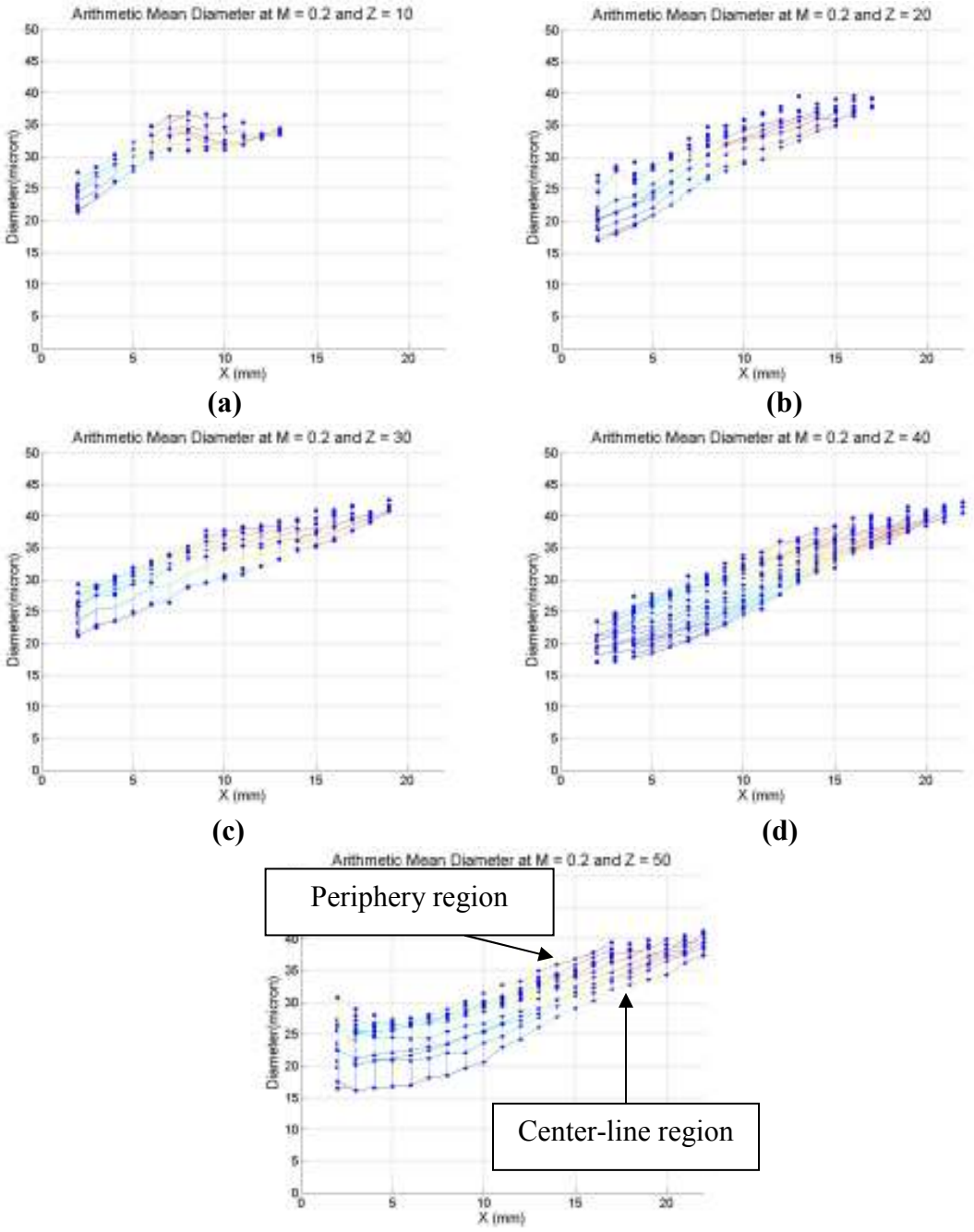

Figure A.3: Arithmetic Mean Diameter, view along x-axis at M=0.2 for different Z locations

(a) Z=10mm (b) Z=20mm (c) Z=30mm (d) Z=40mm (e) Z=50mm

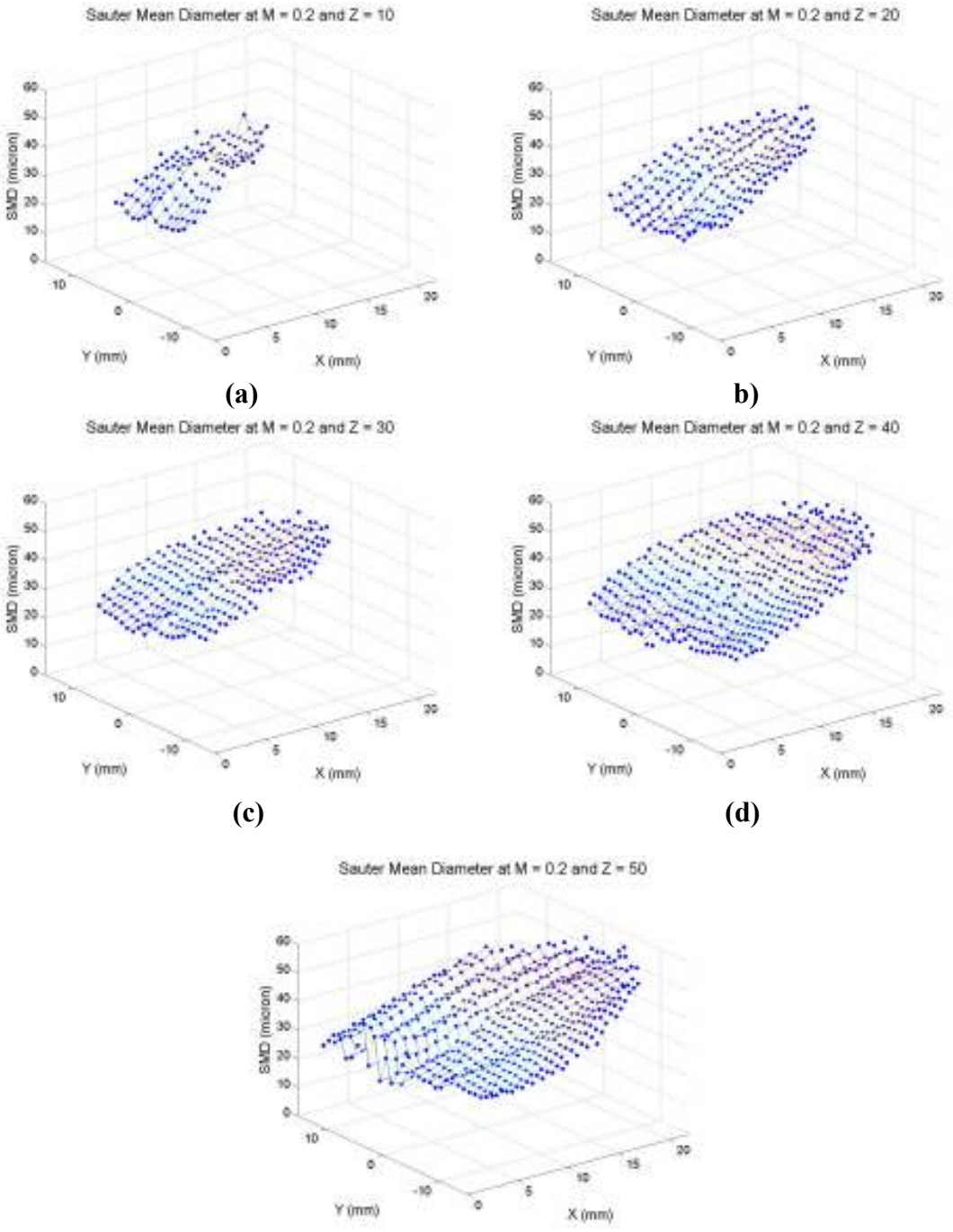

Figure A.4: Sauter Mean Diameter at M=0.2 for different Z locations
(a) Z=10mm (b) Z=20mm (c) Z=30mm (d) Z=40mm (e) Z=50mm

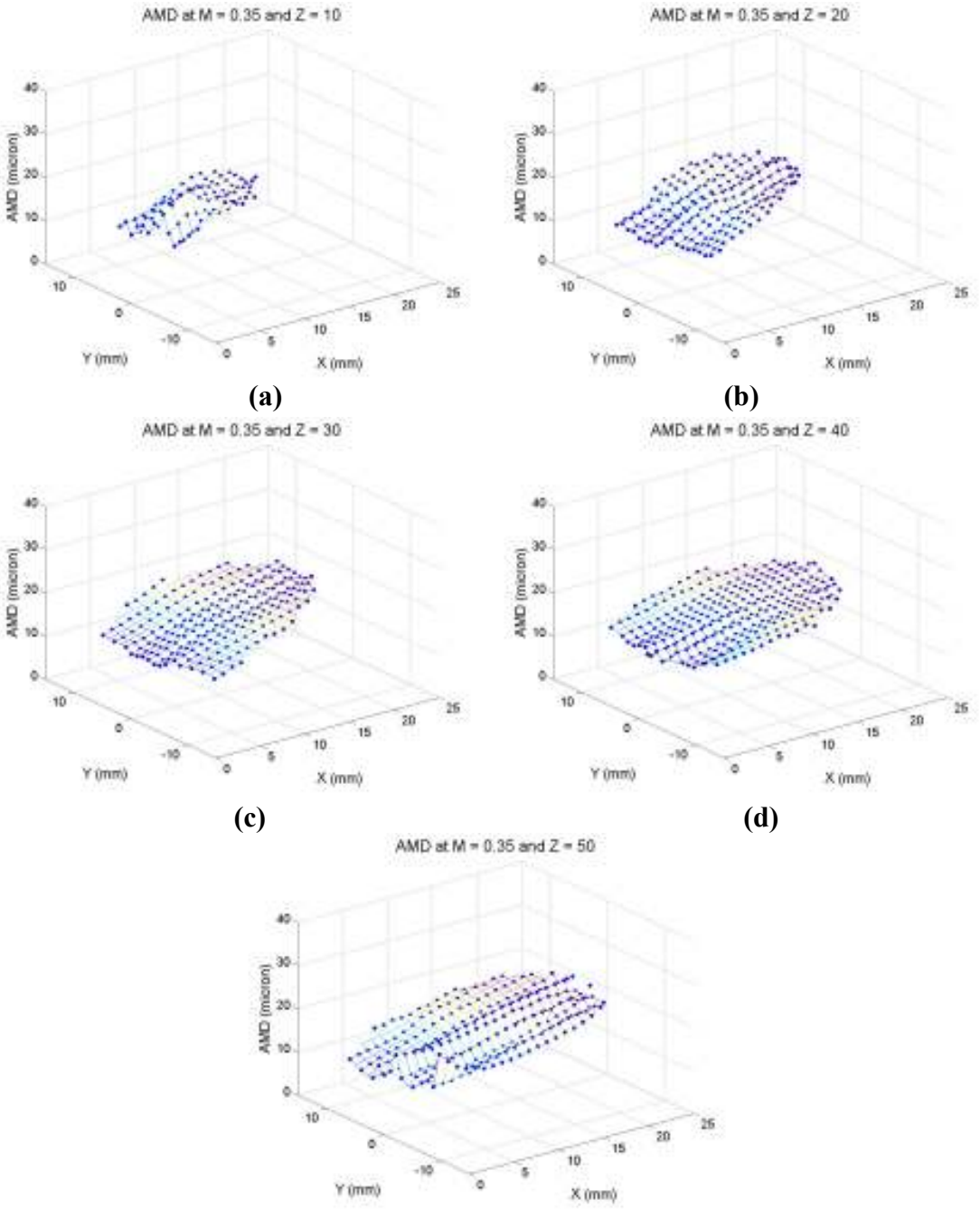

Figure A.5: Arithmetic Mean Diameter at M=0.35 for different Z locations
(a) Z=10mm (b) Z=20mm (c) Z=30mm (d) Z=40mm (e) Z=50mm

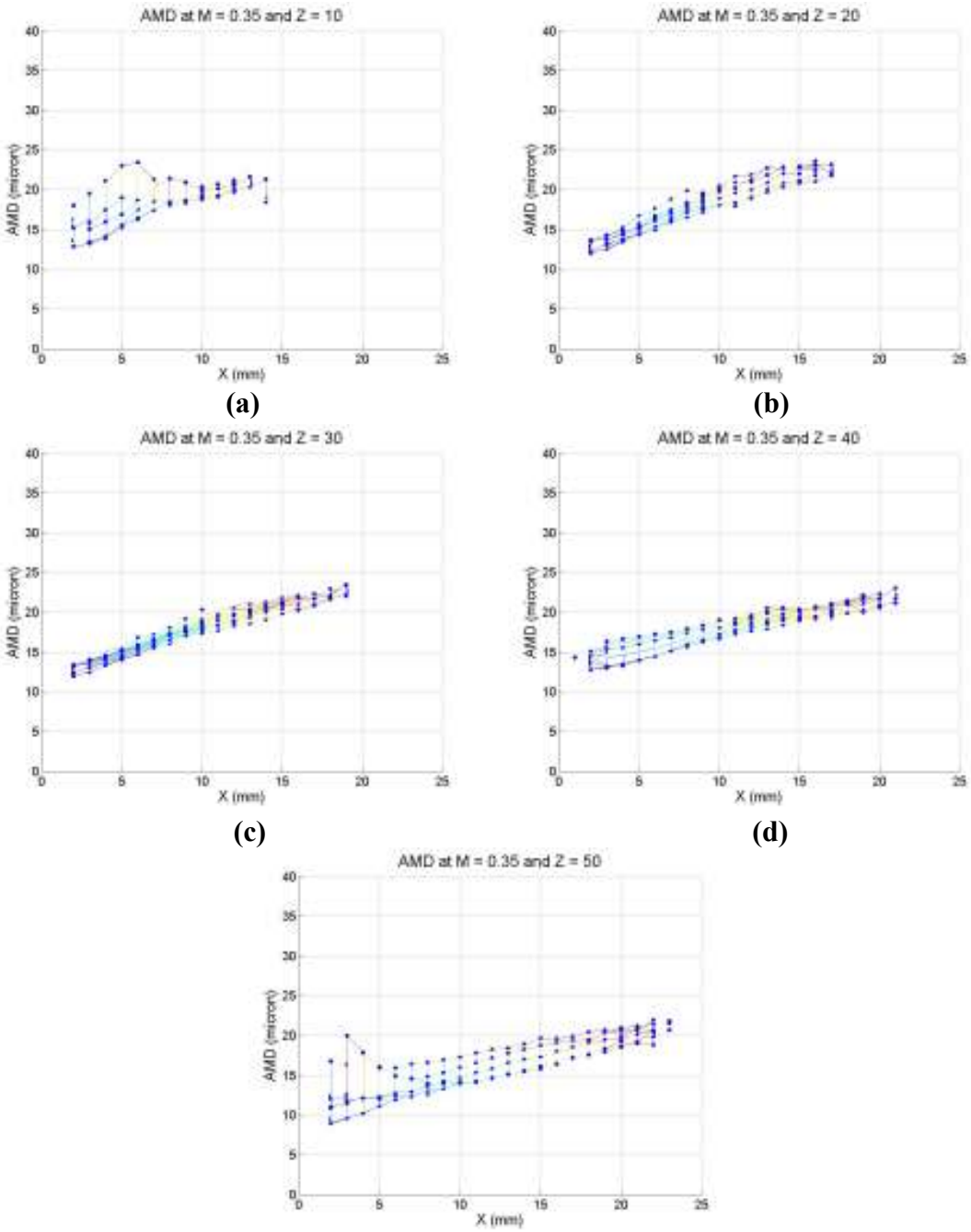

(a) **(b)** **(c)** **(d)** **(e)**

Figure A.6: Arithmetic Mean Diameter, view along x-axis at M=0.35 for different Z locations

(a) Z=10mm (b) Z=20mm (c) Z=30mm (d) Z=40mm (e) Z=50mm

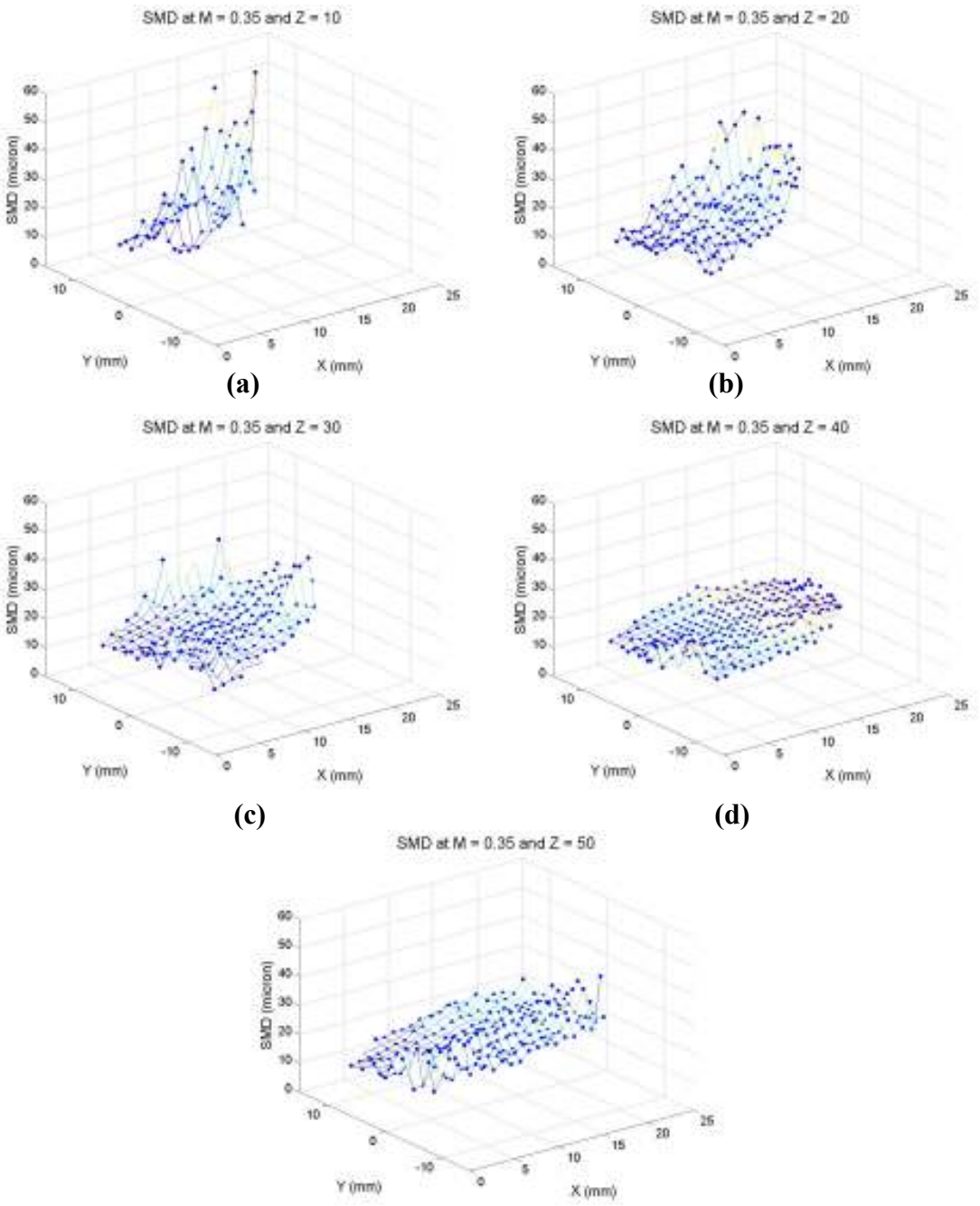

Figure A.7: Sauter Mean Diameter at M=0.35 for different Z locations
(a) Z=10mm (b) Z=20mm (c) Z=30mm (d) Z=40mm (e) Z=50mm

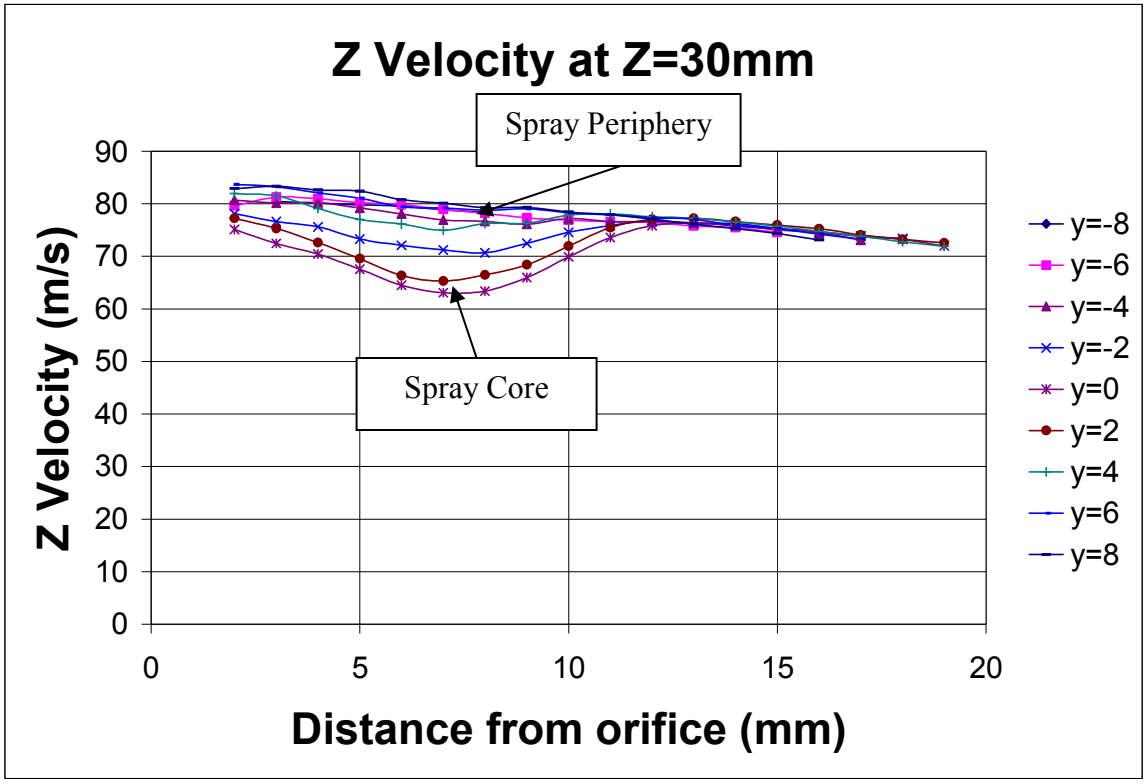

(a)

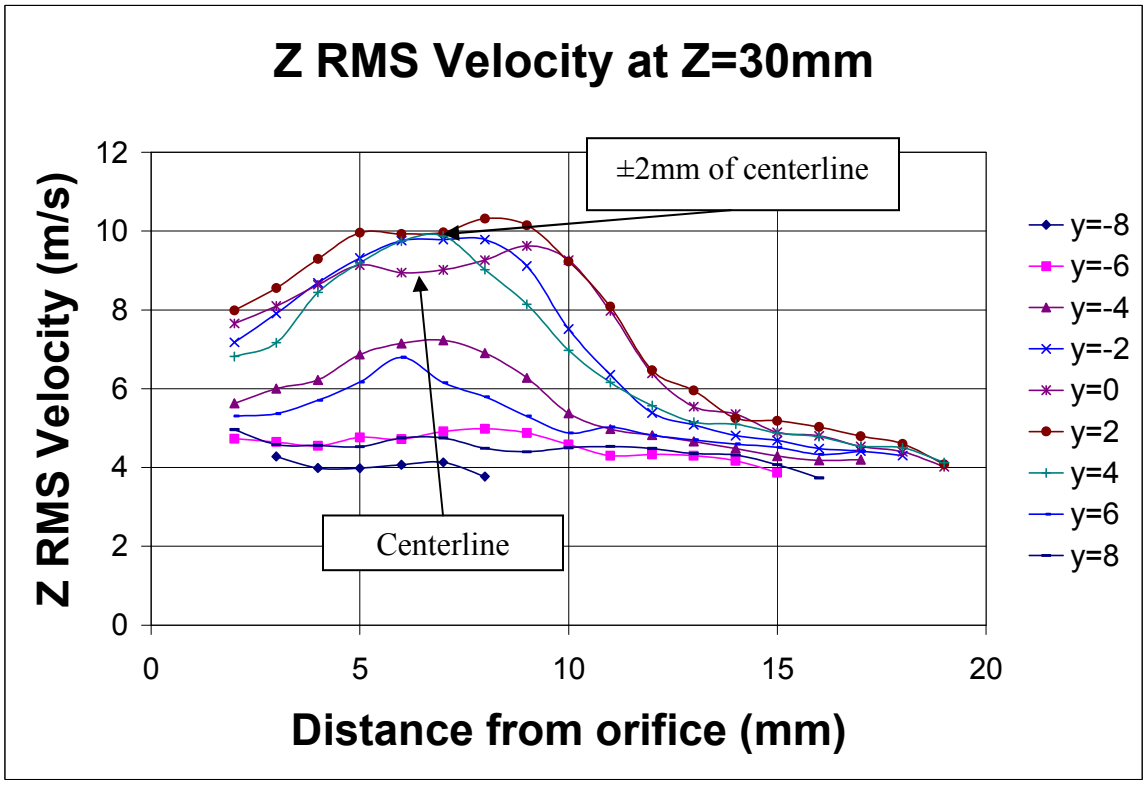

(b)

Figure A.8: Z Velocities in the plane of Z=30mm at M=0.2
(a) Average Velocity (b) Z RMS Velocity

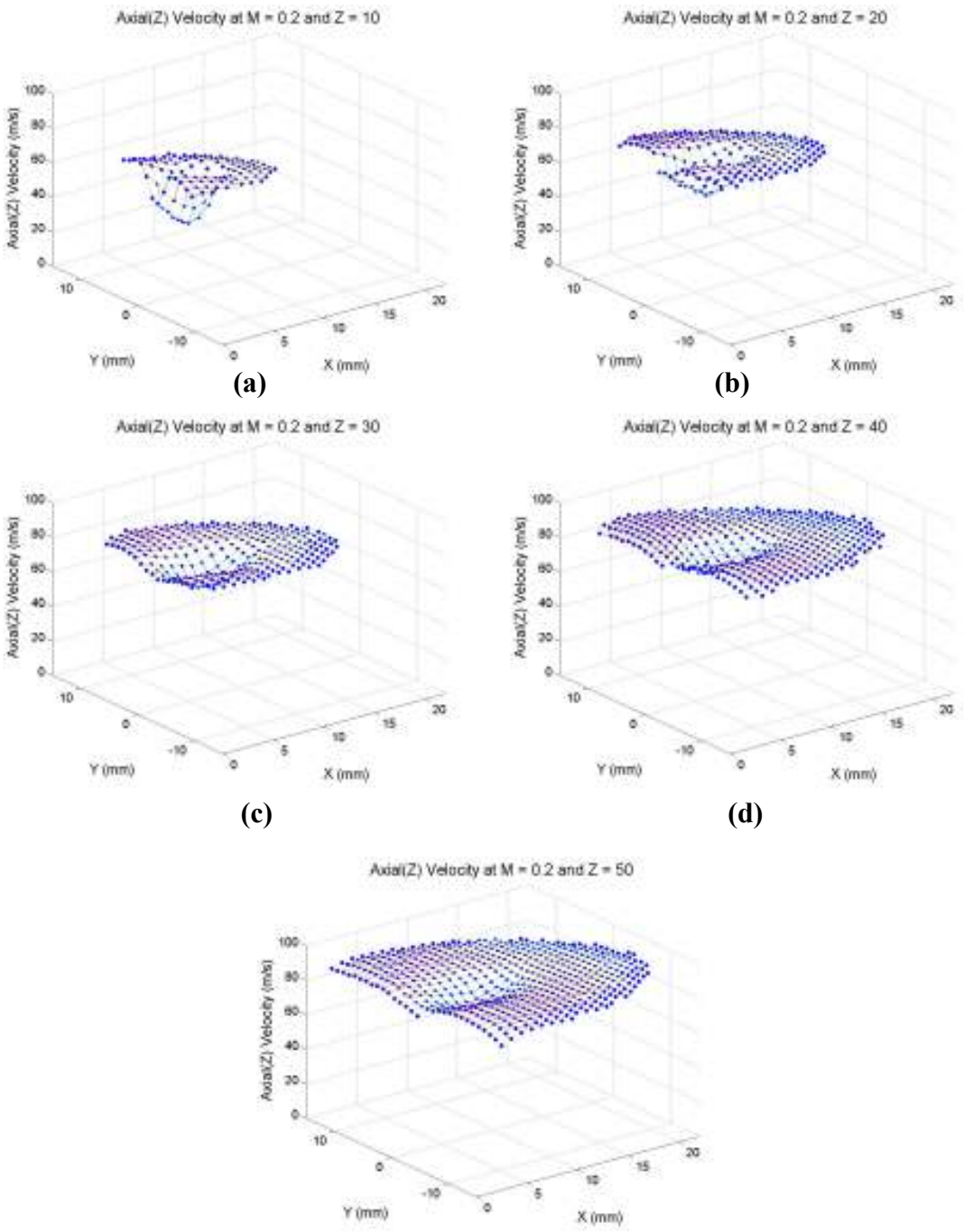

Figure A.9: Z Velocity at M=0.2 for different Z locations
(a) Z=10mm (b) Z=20mm (c) Z=30mm (d) Z=40mm (e) Z=50mm

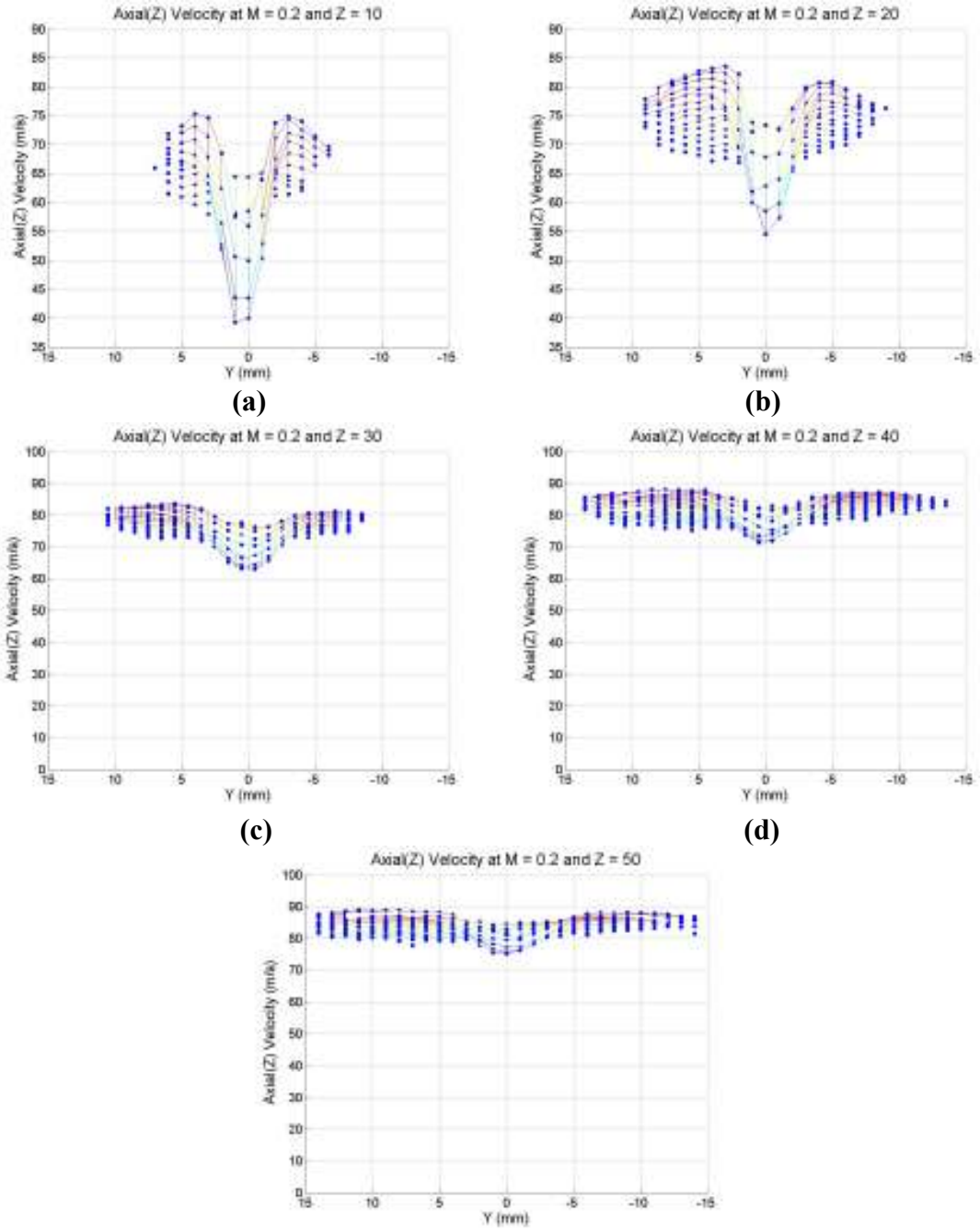

Figure A.10: Z Velocity, view along y-axis at M=0.2 for different Z locations (a) Z=10mm (b) Z=20mm (c) Z=30mm (d) Z=40mm (e) Z=50mm

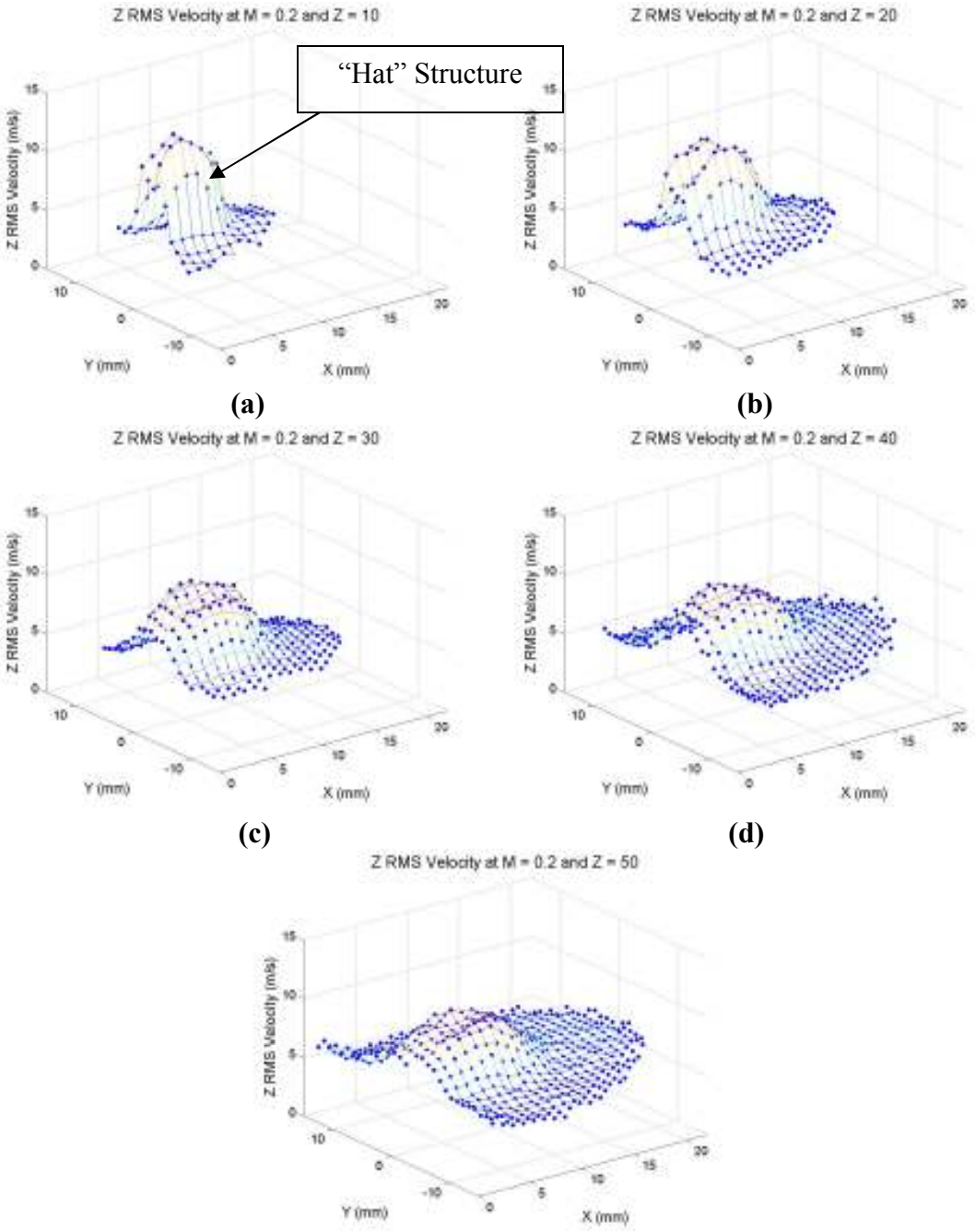

Figure A.11: Z RMS Velocity at M=0.2 for different Z locations
(a) Z=10mm (b) Z=20mm (c) Z=30mm (d) Z=40mm (e) Z=50mm

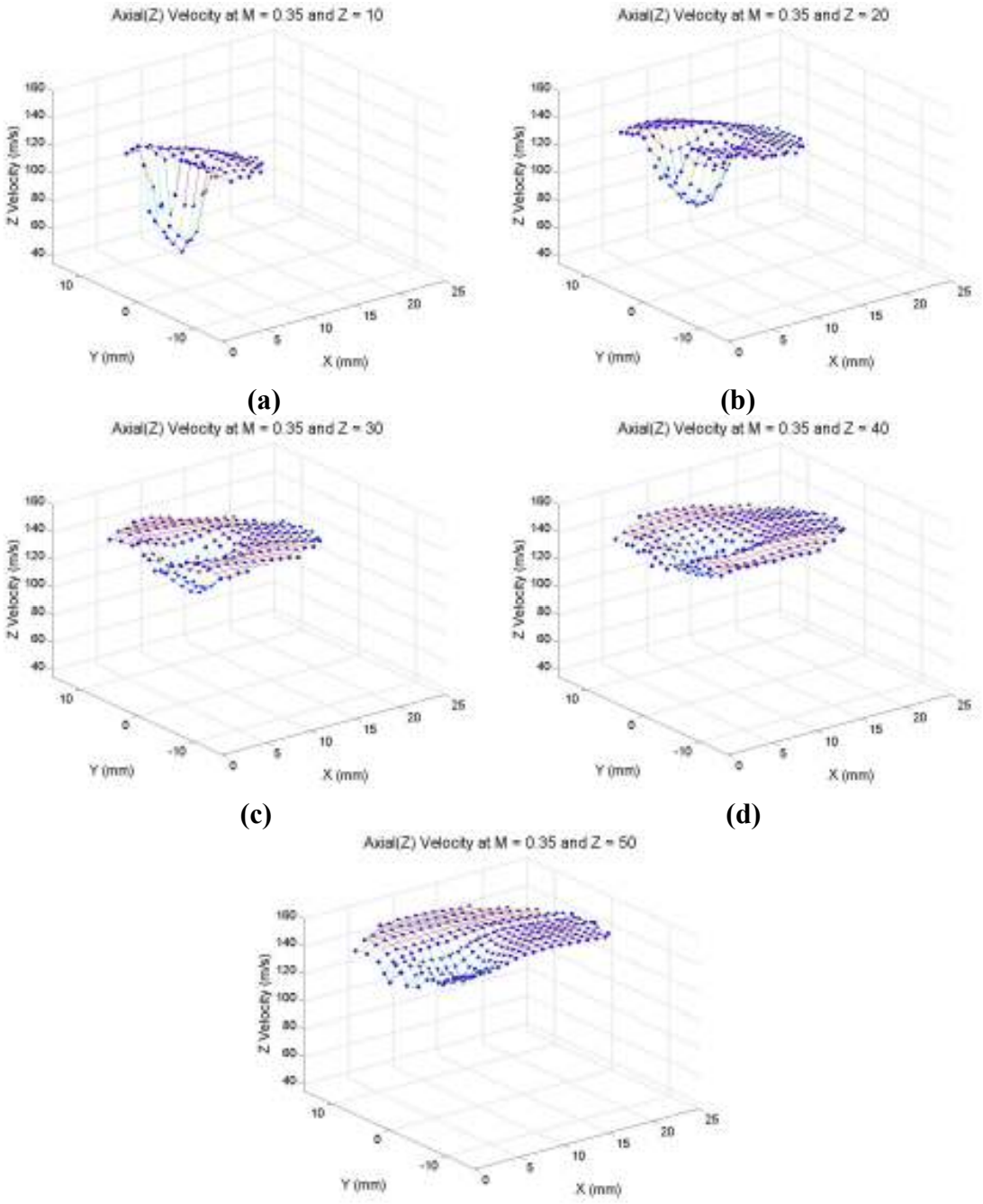

(a) **(b)** **(c)** **(d)** **(e)**

Figure A.12: Z Velocity at M=0.35 for different Z locations
(a) Z=10mm (b) Z=20mm (c) Z=30mm (d) Z=40mm (e) Z=50mm

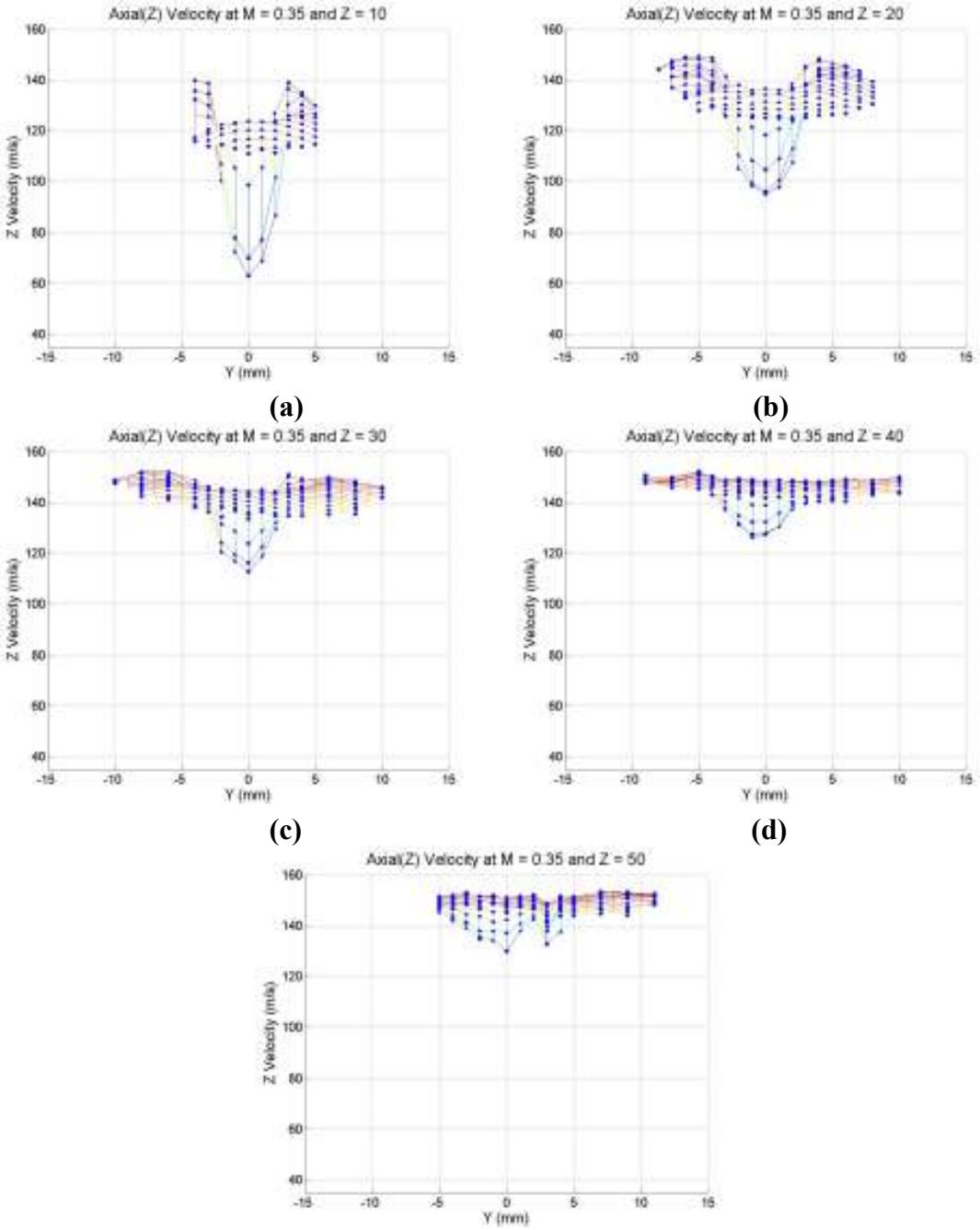

Figure A.13: Z Velocity, view along y-axis at M=0.35 for different Z locations (a) Z=10mm (b) Z=20mm (c) Z=30mm (d) Z=40mm (e) Z=50mm

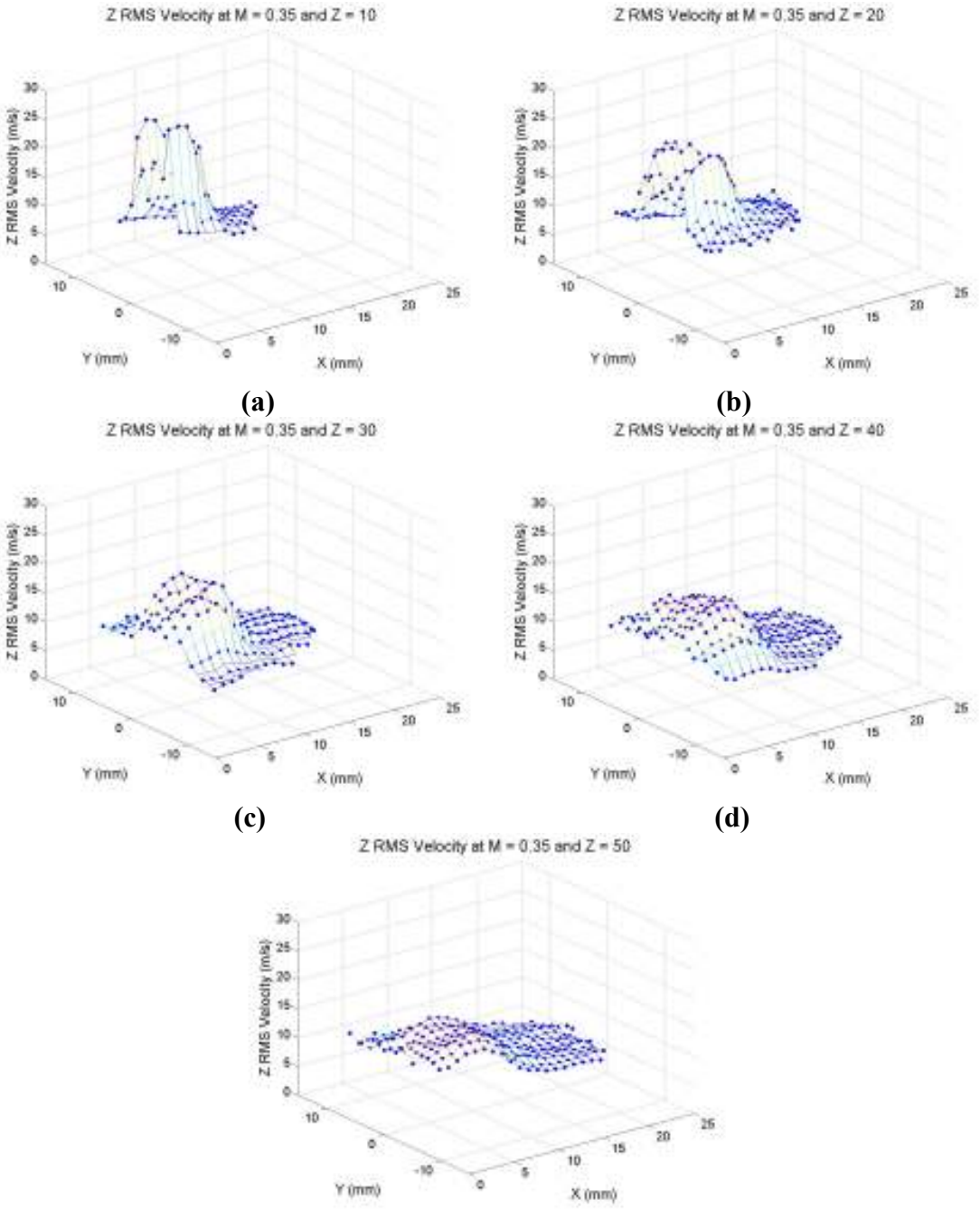

(a) **(b)**

(c) **(d)**

(e)

Figure A.14: Z RMS Velocity at M=0.35 for different Z locations
(a) Z=10mm (b) Z=20mm (c) Z=30mm (d) Z=40mm (e) Z=50mm

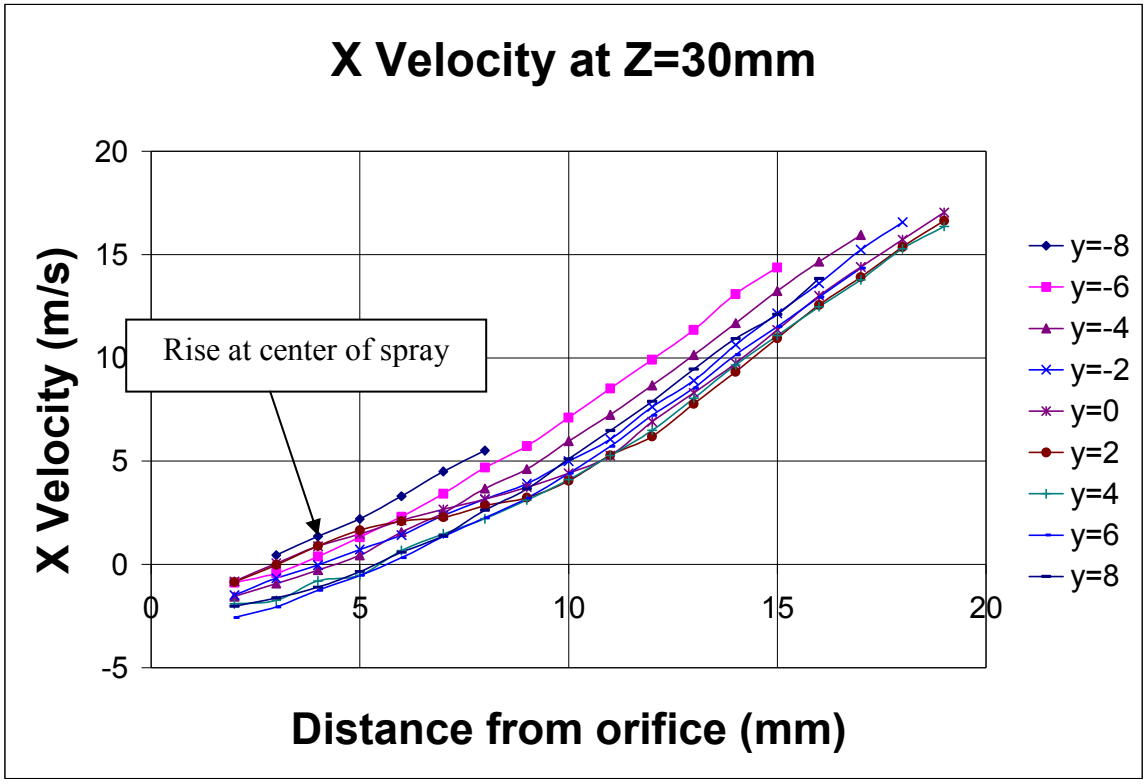

(a)

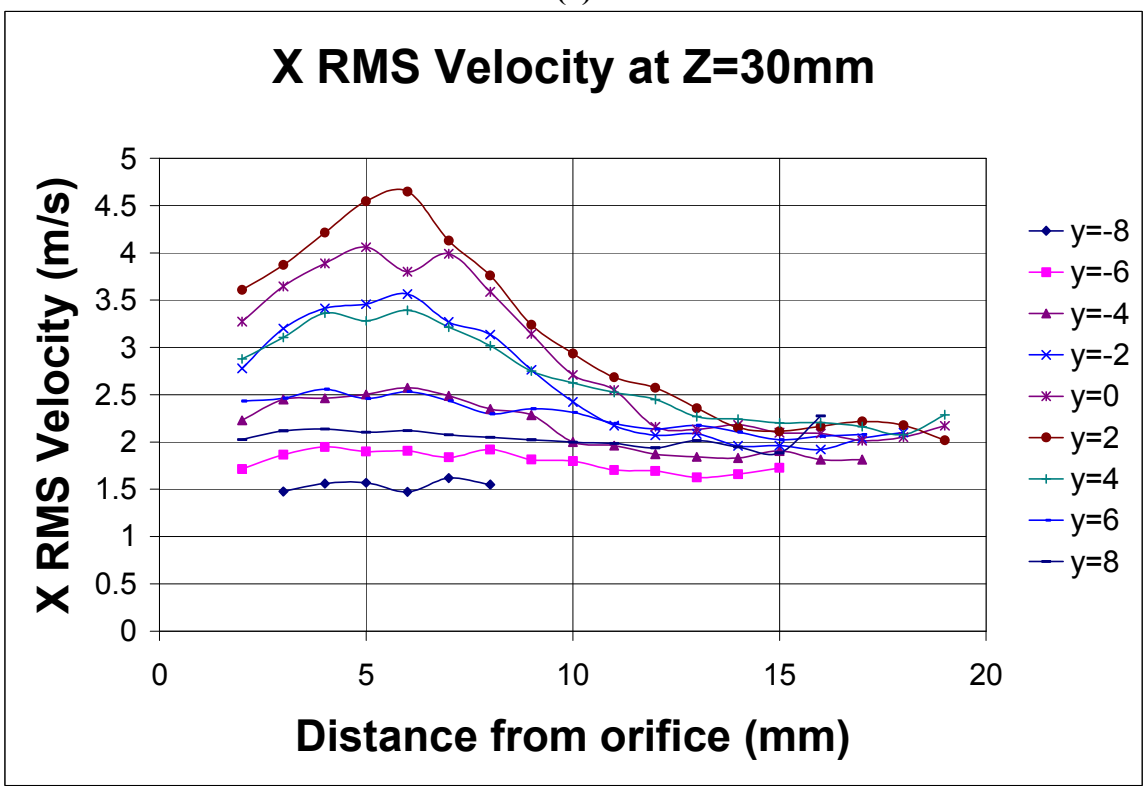

(b)

Figure A.15: X Velocities in the plane of Z=30mm at M=0.2
(a) Average Velocity (b) X RMS Velocity

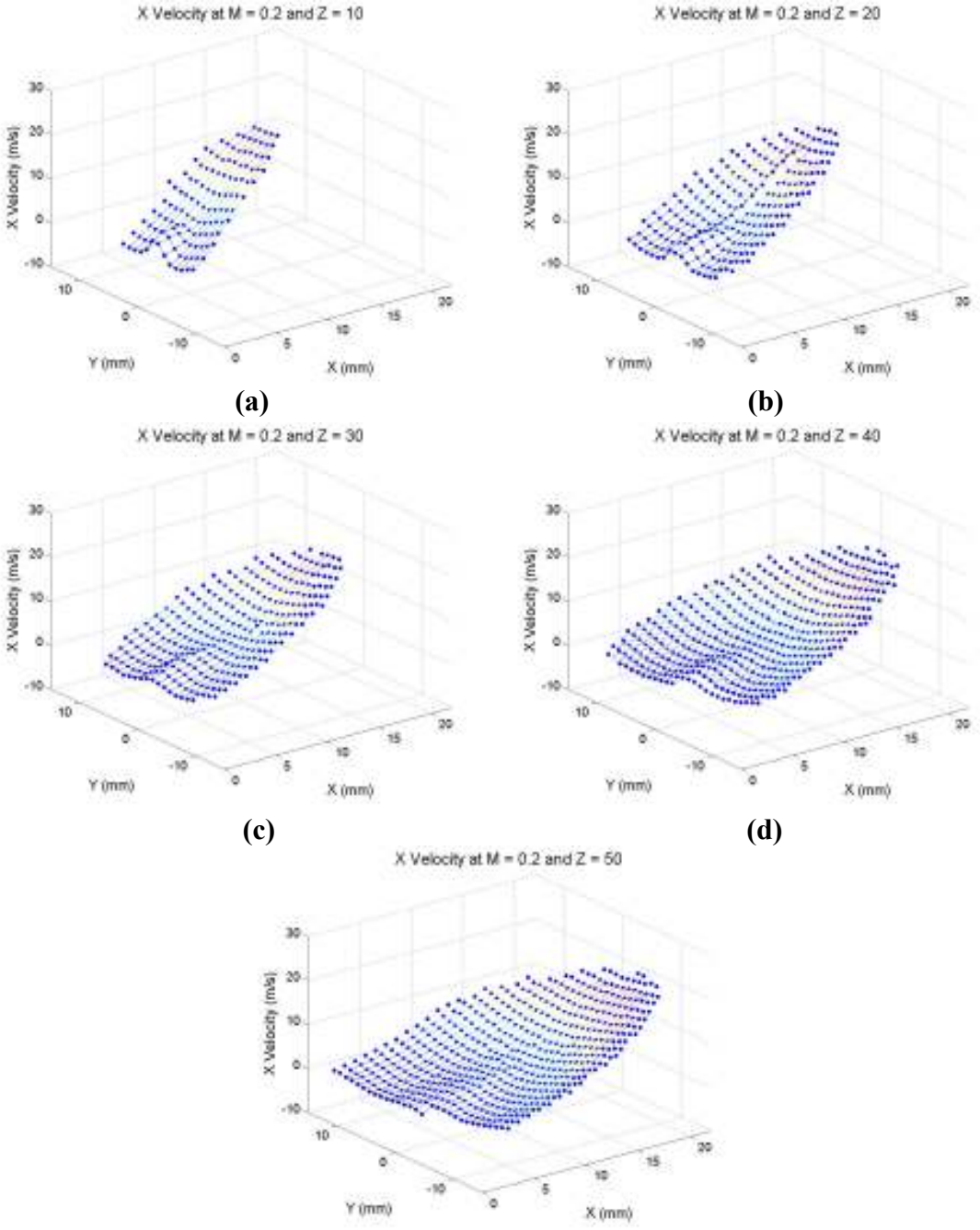

(a) **(b)**

(c) **(d)**

(e)

Figure A.16: X velocity at M=0.2 for different Z locations

(a) Z=10mm (b) Z=20mm (c) Z=30mm (d) Z=40mm (e) Z=50mm

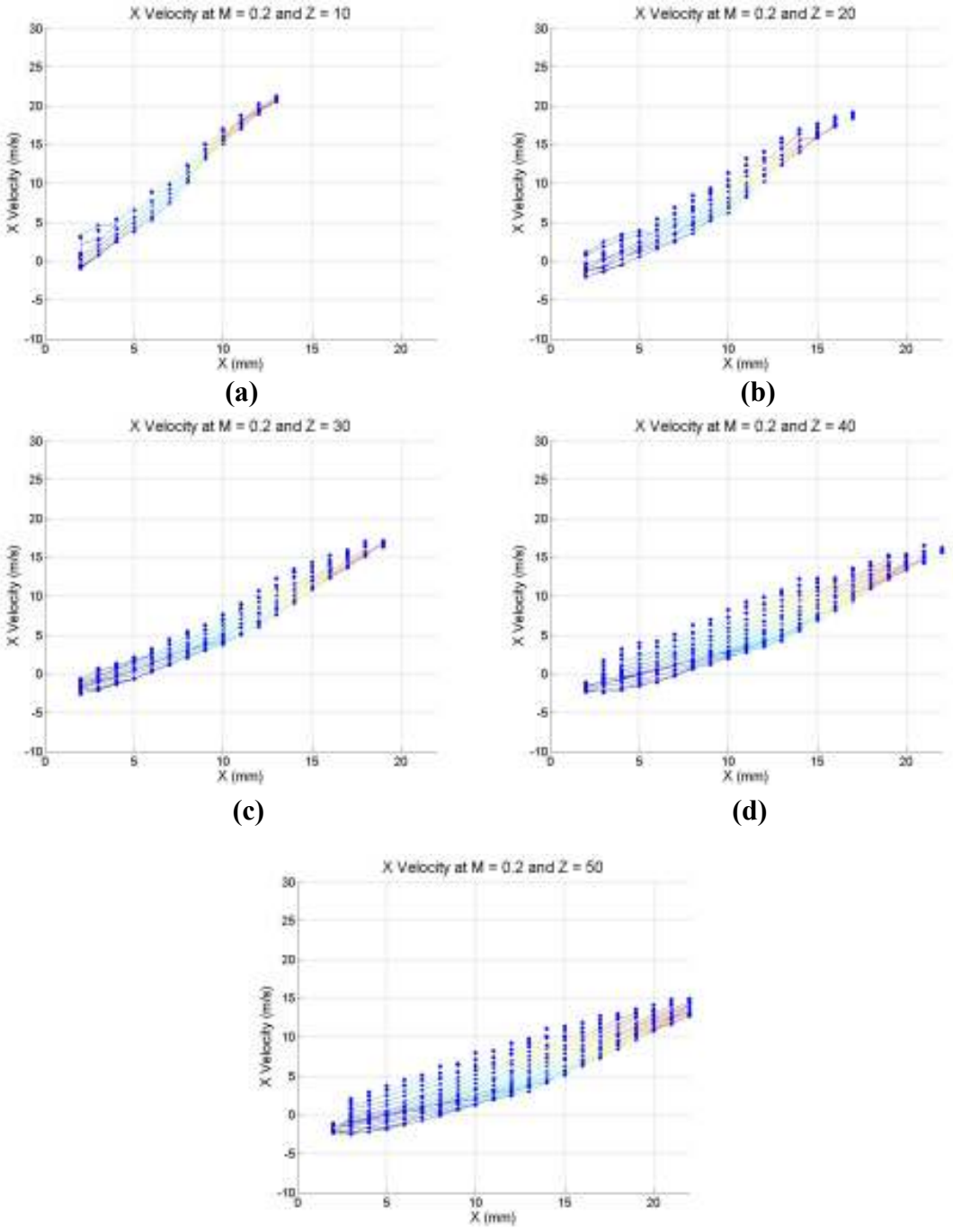

Figure A.17: X velocity, view along x-axis at M=0.2 for different Z locations (a) Z=10mm (b) Z=20mm (c) Z=30mm (d) Z=40mm (e) Z=50mm

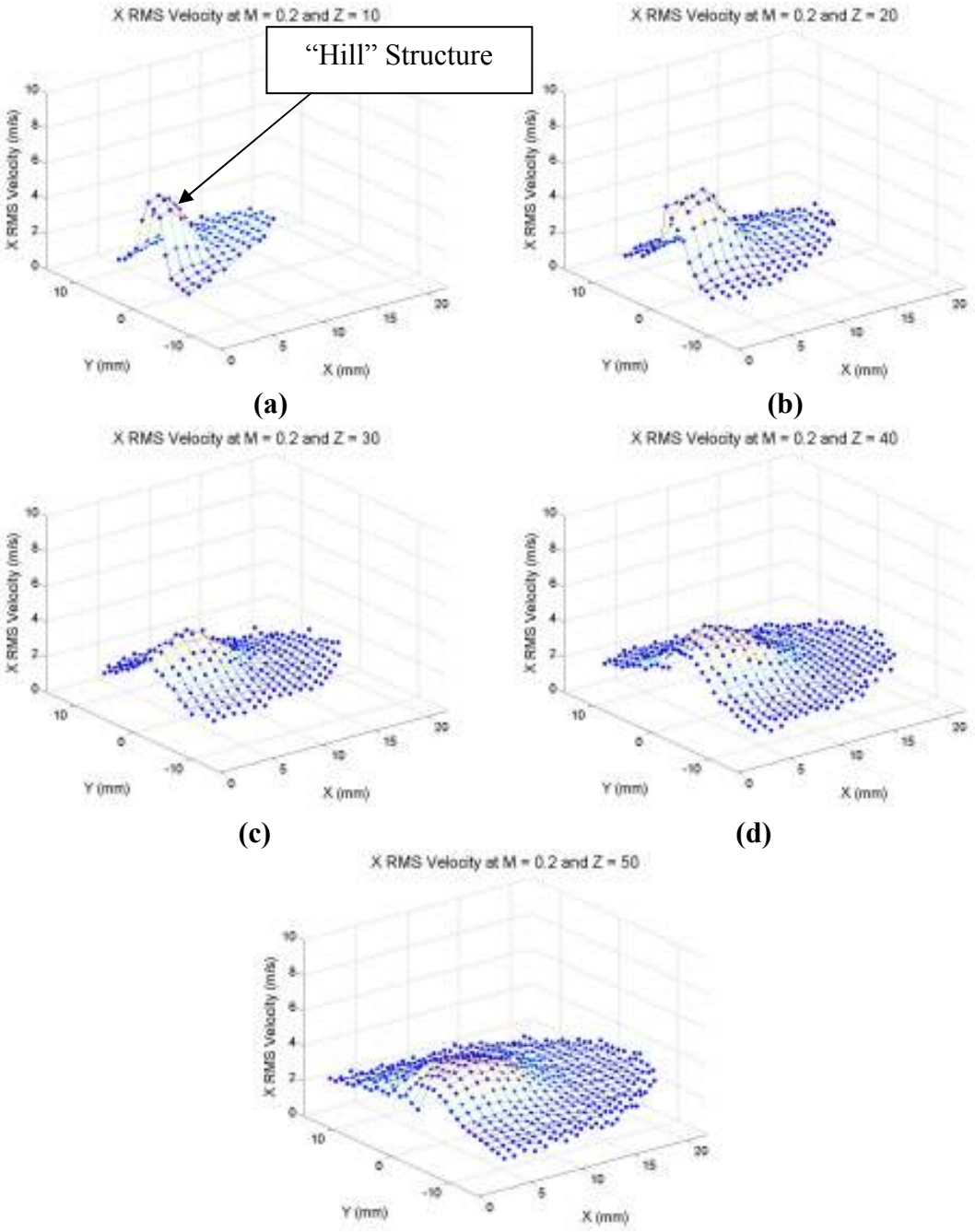

Figure A.18: X RMS Velocity at M=0.2 for different Z locations
(a) Z=10mm (b) Z=20mm (c) Z=30mm (d) Z=40mm (e) Z=50mm

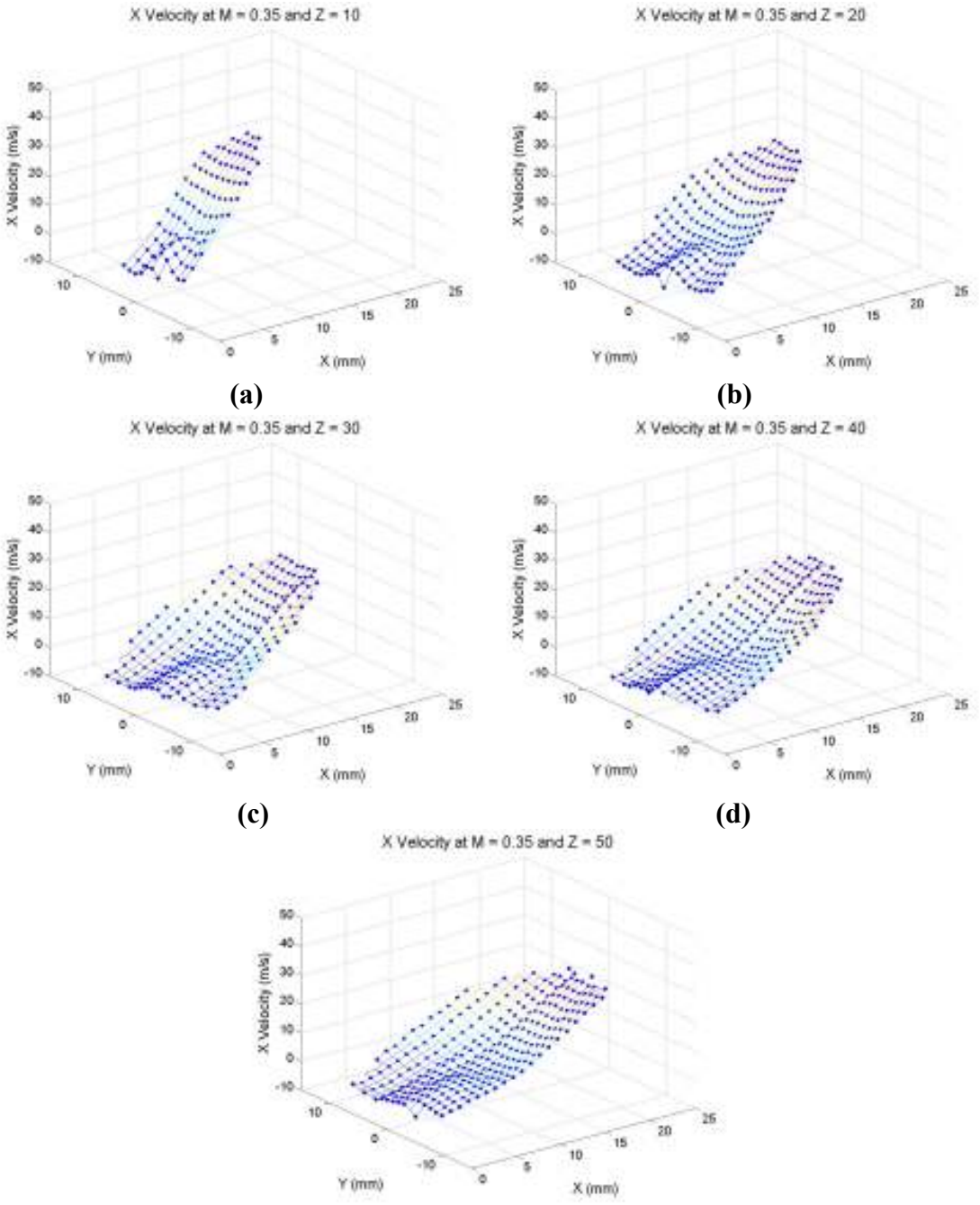

(a) **(b)**

(c) **(d)**

(e)

Figure A.19: X velocity at M=0.35 for different Z locations
(a) Z=10mm (b) Z=20mm (c) Z=30mm (d) Z=40mm (e) Z=50mm

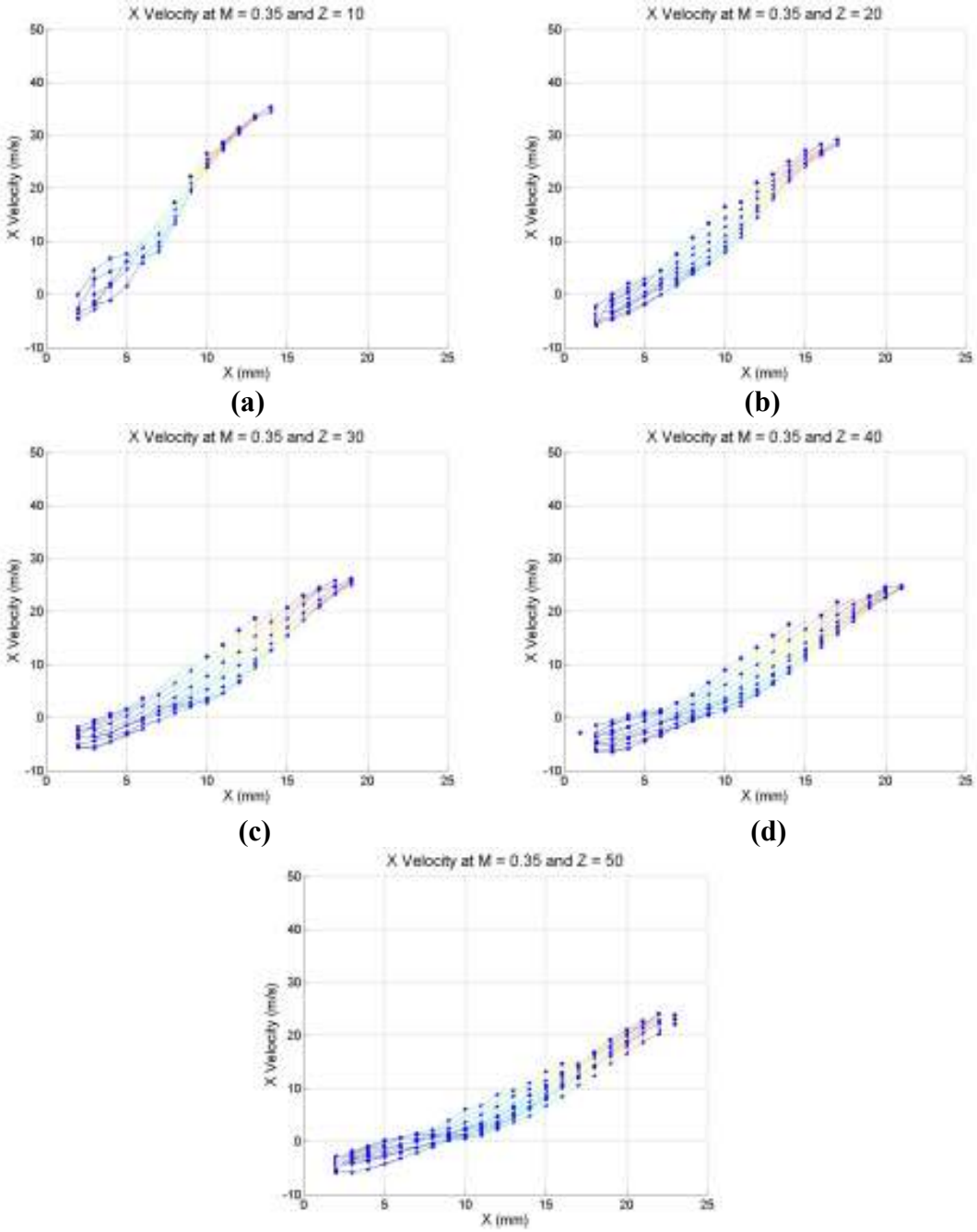

Figure A.20: X velocity, view along x-axis at M=0.35 for different Z locations (a) Z=10mm (b) Z=20mm (c) Z=30mm (d) Z=40mm (e) Z=50mm

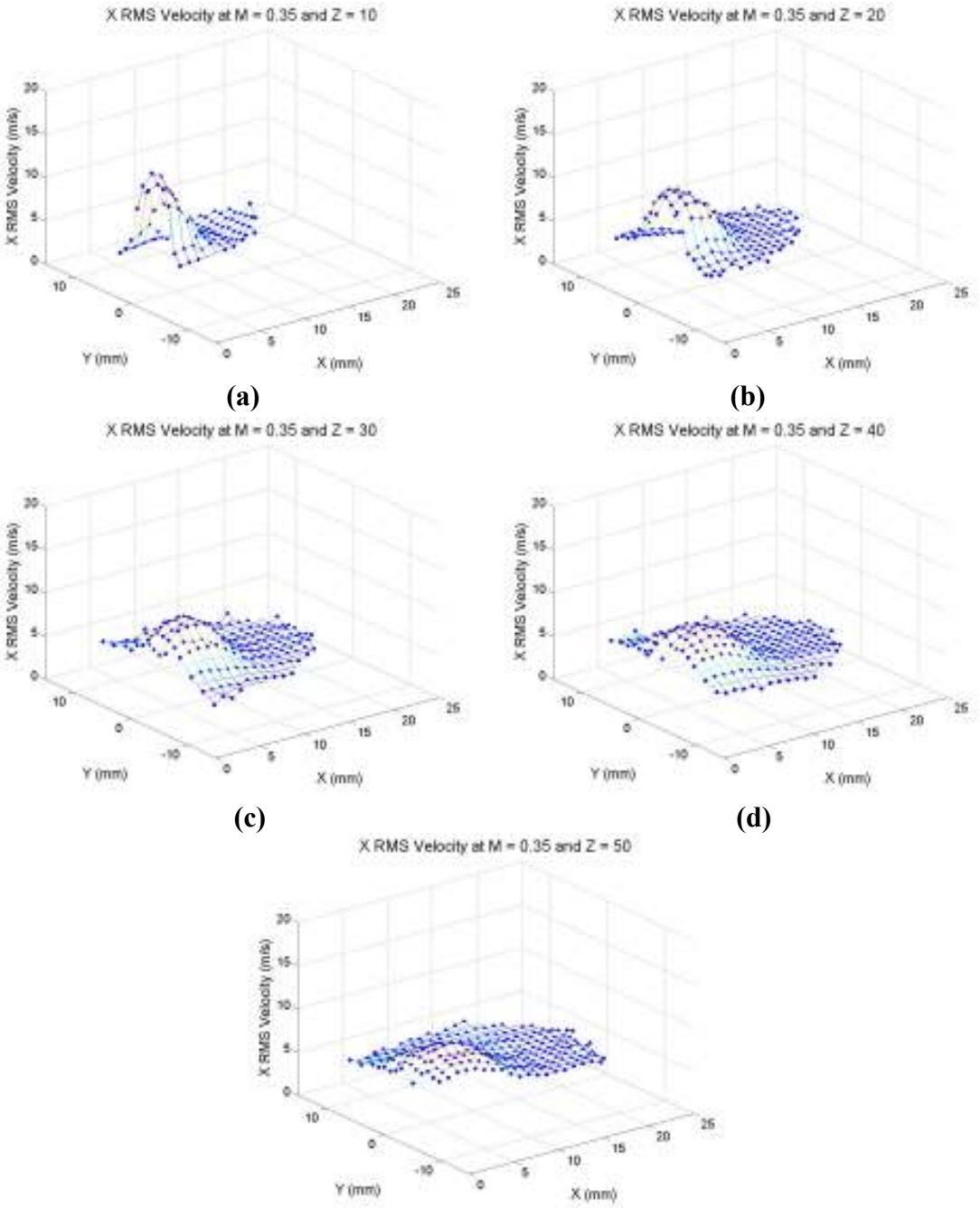

(a) **(b)** **(c)** **(d)** **(e)**

Figure A.21: X RMS Velocity at M=0.35 for different Z locations
(a) Z=10mm (b) Z=20mm (c) Z=30mm (d) Z=40mm (e) Z=50mm

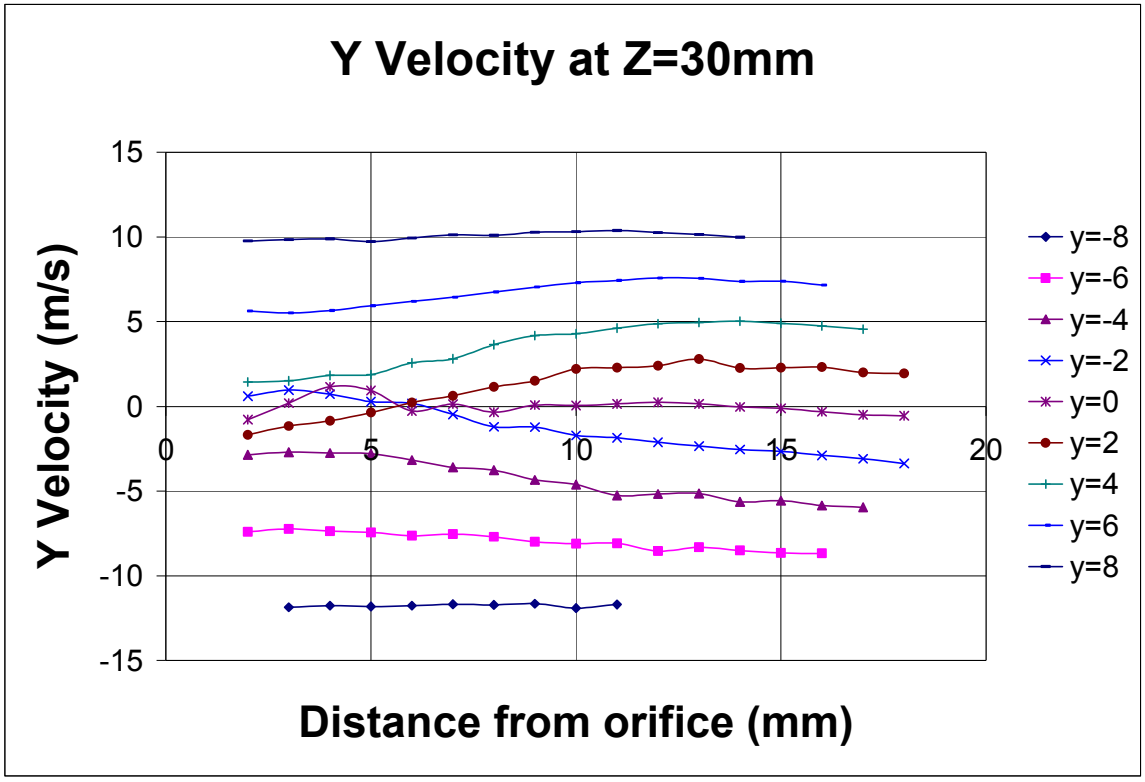

(a)

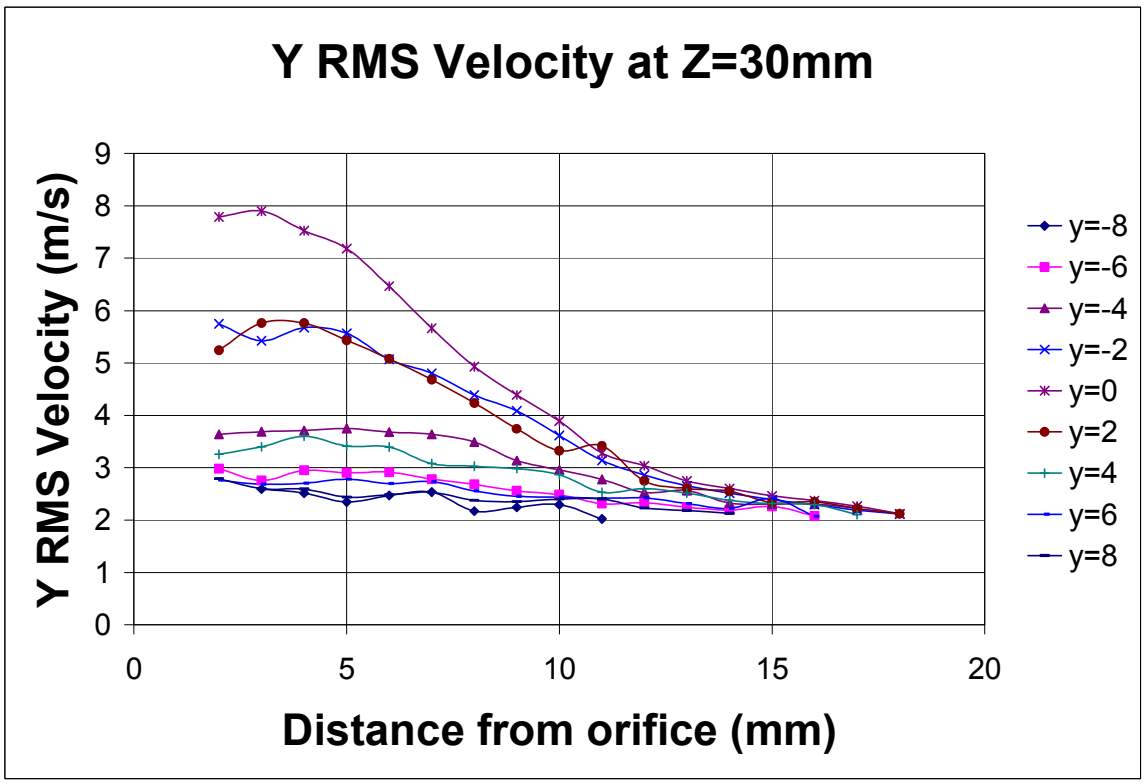

(b)

Figure A.22: Y velocities in the plane of Z=30mm at M=0.2
(a) Average Y velocities (b) Y RMS velocitiea

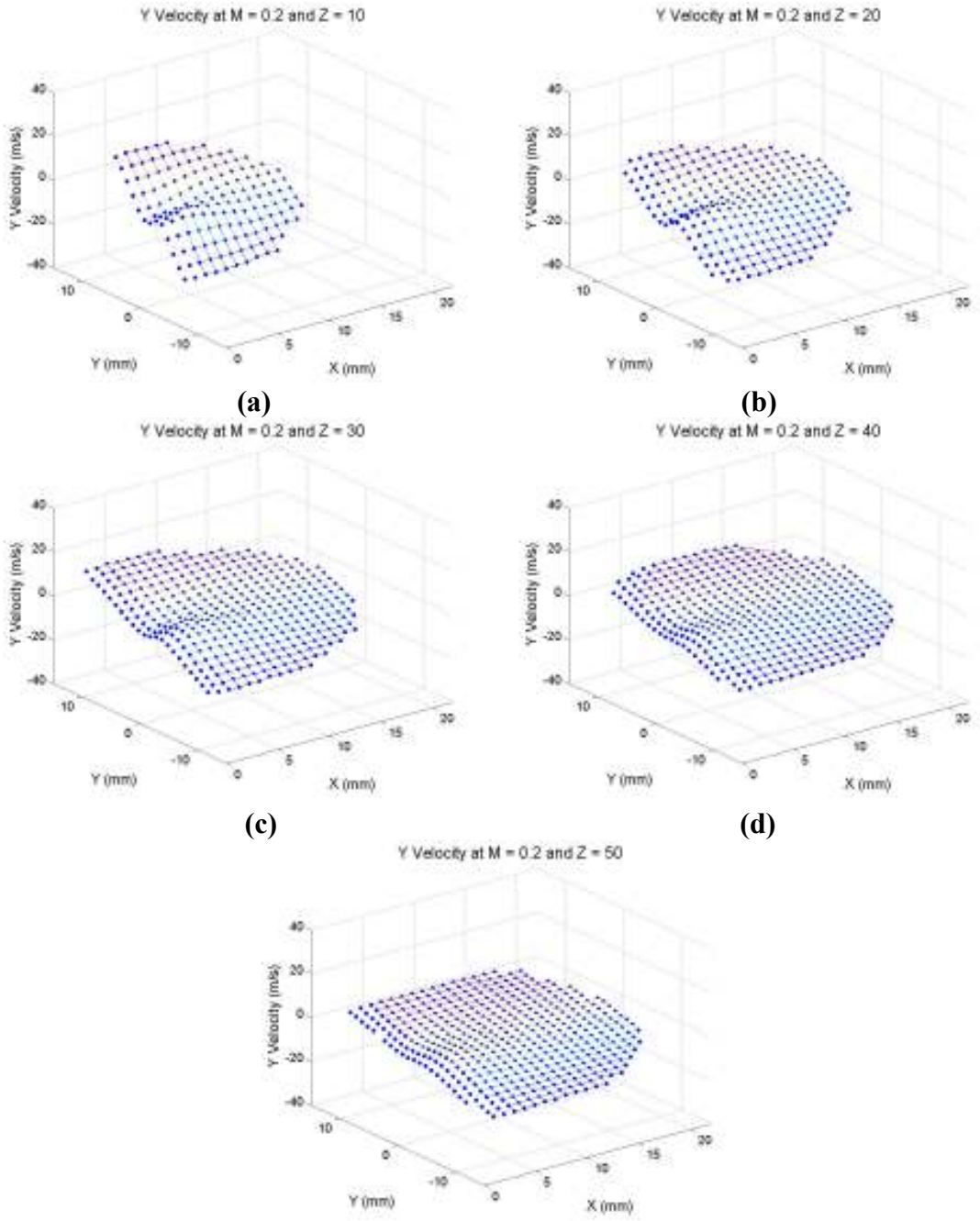

(a) **(b)** **(c)** **(d)** **(e)**

Figure A.23: Y Velocity at M=0.2 for different Z locations
(a) Z=10mm (b) Z=20mm (c) Z=30mm (d) Z=40mm (e) Z=50mm

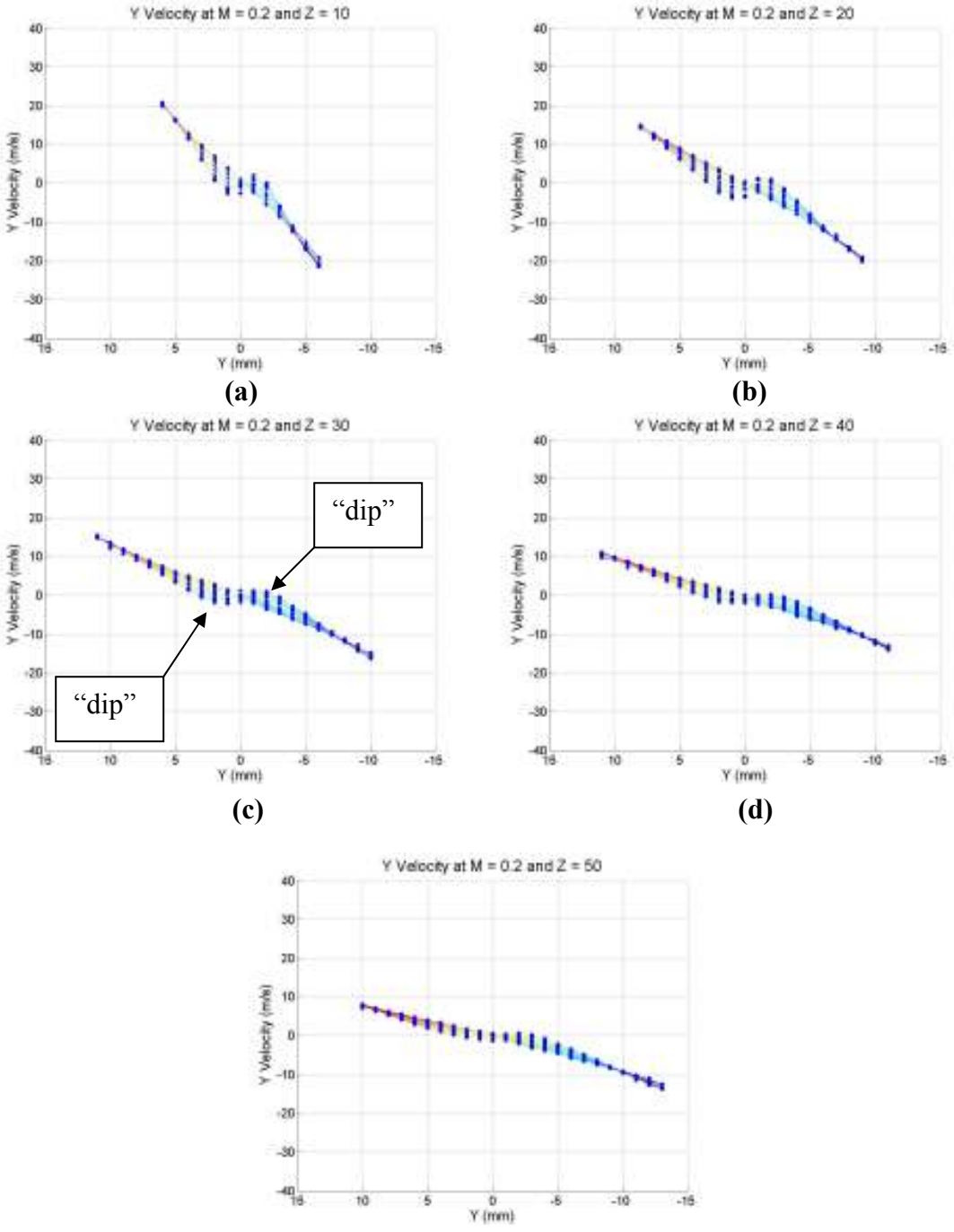

Figure A.24: Y Velocity, view along y-axis at M=0.2 for different Z locations (a) Z=10mm (b) Z=20mm (c) Z=30mm (d) Z=40mm (e) Z=50mm

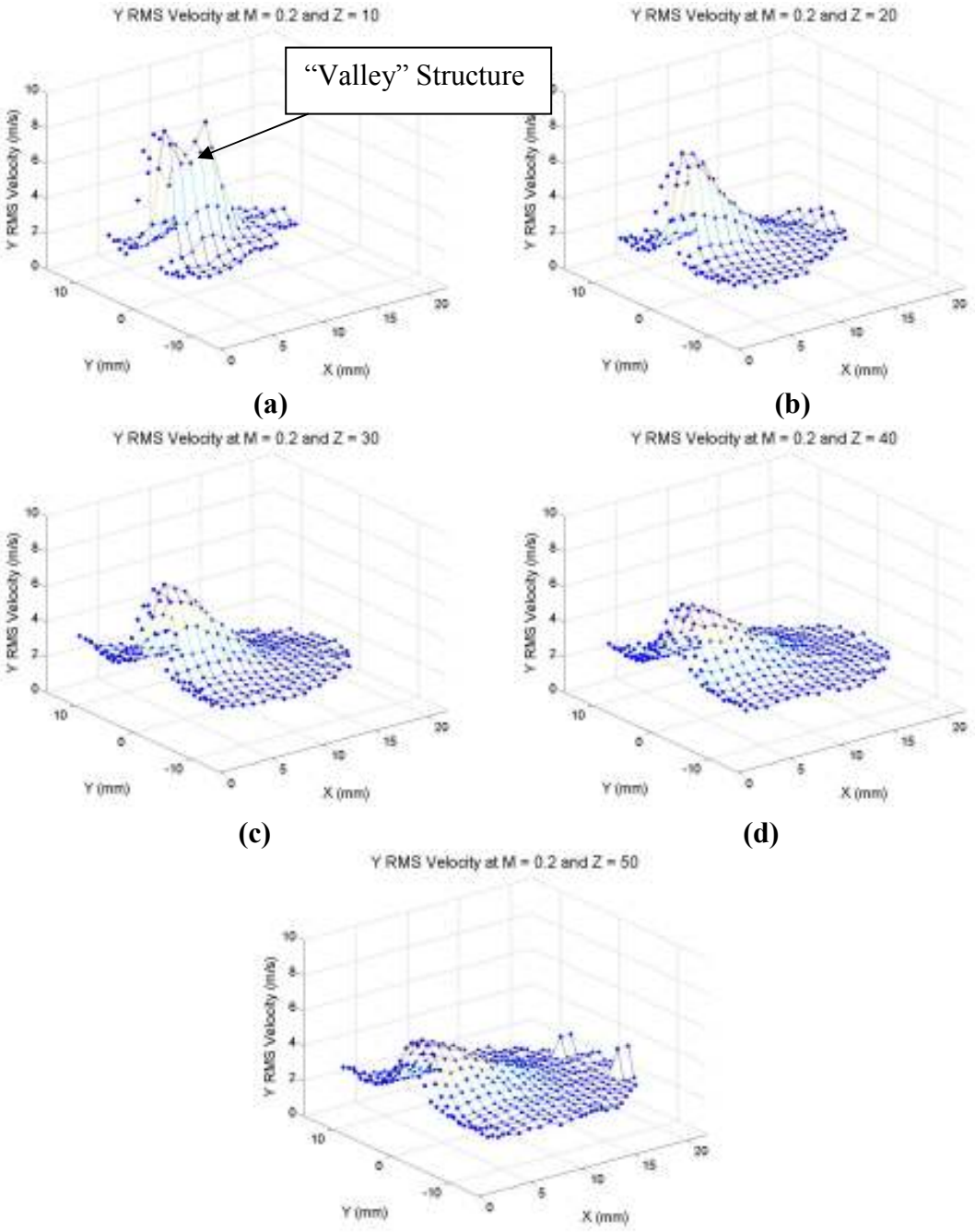

Figure A.25: Y RMS Velocity at M=0.2 for different Z locations
(a) Z=10mm (b) Z=20mm (c) Z=30mm (d) Z=40mm (e) Z=50mm

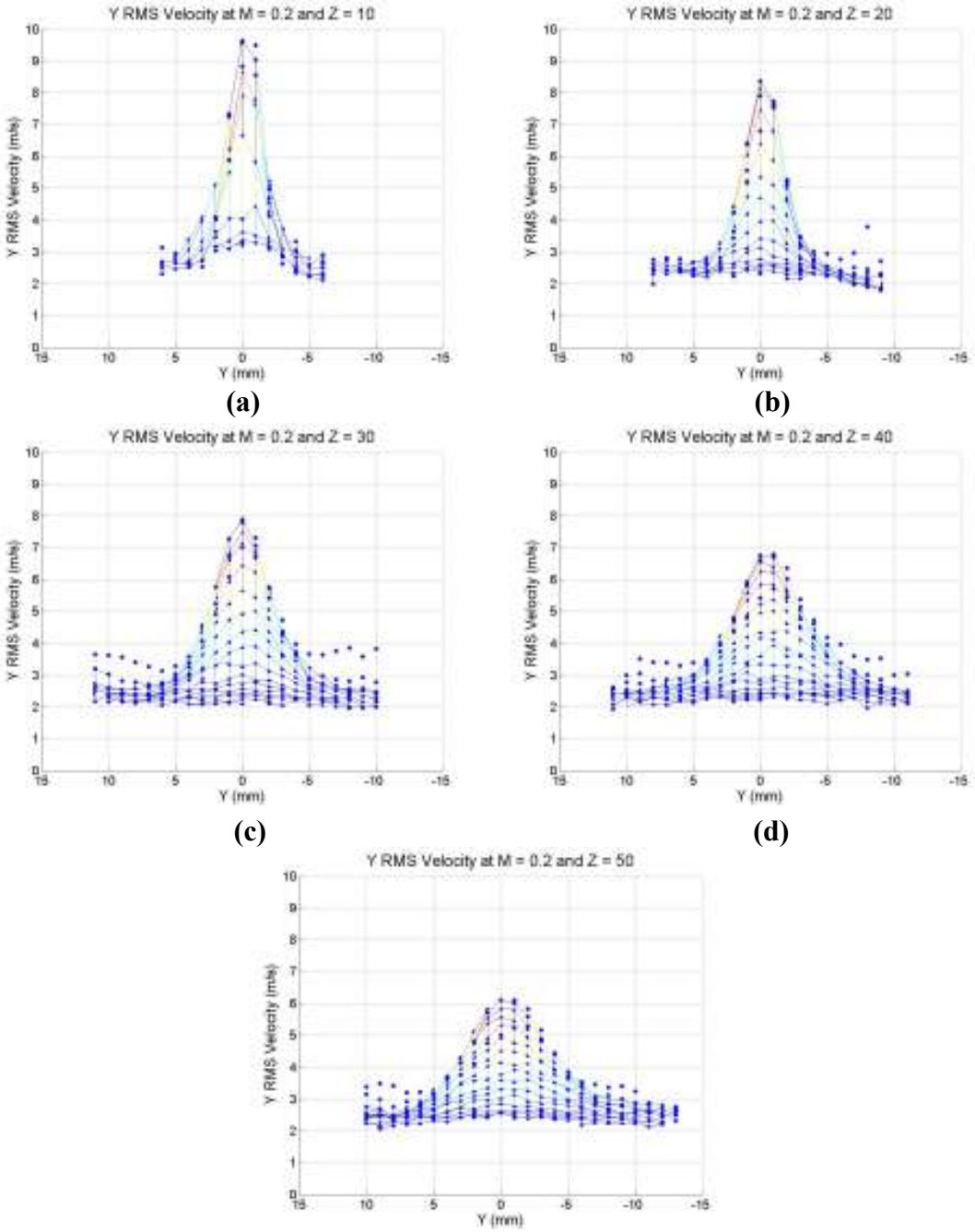

Figure A.26: Y RMS Velocity, view along y-axis at M=0.2 for different Z locations (a) Z=10mm (b) Z=20mm (c) Z=30mm (d) Z=40mm (e) Z=50mm

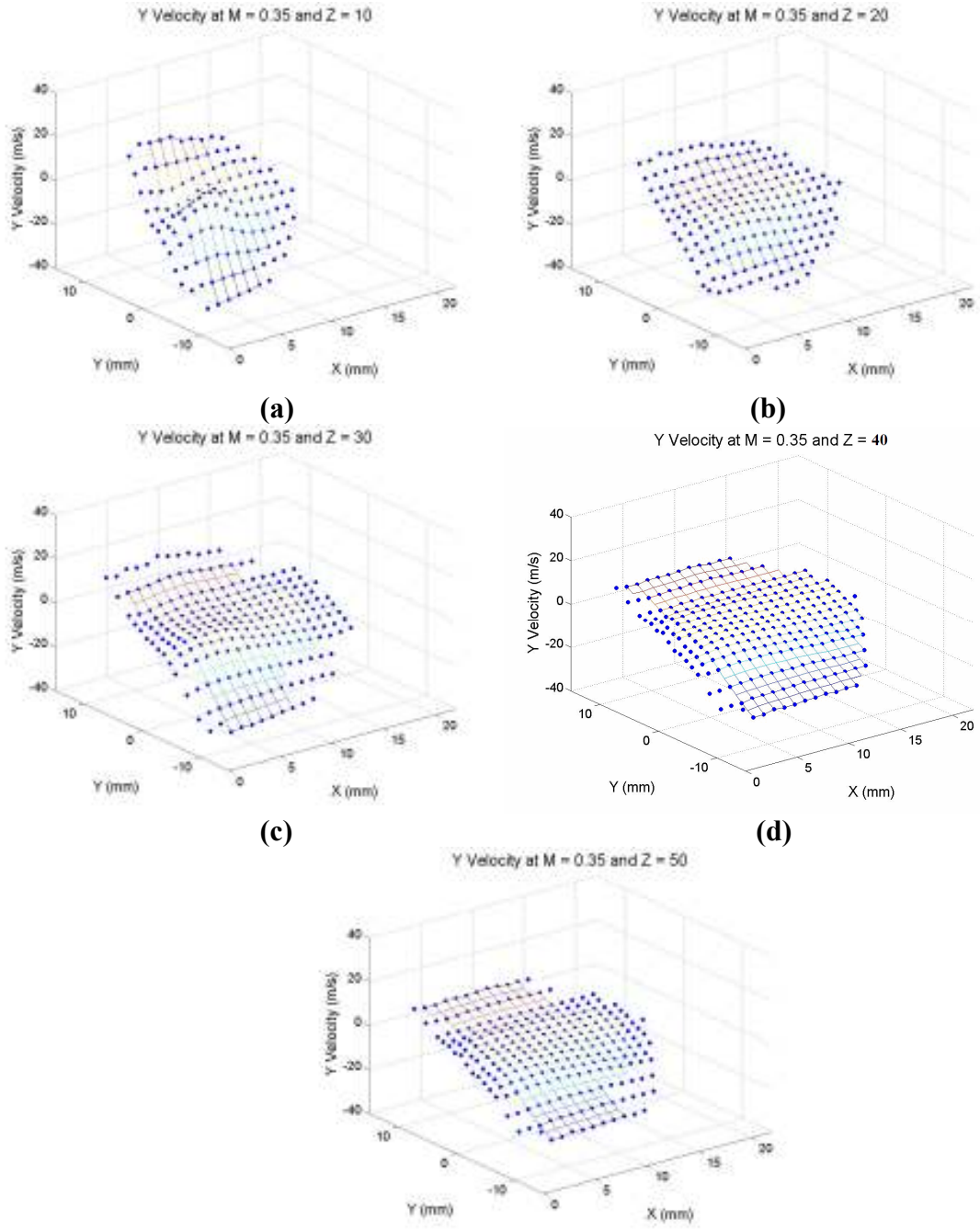

Figure A.27: Y Velocity at M=0.35 for different Z locations
(a) Z=10mm (b) Z=20mm (c) Z=30mm (d) Z=40mm (e) Z=50mm

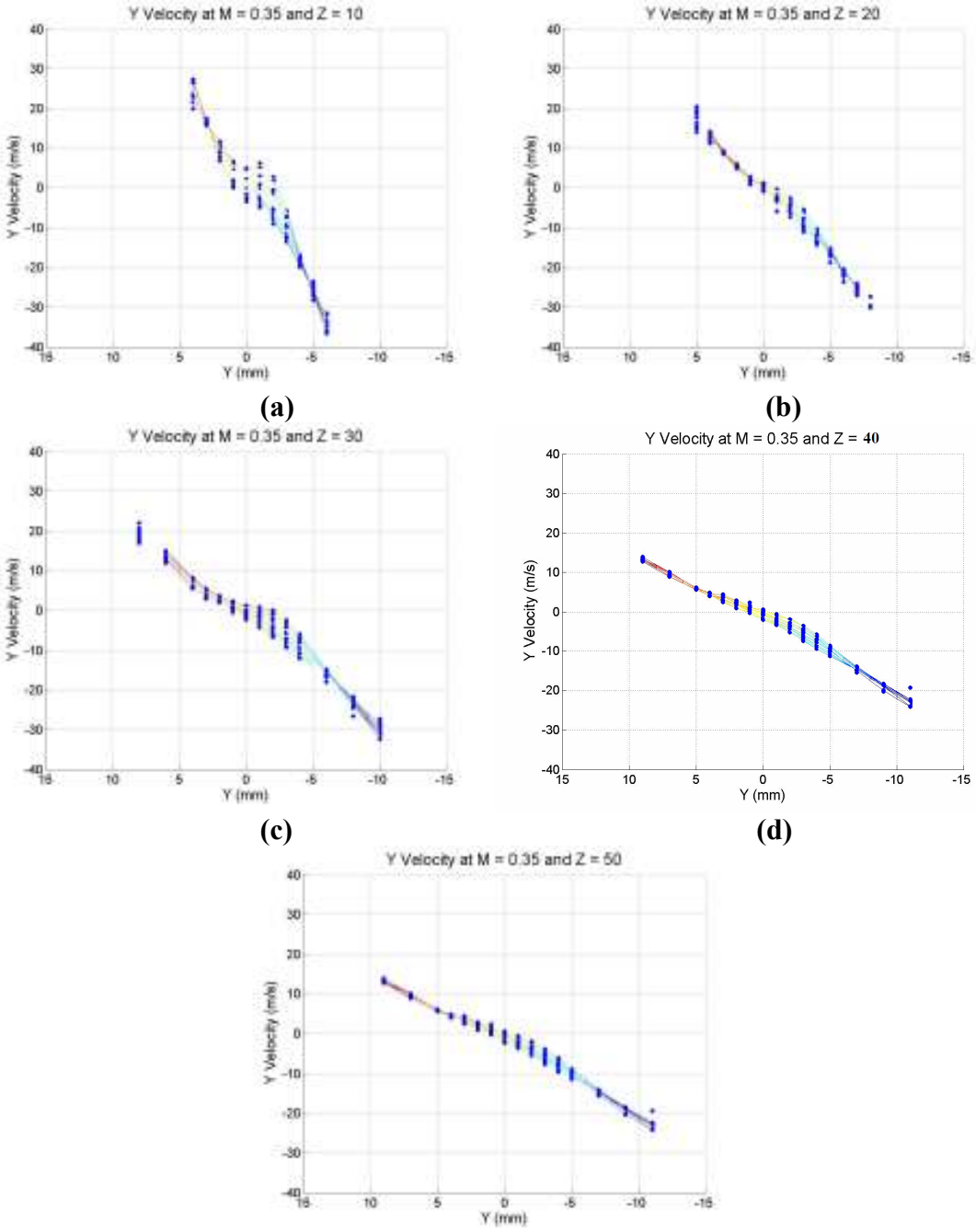

Figure A.28: Y Velocity, view along y-axis at M=0.35 for different Z locations (a) Z=10mm (b) Z=20mm (c) Z=30mm (d) Z=40mm (e) Z=50mm

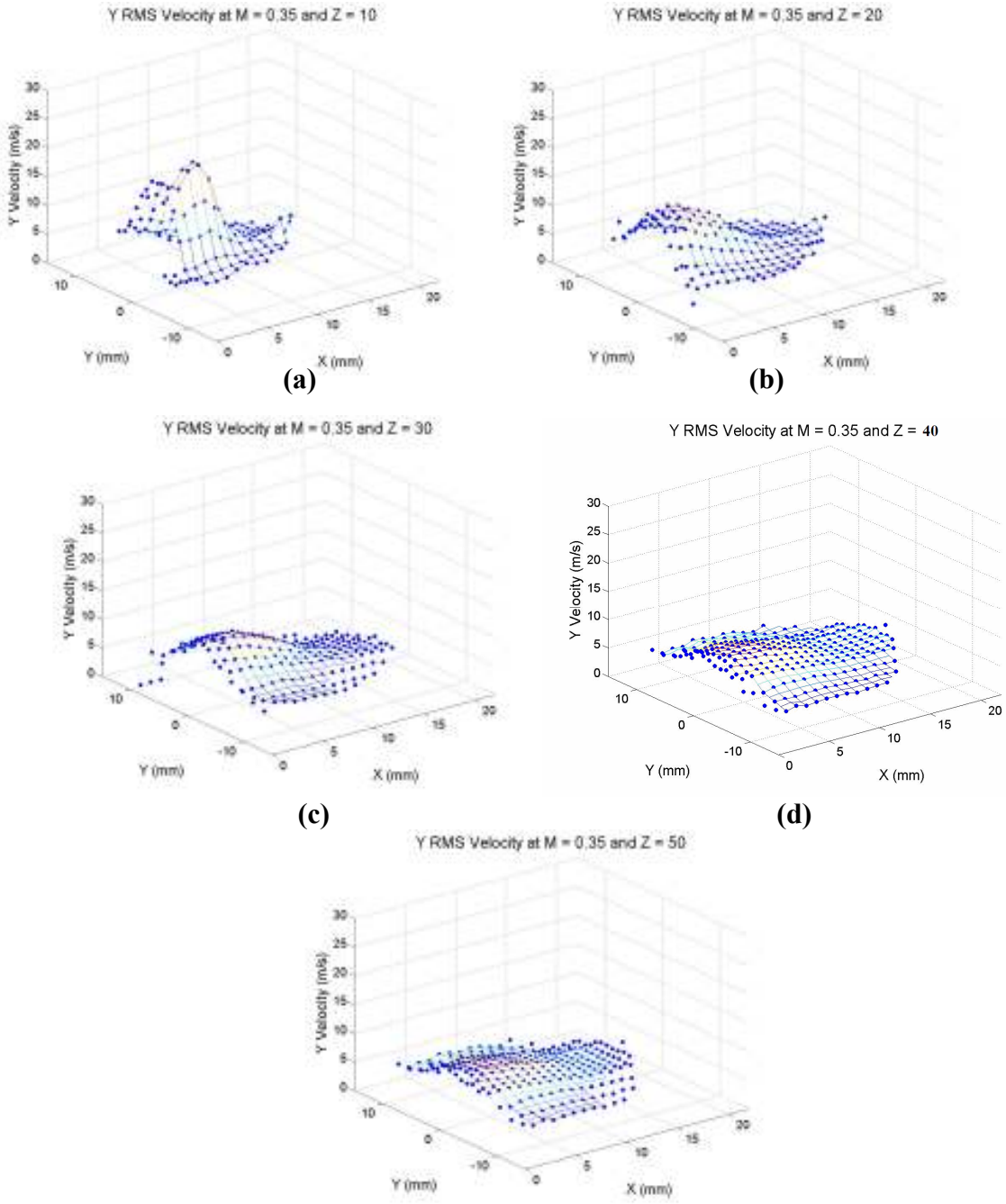

Figure A.29: Y RMS Velocity at M=0.35 for different Z locations
(a) Z=10mm (b) Z=20mm (c) Z=30mm (d) Z=40mm (e) Z=50mm

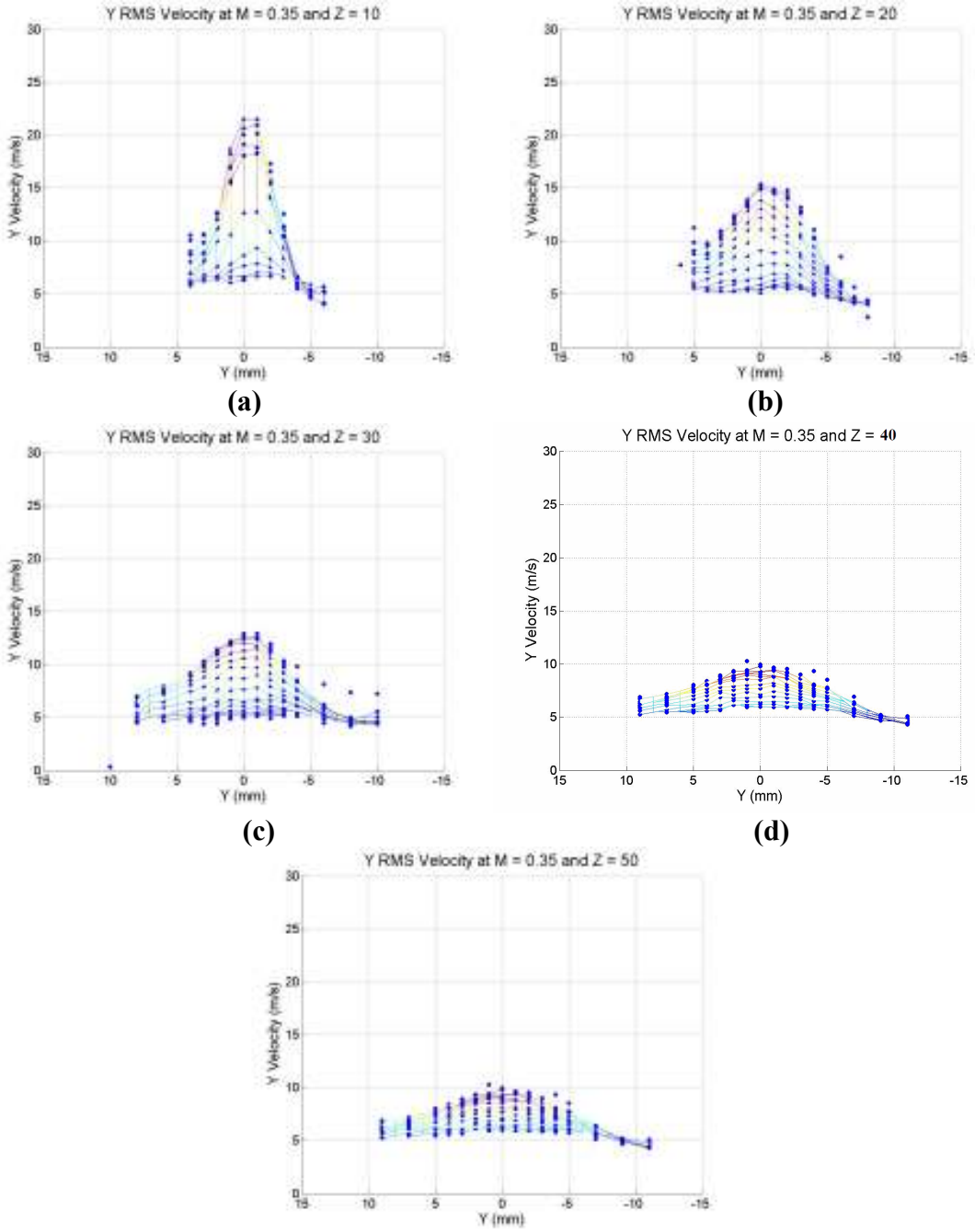

(a) **(b)** **(c)** **(d)** **(e)**

Figure A.30: Y RMS Velocity, view along y-axis at M=0.35 for different Z locations (a) Z=10mm (b) Z=20mm (c) Z=30mm (d) Z=40mm (e) Z=50mm

REFERENCES

[1] Marmottant, P., and Villermaux, E., "On Spray Formation," *J. Fluid Mechanics*, Vol. 498, 2004, pp. 73, 111.

[2]Bonnell, J. M., Marchall, R. L., and Riecke, G. T., "Combustion Instability in turbojet and Turbofan Augmentors", AIAA 71-698, *7th AIAA/SAE Propulsion Joint Specialist Conference Exhibi*t, Salt Lake City, UT 1971.

[3]Sallam, K.A., Dai, Z., Faeth, G.M., "Liquid breakup at the surface of turbulent round liquid jets in still gases," *International Journal of Multiphase Flow* 28 (2002).

[4]Tambe, S. B., Jeng, S. M., Mongia, H., and Hsiao, G., "Liquid Jets in Subsonic Flow", AIAA 2005-731, *43st Aerospace Science Meeting & Exhibi*t, Reno, NV 2005.

[5]Chen, T. H., Smith, C. R., and Schommer, D. G., "Multi-Zone Behavior of Transverse Liquid Jet in High-Speed Flow," *AIAA Paper*, 93-0453, 1993.

[6]Wu, P.-K., Hsiang, L.-P., and Faeth, G. M., ''Aerodynamic Effects on Primary and Secondary Breakup,'' Liquid Rocket Engine Combustion Instability, edited by V. Yang and W. Anderson, Vol. 169, Progress in Astronautics and Aeronautics, AIAA, Washington, DC, 1995, pp.247 – 279.

[7]Mazallon, J., Dai, Z., and Faeth, G. M., "Aerodynamic Primary Breakup at the Surface of Nonturbulent Round Liquid Jets in Cross-flows," AIAA 1998-716*, 36th Aerospace Science Meeting & Exhibi*t**,** Reno, NV 1998.

[8]Ghosh, S., and Hunt, J. C. R., "Spray Jets in Cross-Flow," *J. Fluid Mechanics*, Vol. 365, 1998, pp. 109, 136.

[9]Becker, J., and Hassa, C., "Breakup and Atomization of a Kerosene Jet in Crossflow at Elevated Pressure *Atomization and Sprays*, Vol. 11, 2002, pp. 49-67.

[10]Wu, P.-K., Miranda, R. F., and Faeth, G. M., ''Effects of Initial Flow Conditions on Primary Breakup of Nonturbulent and Turbulent Round Liquid Jets,'' Atomization and Sprays, Vol. 5, No. 2, 1995, pp. 175 – 196.

[11]Wu, P.-K., Kirkendall, K. A., Fuller, R. P., and Nejad, A. S., "Spray Structures of Liquid Jets Atomized in Subsonic Cross-flows," *Journal of Propulsion and Power*, Vol. 14, No. 2, 1998, pp. 173, 184.

[12]Rancher, M., Becker, J., Hassa, C., and Doerr, T., "Modeling of the Atomization of a Plain Liquid Fuel Jet in Crossflow at Gas Turbine Conditions," *Aerospace Science and Technology 6*, 2002, pp. 495, 506.

[13]Wu, P.-K., Kirkendall, K. A., Fuller, R. P., and Nejad, A. S., "Breakup Processes of Liquid Jets in Subsonic Cross-flows," *Journal of Propulsion and Power*, Vol. 13, No. 1, 1997, pp. 64,73.

[14]Stenzler, J. N., Lee, J. G., and Santavicca, D. A., "Penetration of Liquid Jets in a Crossflow", AIAA 2003-1327, *41st Aerospace Science Meeting & Exhibi*t, **,** Reno, NV 2003.

[15]Leong, M..Y., McDonell, V.G., Samvelsen, G.S., "Effect of ambient pressure on an airblast spray injected into a crossflow", Journal of Propulsion and Power, Vol. 17, No. 5, Sept-Oct 2001

[16]Aalburg, C., Sallam, K. A. and Faeth, G.M.., "Properties of Nonturbulent Round Liquid Jets in Uniform Crossflow," AIAA 2004-0969, Jan 2004.

[17]Johnson, J. N., Lubarsky, E., Zinn, B. T., "Experimental Investigation of Spray Dynamics Under Jet Engine Augmentor Conditions", AIAA 2005-4480, *AIAA/ASME/SAE/ASEE Joint Propulsion Conference & Exhibit*, Tuscon, AZ 2005.

[18]Lubarsky, E., Gopala, Y., Bibik, O., Zinn, B. T., "Experimental Investigation of Spray Dynamics in Crossflow of Pre-heated air at Elevated Pressure", AIAA 2006-1342, *44th Aerospace Science Meeting & Exhibi*t, **,** Reno, NV 2006

[19]Gopala, Y., Lubarsky, E., Oleksandr, B., and Zinn, B.T., Dai, Z., "Experimental Investigation of Spray Dynamics in Cross-flowing air at high Weber number" AIAA-2006-4568 42nd AIAA/ASME/SAE/ASEE Joint Propulsion Conference and Exhibit, Sacramento, California, July 9-12, 2006

[20]Inamura, T and Nagai, N., "Spray characteristics of Liquid jets traversing in subsonic airstream" Journal of Propulsion and Power, Vol. 13, No. 2 March-April 1997, pp.250-256

VITA

JONTHAN R. REICHEL

Jonathan Reichel was born in Ft. Lauderdale, FL. He attended North Allegheny Public Schools while living with his family in Wexford, PA during most of his childhood. He went on to earn his B.S. in Ocean Engineering at the United States Naval Academy in Annapolis, MD. Jonathan was commissioned an Ensign in the U.S. Navy in May 2006 and came to Georgia Tech to earn his M.S. in Aerospace Engineering prior to attending U.S. Navy flight school on his way to becoming a Naval Aviator.